Interfacial Characterisation of Sol-Gel Derived Coatings of Hydroxyapatite and Zirconia Thin Films with Anodised Titanium Substrates

A THESIS SUBMITTED IN FULFILMENT OF THE REQUIREMENTS FOR THE
DEGREE OF DOCTOR OF PHILOSOPHY

BY

Richard Roest

B.Sc. M.Sc. (UTS)

UNIVERSITY OF TECHNOLOGY, SYDNEY

November 2008

CERTIFICATE OF AUTHORSHIP/ORIGINALITY

I certify that this thesis has not previously been submitted for a degree nor has it been submitted as part of the requirements for a degree except as fully acknowledged within the text.

I also certify that the thesis has been written by me. Any help that I have received in my research work and the preparation of the thesis itself has been acknowledged. In addition, I certify that all information sources and literature used are indicated in the thesis.

Signature of Candidate

Production Note:
Signature removed prior to publication.

ABSTRACT

The anodisation of titanium involves the formation of a thin, compact oxide layer, which improves the wettability of the oxide film. This process involves the conversion of the rutile structure of the original titanium oxide into a mixed rutile and crystalline anatase structure. An understanding of the anodised structure and how it influences the bonding properties of the sol-gel coating of hydroxyapatite (HAp) and zirconia is the main focus of this research project.

The titanium samples were anodised in a mixed phosphoric acid (H_3PO_4) sulphuric acid (H_2SO_4) solution. The samples were also anodised at three different voltages, 25V, 50V and 75 Volts for 30 minutes. Both anodised and original titanium samples were spin coated with alkoxide-derived hydroxyapatite and zirconia sol-gel coatings and examined using X-ray diffraction and scanning electron microscopy. By controlling the oxide layer formed on the titanium substrates, its thickness and the amount of anatase formed in the mixed oxide layer as well as the oxide films porosity enabled the preparation of an oxide film surface that yielded the optimum conditions for coating with the sol gel solutions.

The diffusion theory can be seen to operating in the coating of the sol gel films through interdiffusion of the sol gel coating into the titanium oxide layer, with zirconium ions detected in the titanium oxide layer up to a depth of 75 microns and in the case of the hydroxyapatite sol gel coating phosphorus and calcium was detected in the titanium oxide layer.

The adhesion of the sol gel coated samples was tested using a micro-adhesion tester and the zirconia samples were further tested on an Ortho-pod tribological tester to determine the wear properties. The results show a significant improvement in interfacial energy of the hydroxyapatite films on the Ti6AL4V substrates over the C.P. titanium substrates with the anodised 25 volt and 50 volt Ti6Al4V substrate yielding values of 12.1 and 12.8 J/m^2 compared with values of less than 2 J/m^2 for the C.P. titanium samples.

Experimentation also shows that for both C.P. Titanium and Ti6Al4V substrates the 25 and 50 volt anodised samples for the crack free zirconia have interface toughness values in excess of 1.5 MPa.m$^{1/2}$ in addition to them the Ti6Al4V substrate also is in excess of 1.5 MPa.m$^{1/2}$ indicating that these samples all possess good interface toughness values while the other substrates have toughness values half the previously mentioned samples of about 0.75 MPa.m$^{1/2}$.

The zirconia solution used was modified with 1- Butanol to reduce the viscosity of the zirconia sol gel to 10 -12 centipoise and this lead to the formation of a crack free zirconia coating of 100 nm thickness when spin coated, also the tetragonal polymorph was found on all substrates tested with X–ray diffraction.

Tribological results on the zirconia-coated titanium samples, both anodised and control, showed the titanium samples yielded better wear-resistance properties than the double coated samples. The 50 volt anodised titanium samples yielded the best wear resistance of all samples tested after 500,000 cycles on the Ortho-pod machine in water.

Acknowledgements

I am deeply indebted to a number of people for their help and guidance throughout the duration of this degree. In particular, I would like to express my deepest gratitude to my supervisor, Associate Professor Besim Ben-Nissan for the guidance, encouragement, expertise and friendship he has given during this degree.

Special thanks to Dr Greg Heness, Dr Norman Booth, Alex Rubel and Jules Guerbois for their support and assistance; their time and enthusiasm are greatly appreciated.

I would also like to offer a special thank you to the following people for their assistance with this research study:

- Associate Professor Matthew Phillips, Dr Richard Wuhrer, Mark Berkahn and Ms Katie McBean from the Micro structural Analysis Unit of UTS, whose help and encouragement with the SEM and XRD analysis were greatly appreciated.

- Associate Professor Alan W. Eberhardt and Carrie Stewart from the University of Alabama, who assisted with the tribological testing of my samples.

I would also like to acknowledge the support of the Australian Institute for Nuclear Science and Engineering (AINSE) for giving me a Postgraduate Research Award which provided access to a wide range of facilities at the Lucas Heights site, and I would also like to acknowledge the support of the Australian Nuclear Science and Technology Organisation (ANSTO) Materials Engineering Division.

I would also like to give special thanks to Dr Bruno Latella from the Materials Engineering Division of ANSTO who helped conduct the micro-adhesion testing and provided endless assistance and mentoring during the project in addition to his friendship and guidance which made the journey towards completing my thesis more enjoyable.

Finally, a special thanks to my family and close friends for their support and confidence during this project.

TABLE OF CONTENTS

LIST OF TABLES

LIST OF FIGURES AND ILLUSTRATIONS

APPENDIX

LIST OF SYMBOLS, ABBREVIATIONS AND NOMENCLATURE

V	Volts
A	Constants
B	Constants
σ_c	Critical stress for cracking (MPa)
ε_c	Strain at first cracking
E_f	Young's Modulus of film (MPa)
σ_r	Residual Stress
λ_f	Fracture energy of film (Jm^{-2})
$g(\alpha)$	Constant
α	Dundas parameter
K_{ic}	Film toughness ($MPa.m^{1/2}$)
d	Oxide thickness
ε	Strain
σ	Stress (MPa)

PUBLICATION LIST

2007 R. Roest, A.J. Atanacio, B.A. Latella, R. Wuhrer, and B. Ben-Nissan, 'An Investigation of Sol gel coated zirconia thin films on anodised titanium substrate by secondary ion mass spectrometry and scanning electron microscopy' Materials Forum Volume 31- 2007. Edited by J.M. Cairney and S.P.Ringer

2005 Roest, R. Heness, G., Latella, B., Ben-Nissan, B., "Fracture toughness of nanoscale Hydroxyapatite coatings on titanium substrates" Proc. 6th Int. Conf. Fract. & Strength of Solids, pp. 1297-1302, 2005

2004 Roest, R., Heness, G., Latella, B. and Ben-Nissan, B. "Fracture toughness of nanoscale zirconia coatings on titanium substrates", Proc. Int. Conf. Structural Integrity and Fracture, pp. 325-330, 2004

2004 R. Roest et al, "Adhesion of Sol-Gel Derived Zirconia Nano-Coatings on Surface Treated Titanium", *Key Engineering Materials*, Vols. 254-256, pp. 455-458, Trans Tech Publications, Switzerland. 2004.

2004 Roest, R., Eberhardt, A.W., Latella, B., Wuhrer, R. & Ben-Nissan, B. 2004, 'Tribology and adhesion of zirconia nano-coatings on surface treated titanium', *Transactions - 7th World Biomaterials Congress, Transactions - 7th World Biomaterials Congress*, pp. 1783.-1787th 2004.

2003 R. Roest et al, "Sol-Gel Derived Hydroxyapatite Coatings on Anodized Titanium Substrates", *XII International Workshop on Sol Gel Science and Technology*, pp. 112, 25-29 August 2003, Sydney.

2001 R. Roest and B. Ben-Nissan, "Surface Modification of Anodized Titanium for Calcium Phosphate Coatings", *Proceedings of the Engineering Materials*, 23-26 September 2001, Melbourne. (Eds.) E. Pereloma and K. Raviprasad, pp. 115. 2001

CHAPTER 1 - INTRODUCTION

1.1 BACKGROUND

The coating and surface modification of titanium is important as it permits the use of sol-gel-derived surface coatings whilst maintaining the favourable bulk properties of the titanium. In the biomedical field, the surface modification of titanium aims to inhibit wear, reduce corrosion and ion release, and promote biocompatibility. Sol-gel-derived ceramic coatings show promise due to their relative ease of production, ability to form a physically and chemically uniform coating over complex geometric shapes, and their potential to deliver exceptional mechanical properties due to their nanocrystalline structure. [1]

Coating techniques currently include dip coating, electrophoretic deposition, sputter coatings, thermal spraying and sol-gel. While all these techniques have been used in applying ceramic coatings, each possesses a particular drawback that prevents it from being the ideal coating system.

Dip coating requires high temperature sintering at greater than 1000°C, which can degrade the mechanical properties of the titanium substrate. Commercially pure (CP) titanium has a hexagonal, close-packed crystal structure (HCP) or alpha phase up to the beta transformation temperature (882.5°C), transforming to a body-centred cubic structure (BCC) or beta phase above this temperature. [2] This phase transformation at 882.5°C and the consequent strain during the transformation leads to the degraded bond strength of the ceramic coating. Electrophoretic deposition has similar problems to dip coating as well as a tendency towards non-uniform coatings.

Thermal spraying is the main technique employed today in the application of HAp coatings on medical implants. Despite its wide use, this technique has serious problems – such as comparatively thick, highly porous non-uniform coatings and especially poor bonding strength to metal implants. In addition, a problem apparent in the control of the HAp coating is the Ca/P ratio of the coating with phases subjected to high temperatures during the application of the coating. Dissociation of HAp to other phases such as CaO and ß-TCP is well reported. [3-5]

Sol-gel is another promising technique, but its main shortcoming is the poor quality of the ceramic/metal substrate interface. The aim of this project is to overcome this problem by modification of the titanium substrate with a controlled anodic oxide film.

1.2 THESIS STRUCTURE

The structure of the thesis is constructed with chapter two giving an overview of the titanium substrate and the effect of anodising on the oxide films formed and the effects of current, voltage and anodising solution on these films. Chapter three is where the sol gel solutions of hydroxyapatite and zirconia are introduced with the properties and techniques used in this thesis to coat the nano-coatings on the titanium substrates are developed. Chapter four covers the biocompatible interface of the coated surface film formed when the titanium substrates are coated with hydroxyapatite sol gel solution.

Chapters five through to nine deal with the testing of the interface and the sol gel coatings from using secondary mass ion spectrometry to gain an understanding of the interface formed with differing titanium substrates, x- ray diffraction to gather information on the sol gel coatings formed, micro adhesion testing tribology and scanning electron microscopy to further investigate the mechanical properties of the sol gel coatings and the interfaces formed. The final chapter is the conclusion where all the threads of the thesis are brought together to present a coherent argument for the use of anodising titanium to form a stable oxide film for the production of hydroxyapatite and zirconia sol gel coatings.

1.3 STATEMENT OF STUDY AIMS

The aim of this study is to produce adherent hydroxyapatite and zirconia sol-gel coatings on anodised titanium substrates. An understanding of the anodised structure and its interfacial characteristics and influence on the bonding properties with the sol-gel coatings of hydroxyapatite (HAp) and zirconia is the main focus of this research project. By anodising the titanium, a surface of controlled thickness and properties can be produced on the titanium substrate.

This study aims to improve the adhesion of the zirconia and hydroxyapatite sol gel coatings with this controlled oxide interface. With the micro adhesion testing, tribological and biocompatibility studies of the coated samples giving a guide to the mechanical and physical properties of the sol gel coatings and thus demonstrating the improved properties of the sol gel coatings on the anodised titanium substrates.

CHAPTER 2 – TITANIUM SUBSTRATES AND ANODISING

2.1 TITANIUM

Titanium is an allotropic element, in that more than one crystallographic form can exist. [5] The hexagonal close-packed crystal structure (HCP), which is known as the alpha phase, exists at room temperature. A transformation to the body-centred cubic structure (BCC), or beta phase, takes place when titanium solidifies from a liquid or when solid titanium is heated to temperatures above 883°C. There are three generally accepted classes of titanium alloys: “alpha”, “beta” and “alpha-beta”. [2, 6, 7]

By alloying titanium metal with other elements, either of these crystal structures can be selectively stabilised at room temperature, thus enabling the manufacture of stable alpha, alpha-beta and beta alloys. Common alloying elements used to stabilise the alpha phase include aluminium, tin and oxygen. Some common beta stabilisers are niobium, molybdenum, tantalum, chromium, iron and vanadium. Many alloys combine a carefully chosen combination of the two types of elements, and these are classified as “alpha-beta” alloys. [2, 6, 7]

Titanium is as strong as steel and yet is 45% lighter. Titanium alloys will work continuously, resisting creep and oxidation at temperatures up to 600°C, and down to liquid nitrogen temperatures without a loss in toughness. Titanium is a very reactive metal that shows remarkable corrosion resistance in oxidising acid environments by virtue of its passive oxide film.

Titanium develops a thin, tenacious and highly protective native surface oxide film. Titanium's wear properties are limited due to its tendency to gall and seize and its reactivity to atmospheric oxygen. Anodising titanium decreases galling, improves corrosion resistance, and provides stable optical properties to its components.

There are only a few biomaterials in wide use today that have exceptional osseointegratibility: commercially pure (CP) titanium, commercially pure (CP) tantalum, hydroxyapatite and bioactive ceramics [4]. Branemark P.I. R. Adell, T. Albrektsson, U. Lekholm, S. Lundkvist and B. Rockler [8] used titanium for dental implant applications, and coined the term Osseo integration to describe the condition and the process for having a stable loaded implant in direct contact with bone. Integration of a foreign substance, such as a metallic implant, into bone or soft tissue of a living host generates many complex physiological and biological reactions.

2.2 TITANIUM ANODISING

In anodic oxidation (anodising), electrode reactions in combination with an electrical field drive metal and oxygen ion diffusion, which leads to the formation and growth of an oxide film at the anode surface. Anodising is a well-established method for producing differing types of protective oxide films on metals. It can also be used for producing increased oxide thicknesses (for enhanced corrosion protection and decreased ion release), colouration and porous coatings. [6, 9]

The structural and chemical properties of anodic oxides on titanium can be varied over quite a wide range by controlling the processing parameters, such as anode potential, electrolyte composition, temperature and current. Different diluted acids (H_2SO_4, H_3PO_4, acetic acid and others) are commonly used electrolytes for anodic oxidation of titanium. [6, 9]

The main reactions leading to oxidation at the anode are as follows [6]:

At Ti / Ti Oxide Interface

$$Ti \rightarrow Ti^{2+} + 2e^-$$

At Ti Oxide / Electrolyte Interface

$$2H_2O \rightarrow O^{2-} + 4H^+$$

(Oxygen ions react with Ti to form oxide)

$$2H_2O \rightarrow O_2(g) + 4H^+ + 4e^-$$

(Oxygen gas evolves from surface)

At Both Interfaces

$$Ti_2^+ + 2O^{2-} \rightarrow TiO_2 + 2e^-$$

The titanium and oxygen ions formed in these redox reactions are driven through the oxide film by the externally applied electric field, leading to the growth of the oxide film. Since anodic titanium oxides have a high resistivity relative to the electrolyte and the metallic parts of the electrical circuit, the applied voltage will predominantly drop over the oxide film of the anode.

As long as the electric field is strong enough to drive the ions through the oxide, a current will flow and the film will continue to grow [6]. This is why the final oxide thickness, **d**, during anodic oxidation is almost linearly dependant on the applied voltage, **U**:

$$\mathbf{d = \alpha U} \qquad \textbf{(2.1)}$$

Where **α** is a growth constant which is usually in the range 1.5-3.0 nmV^{-1}.

This linear relationship holds below the dielectric breakdown limit of the oxide, [10] which is around 100-150 V depending on the electrolyte and other process conditions. [6] If the anodising is carried out at voltages above the breakdown limit, the oxide will no longer be resistive enough to prevent further current flow and oxide growth.

At such high voltages the process will lead to increased gas evolution and frequent sparking. This type of anodising is often referred to as spark anodising. It leads to less uniform and more porous oxide films than anodising below the dielectric breakdown limit. [6]

Titanium is classified as a oxide film former, in view of its position in the periodic table and its electrochemical behaviour [9], that is, a metal whose surface is always covered with a "natural" oxide film when exposed to air, water or other oxygen-containing media. The "natural" oxide film on titanium ranges in thickness from 5 to 70 nm, depending on the composition of the metal and surrounding medium, the maximum temperature reached during the working of the metal, etc. [11, 12]

2.3 FORMATION MECHANISM OF ANODIC OXIDE FILMS

The formation mechanism of anodic oxide films, and in particular those on aluminium and tantalum, has been the subject of extensive research. [13] Although the general rules governing the anodic oxidation of titanium are roughly the same as for other "valve" metals. (That is, the ionic current during anodic polarisation leads to film formation, and the relatively large contribution of ionic current associated with the high heat of formation of the respective oxides). [14, 15]

According to Kossyi, G., V. Nivakoyskii, and Y.A. Kolotyrkin [16], Tomashov, I. and T. Matveeva with Tomashov, N. and N. Strukov [16, 17] the first step in the anodic oxidation of titanium involves the formation of an adsorbed layer of oxygen (or some oxygenated species) on the metal surface, or more accurately on the surface of the pre-existing "natural" oxide film.

At low anodic potentials, the relationship between the anodic current and the electric field across the oxide film is described by the following equation [18, 19]:

$$\mathbf{i_t = A \exp BE} \qquad \mathbf{(2.2)}$$

where i_t is the ionic current, E is the electric field strength and A and B are constants.

Evidence exists that the anodic film on titanium grows as a result of the transfer of Ti^{2+} cations through the film, that is, that the growth takes place at the oxide surface interface [20-22]. However, others have reported that the film grows by oxide ion transfer [23, 24]. Aladjem, A. [25] argues that it is most probable that both Ti^{2+} and O^{2-} ion transfer contribute simultaneously to the growth mechanism, similar to that of oxidation in a gas.

The role of the electrolyte in the formation mechanism has not been studied in great detail. The nature of the anions influences both the initial passivation and subsequent growth stages [26-28]; it has been suggested by Cotton J.B [29] that an anodic film is formed only if the conditions (including the nature of the electrolyte) favour the formation of Ti^{4+} rather than Ti^{3+} ions.

2.4 GROWTH MODES FOR ANODIC OXIDE FILMS

Three modes of growth are described in the literature for anodic films [30-35]:

1/ The potentiostatic growth mode for which a constant potential versus a reference electrode is applied directly to the anode [36].

2/ The galvanostatic growth mode for which a constant potential is applied to the electrochemical cell [36].

3/ The combined growth mode for which a constant current is first applied to the cell until the anode potential reaches a fixed value, then the potential is maintained for a fixed period of time [36].

All of these growth modes are based on the H_2SO_4 electrolyte.

According to the published data in the literature, regardless of the growth mode, the composition of the film, potentials higher than 45 volts lead to microcrystalline anatase and/or rutile [37-52] oxide layers, although Marino, Claudia E. B.Nascente, Pedro A. P. Biaggio, Sonia R. Rocha-Filho, Romeu C. and

Bocchi, Nerilso. [53] argue that a monoclinic mixed oxide of Ti_3O_5 ($TiO_2.Ti_2O_3$) is formed at the same time. J.L. Delplancke and R. Winand [36] argue that during potentiostatic anodisation, the current density at which the initial oxide film is growing is only limited by the available power of the rectifier (power source). In most cases the initial current density is very high. Micro-crystals are formed, but their growth is so fast that they are randomly orientated, forming a thick insulating oxide film.

In contrast, the galvanostatic and the combined growth films are grown at a constant current density and for some orientations of the underlying titanium crystals, clusters of orientated oxide micro-crystals are formed; these clusters act as preferential channels for the current flow during cathodic polarisation. These channels modify the electrochemical and semi-conducting properties of the anodic oxide films.

According to Leitner, K., J.W. Shultze, and U. Stimming [54], the donor density in the titanium anodic oxide films could be related to point defects such as oxygen vacancies. A linear relationship for the donor density versus the reciprocal square thickness of the oxide film is observed [55].

The growth mode of anodic oxide films on titanium has a considerable influence on the composition and the properties of these films, from a macroscopic point of view. Whatever the growth mode, films grown at 50 volts are crystallised but the microscopic orientation of the micro-crystals depends on the anodising conditions for galvanostatic and combined growth films. Preferential conducting channels are observed [36].

Figures 2.1, 2.2 and 2.3 give a schematic overview of the combined growth modes speculated on by J.L. Delplancke and R. Winand [36] in sulphuric acid solutions and are based on the titanium surface processing work of C. Jung. [56] In figure 2.1 before a current is applied the natural passive oxide layer formed prior to anodisation sits in the electrolyte and will slowly dissolve if left in the solution for a period of time as the anodising process is not just a mechanism where the oxide layer grows but a ever changing environment of oxide growth and dissolution depending on the cell current and voltage parameters.

Figure 2.2 gives a summary of the start of the titanium oxide growth as oxygen ions migrate into the oxide film and titanium ions Ti^{2+}, Ti^{3+} and Ti^{4+} as speculated by Cotton [32], Marino *et al*. [53] Delplancke and Winand [36] and Aladjem [9] resulting in a titanium oxide layer that primarily consists of TiO_2 but also a monoclinic mixed oxide of Ti_3O_5 ($TiO_2.Ti_2O_3$) is formed at the same time.

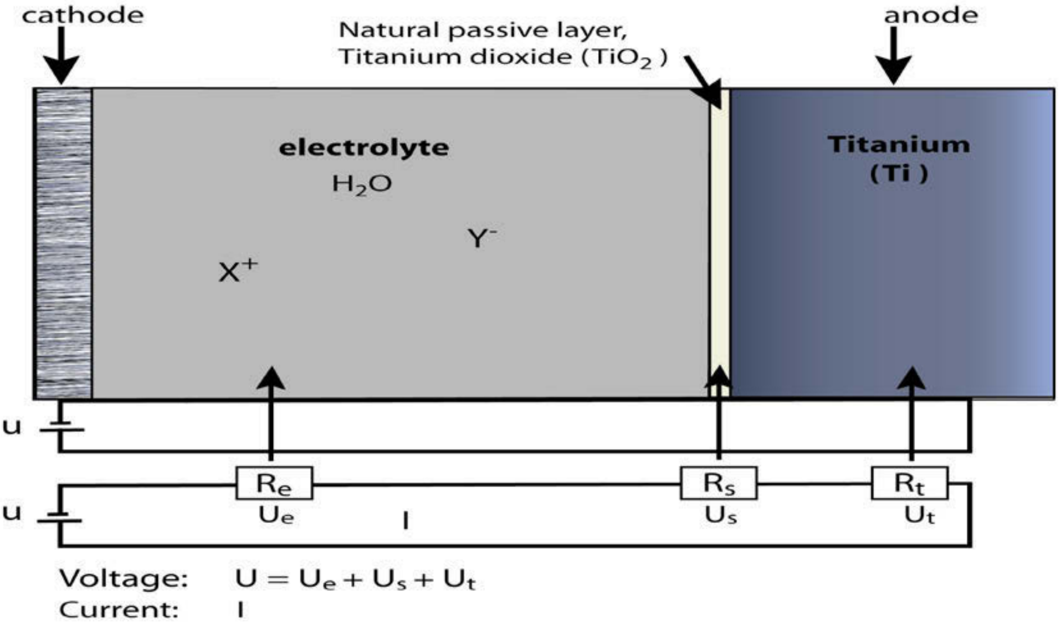

Figure 2.1 *Illustration of titanium anodising cell before current is applied, based on a Christiane Jung presentation. [56]*

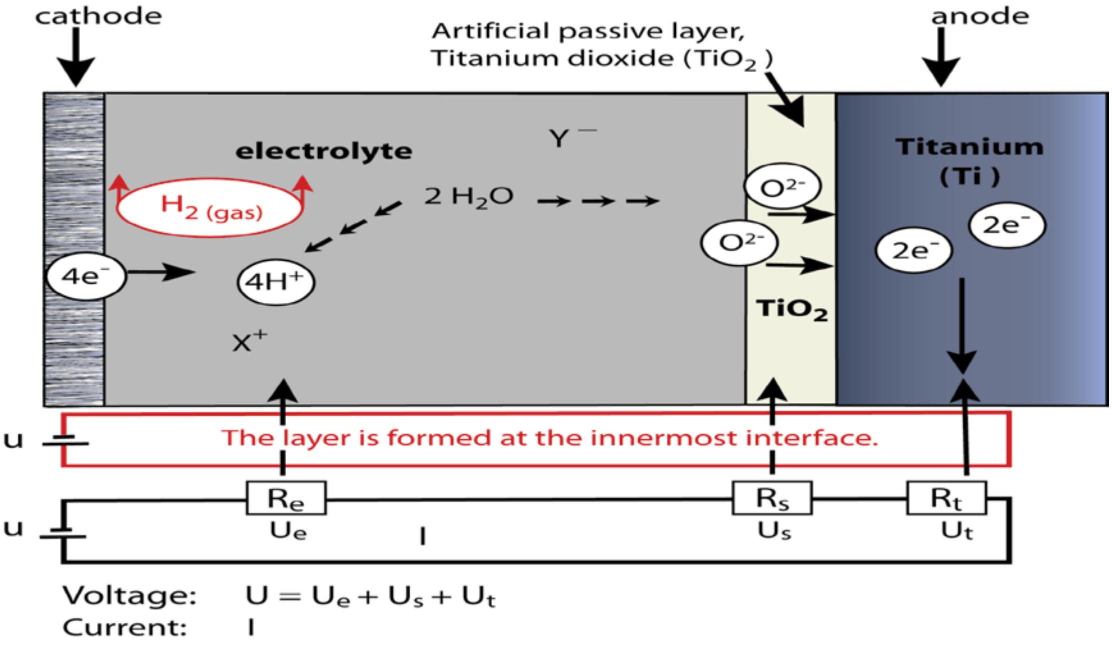

Figure 2.2 *Start of the anodised titanium oxide layer formation showing the oxygen ions moving into the titanium oxide layer. [56]*

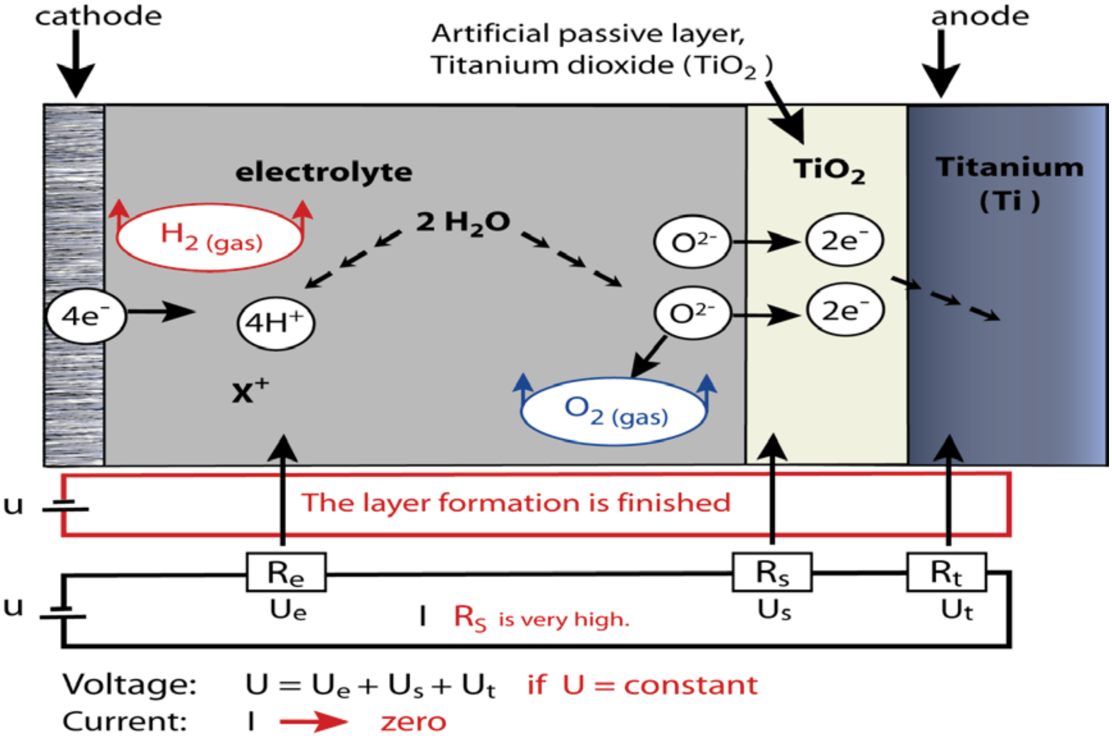

Figure 2.3 *Final layer formation after the titanium oxide is finished growing. [56]*

In figure 2.3 the titanium oxide layer has finished growing, resistance at the oxide face is very high and the current has stopped flowing in the cell. The excess oxygen ions are released as oxygen gas and the oxide layer formed will slowly start to dissolve in the electrolyte over time. It is important to remove the titanium sample from the electrolyte at this point to preserve the integrity of the oxide film and quick cleaning in distilled water to remove any surface electrolyte ion contamination of the oxide film formed.

2.5 ANODISING SURFACE ROUGHNESS

When anodising both commercially pure grade two titanium (C.P. Ti) and the titanium alloy (Ti6Al4V there was a substantial increase in the surface roughness, R_a, by a factor of 10 when using an instantaneous voltage of twenty five volts compared with a slowly applied voltage over an approximate two minute period. All samples were anodised for twenty minutes, with the surface roughness measured with (ANSTO) stylus profilometer and the resulting surface roughness differences are shown in figure 2.4.

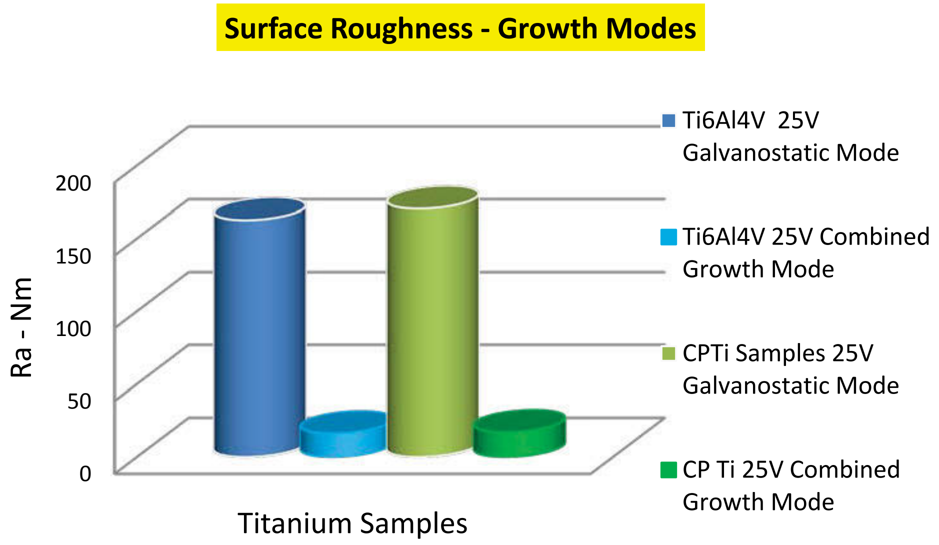

Figure 2.4 *Ra Surface roughness chart of both C.P. Titanium and Ti6Al4V alloy anodised at 25 Volts.*

Due to limitations in the rectifier used for the experiments, which has a 10 amp maximum current. A variation on the combined growth mode approach [36] was used by allowing the voltage to be slowly increased over a two minute period. It allowed for the anodic current to decrease and thus allow the cell voltage to increase to the desired voltage in this case 25 volts. This approach also has the added benefit of a much smoother and less porous oxide film to be formed.

2.6 TITANIUM CORROSION RESISTANCE

Titanium and its alloys are used in a wide range of environments from mildly reducing to highly oxidising where the protective oxide films spontaneously form and remain stable in the environment. Titanium's protective oxide layer is susceptible to attack in acidic reducing solutions, strong oxidizers, 90% hydrogen peroxide, ionisable fluorine compounds can activate the surface layer and lead to rapid corrosion of the titanium surface oxide. Likewise, dry chlorine gas is corrosive to the titanium surface leading to severe stress corrosion cracking. [57]

The excellent corrosion resistance of titanium results from the formation of a highly adherent, chemically stable oxide film. This film forms spontaneously when exposed to a fresh metal surface giving titanium a self-healing property in the presence of air or moisture.

2.6.1 GENERAL CORROSION RESISTANCE

There are several mechanisms used to improve the corrosion resistance of titanium;

1/ increasing the surface oxide coverage by anodising and thermal oxidation.

2/ anodic protection by impressed anodic current or galvanically coupling with a more noble metal to maintain the surface oxide film.

3/ alloying titanium with certain elements such as palladium and nickel. [57-59]

4/ applying precious metal coatings.

5/ adding oxidising species (inhibitors) to the reducing environment, which allows for oxide film stabilization.

6/ coating the oxide film with a protective zirconia layer [60-62].

2.7 ANODISING SET-UP AND PROCESSES

Two solutions were originally used in my early work of the study: a concentrated phosphoric and sulphuric acid solution which is derived from a common industry solution [63], and a dilute solution of the same acids which is a variation on a solution used for adhering paint to titanium [63], giving a more porous oxide film that yields good mechanical keying for the paint. D. Velten, V. Biehl, F. Aubertin, B. Valeske, W. Possart and J. Breme [64] and Arsov [10, 65, 66] both used H_2SO_4 as an anodising solution but this solution gives a highly porous oxide film.

Three voltages were used, from 25 volts, 50 volts and 75 volts for a period of twenty minutes in each anodising cycle. These voltages were based on the work of Arsov [10], Aladjem [9], Delplancke and Winand [37], Blondeau, G.Froelicher, M. Froment, M. and Hugot-Le Goff, A.[67]. These studies showed that the 25 volt current produces a mainly rutile oxide film, the 50 volt current a mixed rutile and anatase oxide film, and the 75 volt current again produces a mixed rutile and anatase oxide film where the anatase crystals formed were larger in size with increasing voltage. The twenty minutes used for anodising was based on earlier anodising work in my master thesis.

The rectifier was constructed with a voltage range of 0-90 volts. Two anodising racks were made from the Ti6Al4V alloy; the racks shown in figure 2.5 were designed to allow the anodisation of six samples at the same time. It was important to ensure that the racks were anodised firstly to ensure that the current was only available for the samples when anodising. The cathodes were made using CP (99.7%) grade 1 thin plate from Titanium International (Aust.) and the anodes were 250 mm x 50 mm x 1 mm plates. Surface preparation techniques of the titanium samples is covered in chapter 8.

2.8 ANODISING SOLUTIONS

The early literature on titanium-anodising solutions concentrated mainly on sulphuric acid as the electrolyte [10, 13, 36, 53, 58, 63-77]. However, Zwilling, V., M. Aucouturier, and E. Darque-Ceretti [78] used chromic acid as an electrolyte, although for medical implants, using this electrolyte is not a realistic option as chromic acid is cytotoxic and the risk of contamination is too high for biomedical applications.

Early anodising solutions for aluminium used phosphoric acid as the main electrolyte with good success rates. The combination of phosphoric acid and sulphuric acid is a common anodising electrolyte for titanium [63]. This combination of acids provides a good electrolyte for the formation of a controlled low porosity oxide film formation with good adherence.

The solution used in this study is a variation of the dilute solution previously mentioned and was chosen due to its ability to form a controlled oxide film with low porosity:

Anodising Solution

20% - H_3PO_4

10% - H_2SO_4

70 % - Distilled H_2O

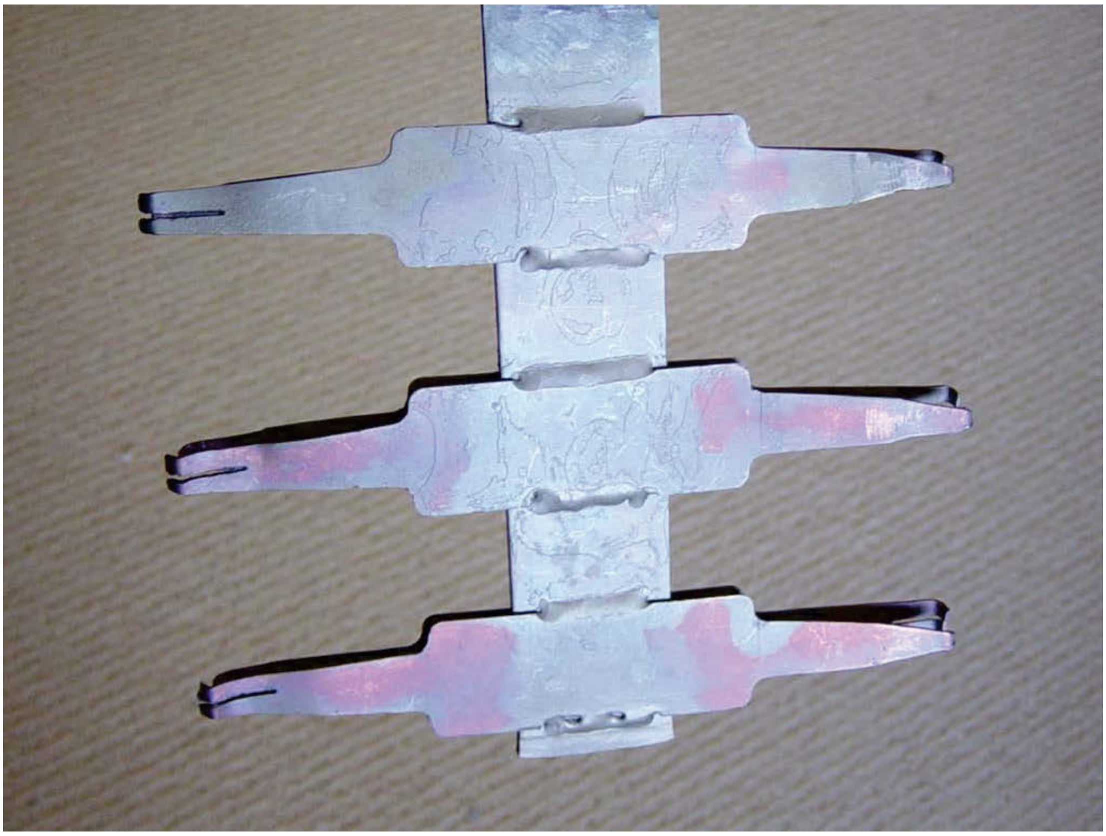

Figure 2.5 *Titanium Anodising rack with anodic oxide film evident after use*

2.9 ANODISED SAMPLES

The samples in figure 2.6 show the relative homogeneity of the oxide layers after heat treating to 550°C on both the Ti6Al4V and C.P. Titanium samples.

The optical microscopy pictures shown in Figures 2.7 to 2.8 clearly demonstrate the differences between the Ti6Al4V and C.P. Titanium samples when anodised at 25 volts, although they have a similar thickness of 50nm having grown at an approximate rate of 2 nm/volt over a twenty minute period.

The colour similarity of the respective voltages indicates that the thickness of the oxide film is similar for the same voltages. The colour of the anodised samples, beyond giving an indication of their thickness, also reveals the topography of the surface oxide film. Changing colours reveals the differing thicknesses of the oxide layer, as it only takes a difference of one to two nanometres to effect a change in colour of the oxide film [70]. Thus variations in the thickness and homogeneity of the coating are easily observed via colour change of the oxide layer.

The lower-voltage anodised samples have a greater homogeneity of colour, this being due to the thickness of the film at these voltages being only about 50 nm. As the voltage increases the thickness of the film increases, and the variation of the topography on the surface oxide formed over the sample increases. The 25-volt anodised samples shown in Figures 2.7 and 2.8 have an oxide thickness of approximately 50 nm when examined after micro-adhesion testing of the oxide film with scanning electron microscopy (SEM). The 50-volt samples shown in Figures 2.9 and 2.10 have a gold tinge with blue oxide film colour, which has an approximate thickness of 100 nm. The 75-volt samples in Figures 2.11 and 2.12 have a predominate bluish tinge and an approximate oxide thickness of 150 nm.

The anodised samples were also heat treated at 550°C for two hours to see if the properties of the oxide film formed changed after heat treating. This is important, as, after sol-gel coating the samples are to be fired at this temperature for two hours. The anodised samples after heat treatment demonstrated a colour change of relatively homogenous nature and an approximate thickness increase of 5-10% over the original anodised samples. The original samples showed a change in colour, but it was significant to notice the non-homogeneity of the colour and thus the thickness of these samples. All samples anodised oxide layers were measured after were measured after micro adhesion testing in previous work carried out. [79-82]

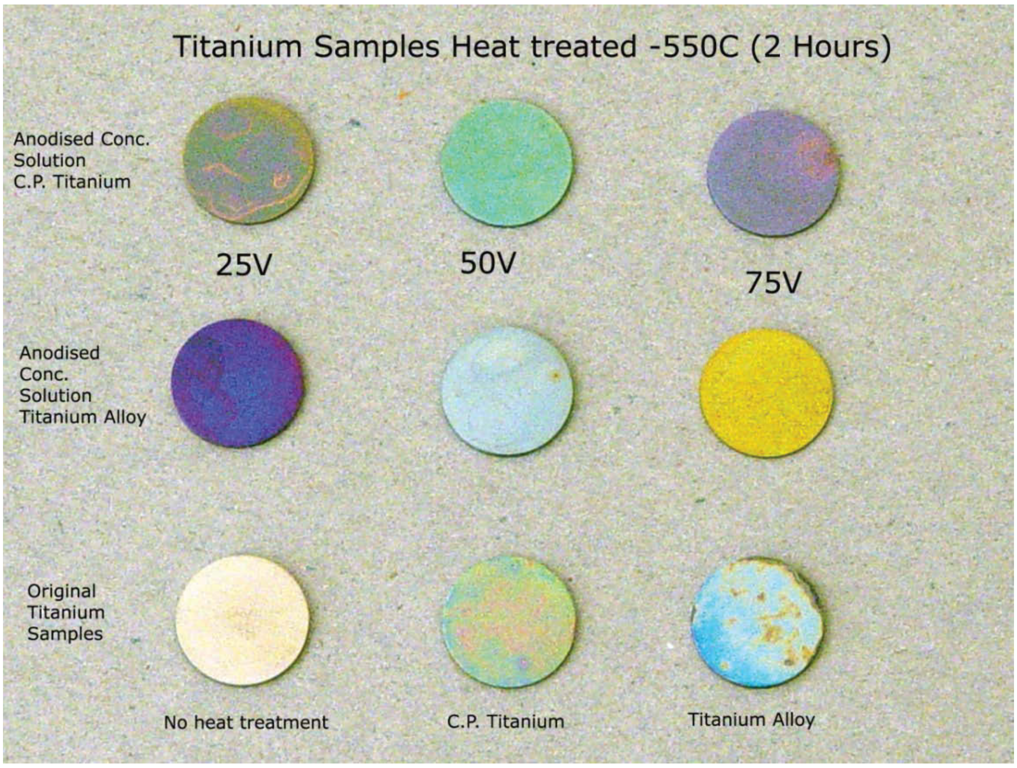

Figure 2.6 *Heat-treated (550°C) samples, showing homogeneity of anodised samples, in concentrated solutions.*

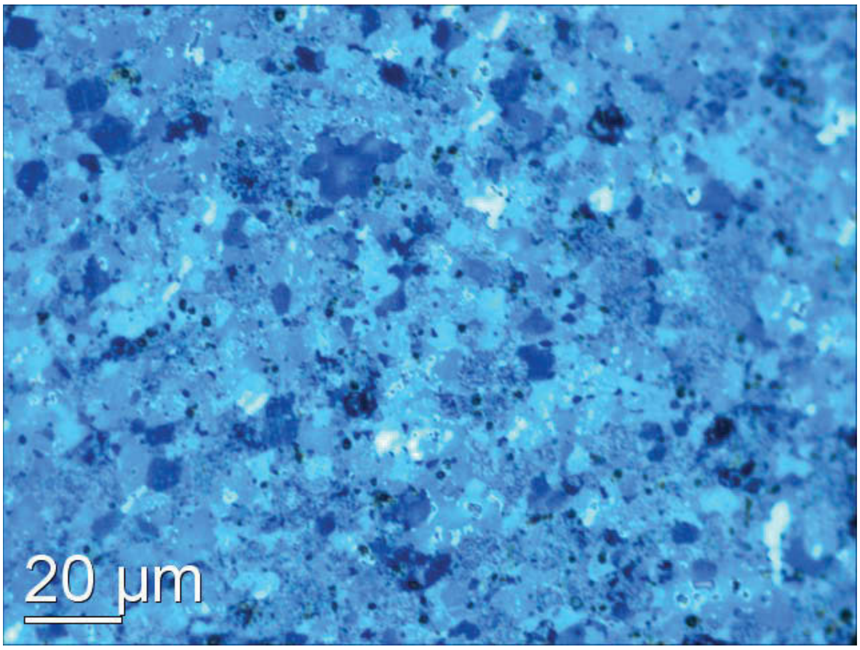

Figure 2.7 *Ti6Al4V sample anodised at 25V*

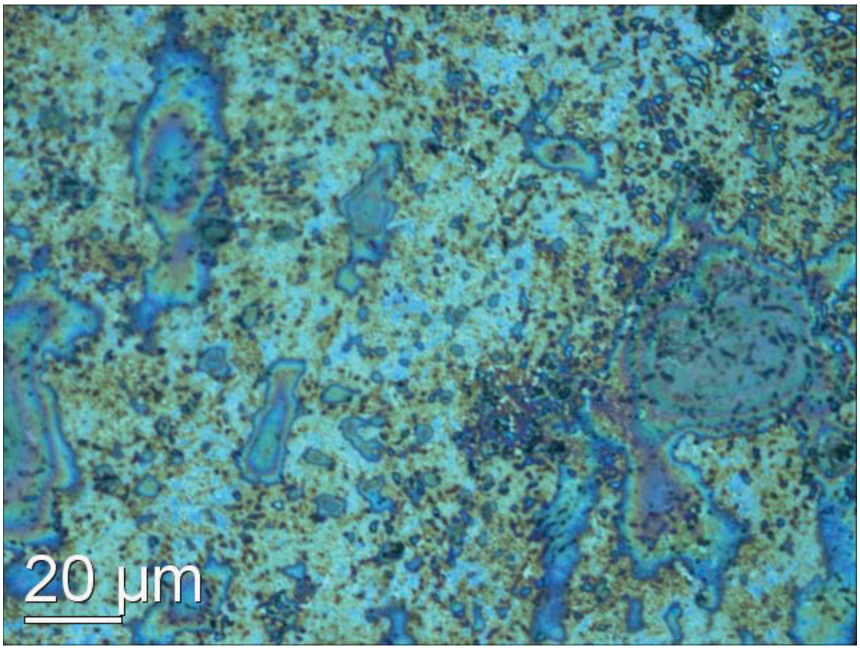

Figure 2.8 *C.P. Titanium sample anodised at 25V*

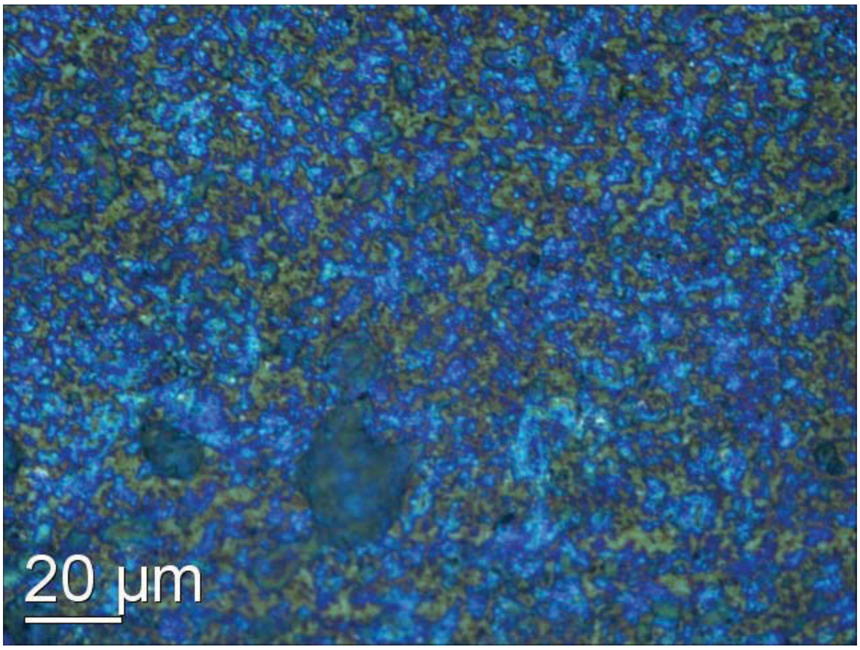

Figure 2.9 *C.P. Titanium sample anodised at 50V*

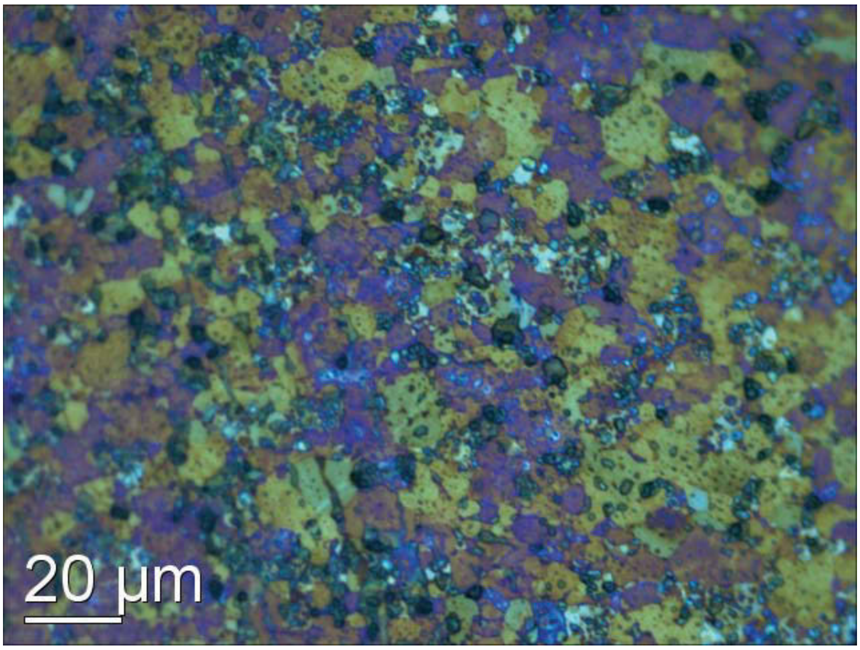

Figure 2.10 *Ti6Al4V sample anodised at 50V*

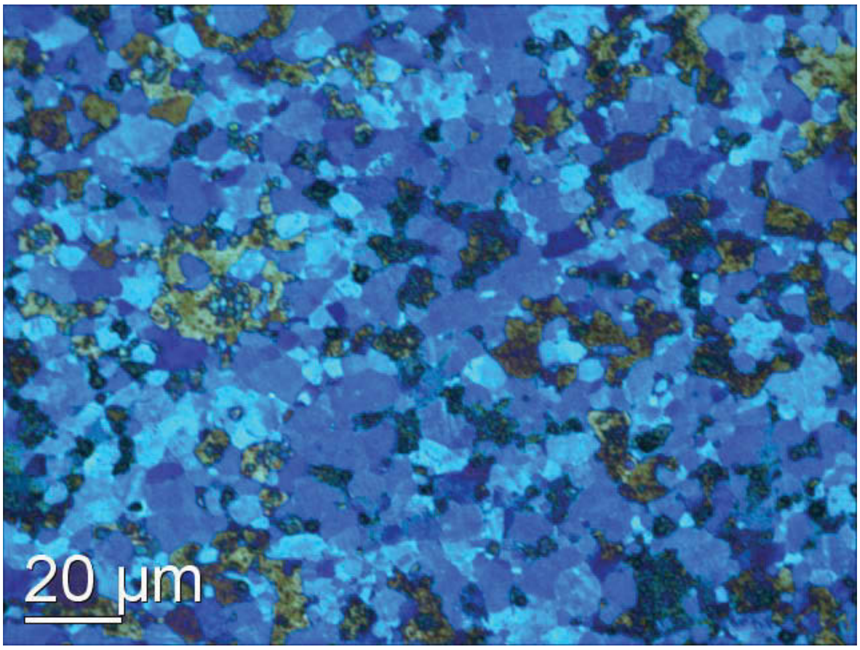

Figure 2.11 *C.P. Titanium sample anodised at 75V*

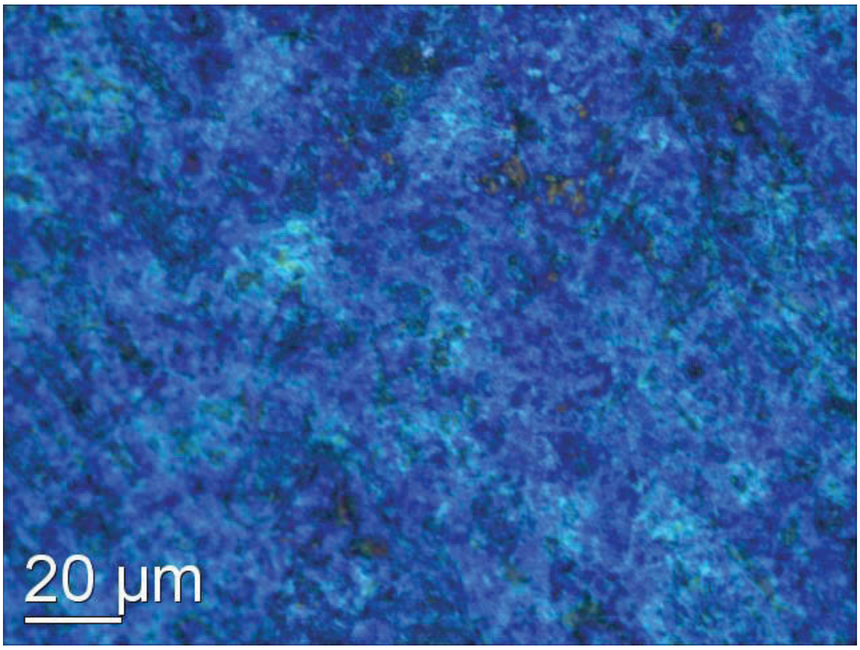

Figure 2.12 *Ti6Al4V sample anodised at 75V*

CHAPTER 3 - SOL GEL PROCESS – HYDROXYAPATITE AND ZIRCONIA COATINGS

3.1 HYDROXYAPATITE

Sol-gel is a term used to describe any process of producing ceramic materials, both single and mixed oxides, as well as non-oxides, such as nitrides, from solution as reported by Chai, C.S., K.A. Gross, and B. Ben-Nissan [83]. The sol-gel process was first recognised by Ebelman [84].

Chai *et al*. [83] reported that the sol-gel technique offers a number of advantages over other coating techniques, such as increased homogeneity, reduced sintering temperatures, and an ability to coat complex shapes easily. Furthermore, there are numerous deposition techniques that can be used to produce coatings [61].

To produce a coating, the sol-gel solution can be applied by spin, dip or spray coating. The coated substrate is then exposed to water for hydrolysis [83]. During this process hydroxides or hydrated oxides form and gelation occurs to form a three-dimensional network [83]. Further heating of the resulting gel removes any residual organic material and induces the conversion to the oxide state under oxidising conditions [5].

The sol-gel route of hydroxyapatite production is based upon the initial work of Masuda, Y., K. Matubara, and S. Sakka [85] in powder production. Later development of hydroxyapatite indicated that to produce high purity hydroxyapatite sol-gel without the calcium oxide phase present requires the sol-gel solutions to be aged for a period of time before deposition onto substrate materials and subsequent hydrolysis and heat treatment [86].

3.1.1 HYDROXYAPATITE PRODUCTION METHODS

P. Ducheyne, L.L. Hench, A. Kagan, M. Martens, A. Burssens and J.C. Miller [87] proposed a route for the production of hydroxyapatite coatings on implants which was extended to fluoro apatite/hydroxyapatite coatings by Partenfelder *et al*. [88]. If the mixture is coated on a titanium substrate, the resulting film composition is slightly different. For thin films, XRD diffractograms show the formation of a β-tricalcium phosphate phase.

The β-tricalcium phosphate phase originates from the chemical reactions that occur at the hydroxyapatite/titanium dioxide interface: the calcium of the hydroxyapatite reacts with the titanium substrate to form calcium titanate ($CaTiO_3$). The stoichiometry of hydroxyapatite is no longer fulfilled; it becomes calcium deficient and a β-tricalcium phosphate phase appears [89, 90].

In a second route, partially hydrolysed phosphoric acid esters were used [6]. These esters offer a compromise between the stable phosphate esters and the highly reactive phosphoric acid [91, 92]. Weng, W. and J.L. Baptista used a mixture of mono- and di-alkyl phosphates, $OP(OR)_X(OH)_{3-X}$ (X=1, 2), in combination with calcium nitrate [93], calcium glycoxide [94] and calcium acetate [95]. These esters are obtained by dissolving P_2O_5 in the parent alcohol (mainly ethanol and butanol). The solution is aged for 24 hours to let the reaction run to completion. It is then mixed with a calcium solution and stabilised with acetic acid to prevent precipitation. The calcium phosphate ratio is set to 1.67 [6].

In another method, triethyl phosphite $P(OEt)_3$ and calcium diethoxide $Ca(OEt)_2$ were dissolved in a mixture of ethanol and ethanediol [85]. The high moisture sensitivity of $Ca(OEt)_2$ makes a maturation period of at least 24 hours under dry nitrogen necessary.

Further investigations into the process show that the time period between the mixing of the precursors and heating to remove the solvent can significantly alter the composition of the product [90, 96, 97]. For example, triethyl phosphite takes 24 hours or more to form a mixture of stable intermediate compounds, which after thermal decomposition results in single-phase hydroxyapatite [98-100]. If time periods of less than 24 hours are employed, the result is a mixture of hydroxyapatite and calcium oxide. The preliminary results of the sol containing diethyl hydrogen phosphonate and calcium diethoxide at elevated temperatures were encouraging, giving rise to monophasic hydroxyapatite [101].

Xiao-Xiang Wang, Satoshi Hayakawa, Kanji Tsuru, and Akiyoshi Osaka [102] investigated the deposition of apatite on varying oxide forming titanium substrates with the intention of improving the bioactivity of the layer formed. Jin-Ming Wu, Satoshi Hayakawa, Kanji Tsuru and Akiyoshi Osaka [103] using similar surface modification techniques treated titanium substrates with hydrogen peroxide solutions at low temperatures to obtain titania layers with varying amounts of anatase and rutile in the oxide film formed in an effort to improve the bioactivity of the oxide film formed. The oxide film formed was found to be bioactive regardless of the fraction of rutile and anatase in the film.

3.2 HYDROXYAPATITE EXPERIMENTAL METHOD

This experimental procedure and manufacture of the hydroxyapatite sol-gel is based on the work of Milev, A., G.S.K. Kannangara, and B. Ben-Nissan [101].

Reaction solutions: Solutions were prepared by dissolving calcium diethoxide (Kojundo Chemical Lab. Japan > 99% purity) in a solvent containing 1:1 molar ratio of ethylene glycol (Fluka, > 99.5% purity) and acetic acid (Sigma > 99.7%

purity). When the calcium diethoxide was completely dissolved, a stoichiometric quantity of diethyl hydrogen-phosphonate (DHP) (Sigma > 98% purity) was added directly into the solution while stirring. Due to the hygroscopic nature of calcium diethoxide, the preparation was conducted in a glove box containing purified dry nitrogen.

3.2.1 HYDROXYAPATITE COATING PROCEDURE

All titanium samples were ultrasonically cleaned in distilled water for a period of five minutes before drying in a 70°C oven for 20 minutes. The samples were then placed on a spin coater (Headway Research USA) and solution was applied via a dropper onto the surface of the sample. The samples were then spun for 10 seconds at 3000 rpm. At this time, sol-gel was reapplied via the previous method and the samples were spun for a further 10 seconds.

Hydroxyapatite- (HAp) coated samples underwent solution aging for 24 hours at 70°C. Samples were fired at 300°C for 24 hours and then finally fired for two hours at 550°C. These coating procedures are based on the previous work of Chai and Ben-Nissan [90, 104], Torpy [105] and Milev *et al*. [101, 106]. Figure 3.1 shows the full sequence for the processing of coating a titanium sample with hydroxyapatite using an anodic oxide layer.

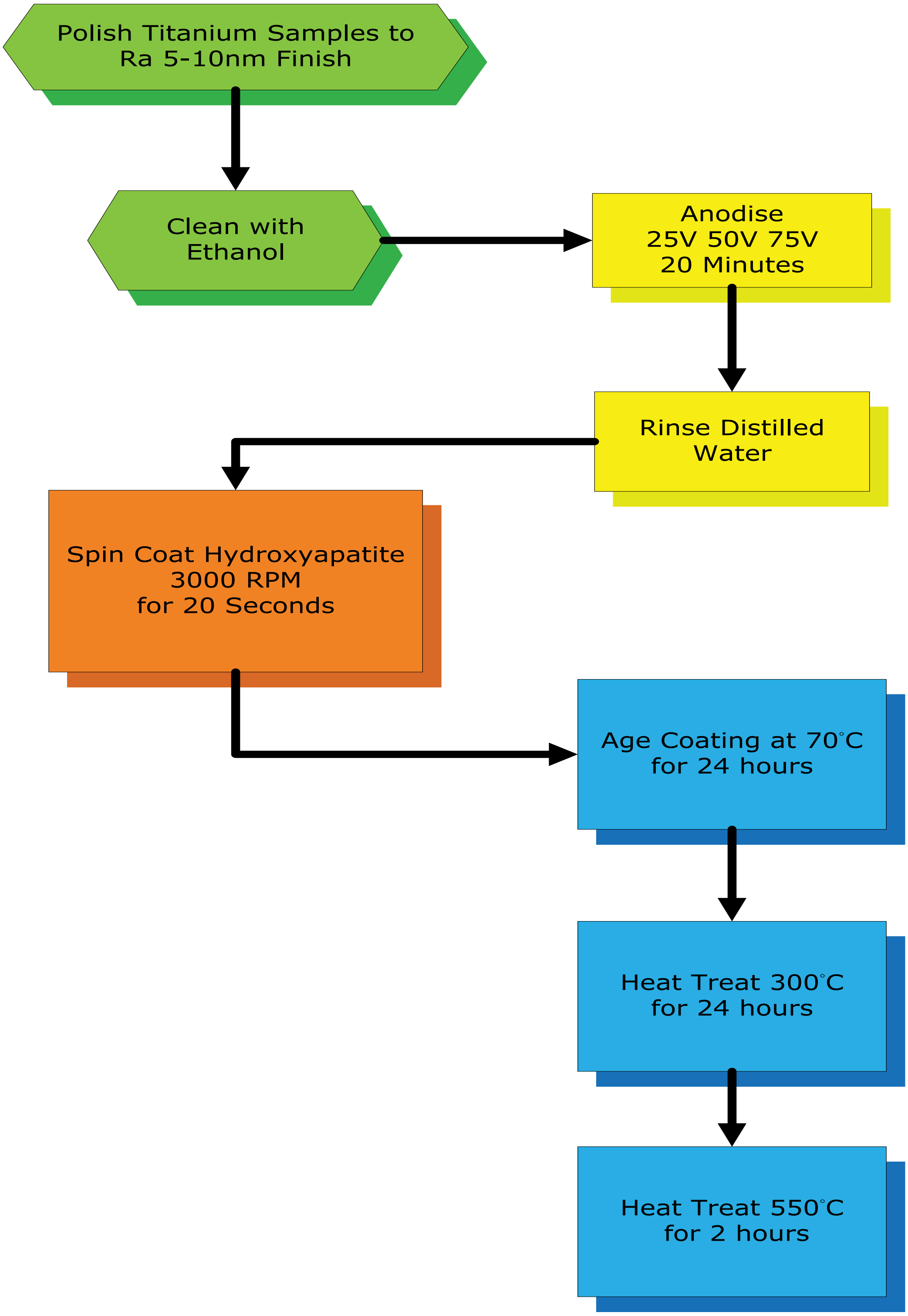

Figure 3.1 *Hydroxyapatite sol gel flowchart*

3.3 ZIRCONIA

The ZrO_2 structure is a face-centred cubic (FCC) structure where the Zr^{2+} cations assume the FCC lattice sites and the O^{2-} anions occupy all eight tetrahedral sites [107]. The biggest problem with the use of ceramics in structural and biomedical applications is their low fracture toughness values. For traditional ceramics they range between 0.5 to 3.0 $MPa.m^{1/2}$ [107], while zirconia values as shown in Table 4.1 range from 10 $MPa.m^{1/2}$ for tetragonal zirconia polycrystals (TZP) to 3.0 $MPa.m^{1/2}$ for cubic stabilised zirconia doped with yttria oxide (Y_2O_3), which is also known as Y-CSZ.

Ceramic fracture toughness values may be increased by (1) the presence of micro voids [107], (2) the presence of localised regions that are in compression, and (3) by fibre reinforcement [107]. Partially stabilised zirconia (PSZ) has increased toughness and strength over ZrO_2 due to the partially stabilised cubic ZrO_2 structure having a doping addition of either MgO, CaO, or Y_2O_3 [107].

Tetragonal zirconia polycrystals (TZP) in addition to the doping of the ZrO_2, stabilise the cubic and tetragonal phases, which lowers the temperature of the tetragonal to monoclinic transformation. It is this phase transformation from the metastable tetragonal to monoclinic phase of crystalline ZrO_2 that prevents its application over a wide temperature range. The high-temperature tetragonal phase can be stabilised at room temperature by the addition of doping agents such as Y_2O_3, MgO, CaO, CeO_2 and Yb_2O_3 to ensure the improved properties of ZrO_2 are retained [45, 108-110].

3.3.1 ZIRCONIA COATINGS

Sol-gel-derived ceramic coatings have a variety of uses, due to their ease of production and ability to coat complex shapes. The sol-gel's nanocrystalline grain structure can result in improved mechanical properties of the coating [1, 111-113]. Sergo, V., Pezzotti, G., Sbaizero, O., and Nishida, T.[114] investigated the influence of grain structure on alumina and zirconia composites with the tensile stresses in zirconia showing no clear agreement with the volume fracture and increases with increasing zirconia grain size, this observation when combined with the nanoscale grain structure of the zirconia sol gel coating point towards the low tensile stresses existing in the sol coatings.

Guicciardi, S., Nagliati, M., Melandri, C., Pezzotti, G. and Sciti, D., [115] also argue that due to residual compressive stresses the fracture strength of the laminated composite was higher than the strength of the outer layer material. The sol gel coating of zirconia on the anodised titanium substrates is itself a laminated structure.

Sol-gel ceramic coatings have been shown to be effective barriers against high-temperature oxidation [1, 116-119], and corrosion by NaCl and Sulphuric acid solutions [116-118, 120-122]. These properties suggest zirconia ceramic coatings for metallic implants may be effective in relation to *in vivo* metal ion release and subsequent biological effects [122]. Metal-based implants are used in load-bearing applications under which the response of the surface treatments to mechanical deformation is important. Delamination or perforation of a protective coating exposes the substrate to accelerated wear or corrosion, and the released coating particles may act to accelerate wear or provoke a negative host response [1, 121-123].

Phase-stabilised zirconia in the bulk form (Y-TZP) is an accepted bio-inert implant that suffers from long-term degradation of its mechanical properties [1]. Submicron thick sol-gel zirconia films crystallise directly into the tetragonal/cubic phases without the need to add phase stabilisers into the zirconia film [117, 118, 124, 125].

3.4 ZIRCONIA EXPERIMENTAL PROCEDURE

The experimental procedure and manufacture of the zirconia sol-gel is the based on the previous work of Paterson, M.J. and B. Ben-Nissan [126, 127], Anast, M. Bell, J. Bell, T. and Ben-Nissan, B. [125, 128] and Torpy [105]. The zirconia sol-gel initially produced was extremely viscous, leading to problems with surface wetting of the samples regardless of surface pre-treatments. This led to incomplete surface coverage of the samples. Modification of this solution to reduce the viscosity to a viscosity of 10 Centipoises (CPS) for the solution enabled the complete surface coverage with no cracking after firing on all samples.

All titanium samples were ultrasonically cleaned in distilled water for a period of five minutes before drying in a 70°C Oven for 20 minutes. The samples were then placed on a spin coater (Headway Research USA) and solution was applied via a dropper onto the surface of the sample. The samples were then spun for 10 seconds at 3000 rpm. At this time, sol-gel was reapplied via the previous method and the samples were spun for a further 10 seconds.

Zirconia-coated samples underwent solution aging for 1 hour at 70°C. Samples were then fired at 300°C for 24 hours and then heat-treated for two hours at 550°C. Figure 3.2 shows a graphical representation of the entire zirconia coating process from the initial titanium sample preparation to the final zirconia heat treatment.

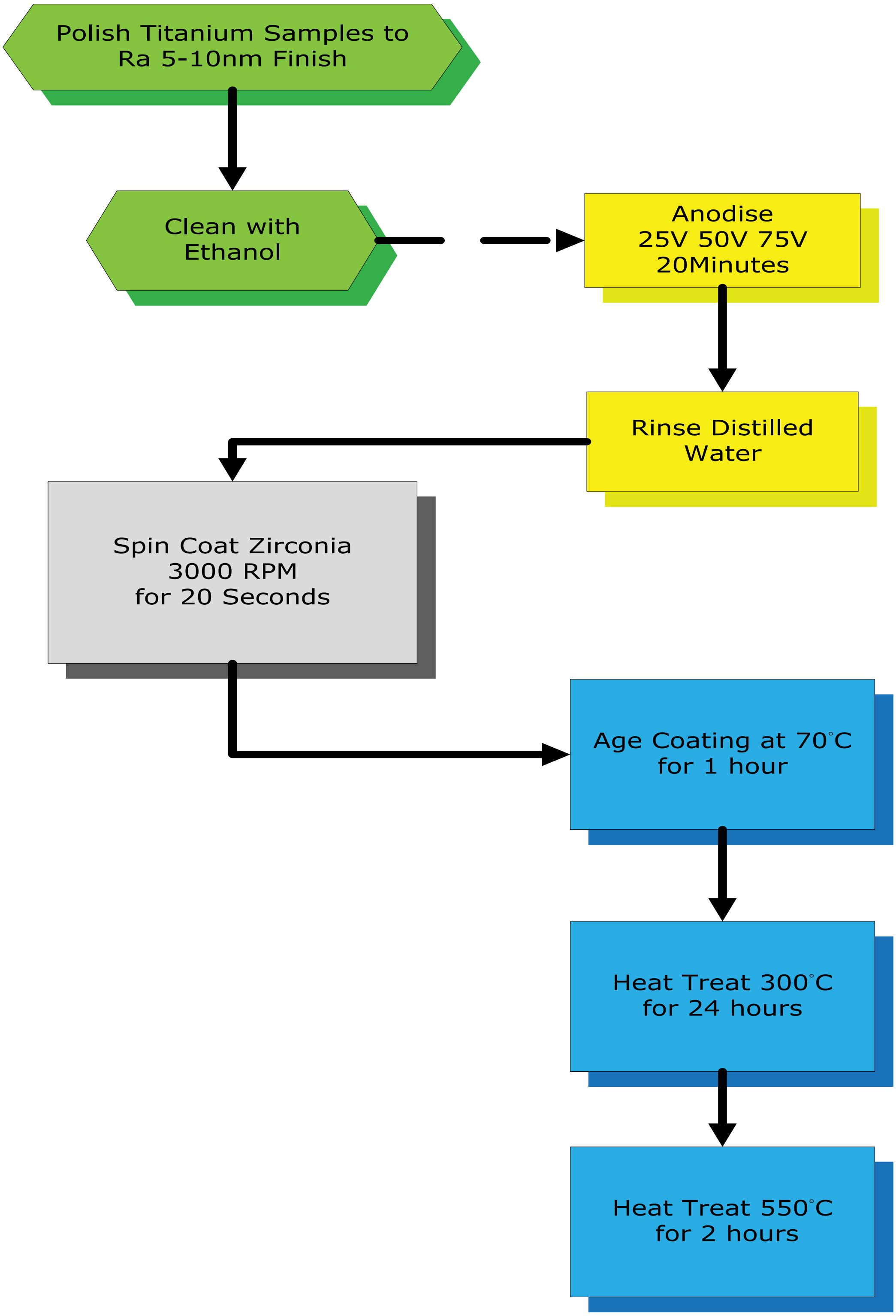

Figure 3.2 *Zirconia sol gel flowchart*

3.5 ZIRCONIA SOL GEL DISCUSSION

The zirconia solution based on previous work by Paterson *et al*. [126, 127], Anast *et al*. [125, 128] and Torpy [105] was designed for high-temperature oxidation applications. The zirconia sol-gel initially produced was extremely viscous, leading to a problem of surface wetting of the samples regardless of surface pre-treatments. This led to incomplete surface coverage of the samples. Modification of this solution with the solvent 1- Butanol to reduce the viscosity of the solution enabled the complete surface coverage after firing on all samples the ideal viscosity was found to be in the range of 10 -12 Centipoises (CPS) with no cracking evident using an ALPHA Series L viscometer with a low viscosity adaptor to allow for viscosity measurements down to 1 centipoise.

Kirk *et al*. [1] reported that zirconia sol-gel films of approximate thickness of 100 nm were found to be cracked extensively, and attributed this cracking to an isotopic biaxial tensile stress in the coating, due to full in-plane relief of shrinkage stresses (capillary) during drying and annealing [1]. Whereas Mehner, A. Klumper-Westkamp, H. Hoffmann, F. and Mayr, P. [129] and Scherer [130] found the critical film thickness of zirconia sol gel films to be 200nm.

The initial films produced for the tribology tests and micro-adhesion tests were around 200 nm thick and after firing developed cracks as in figures 3.3 and 3.4 while figure 3.5 shows the same anodised substrate with the modified zirconia sol-gel solution producing a crack free 100 nm zirconia coating that is in contrast with Kirk *et al*. [1] but in agreement with the work of Mehner *et al.* and Scherer. [129, 130]

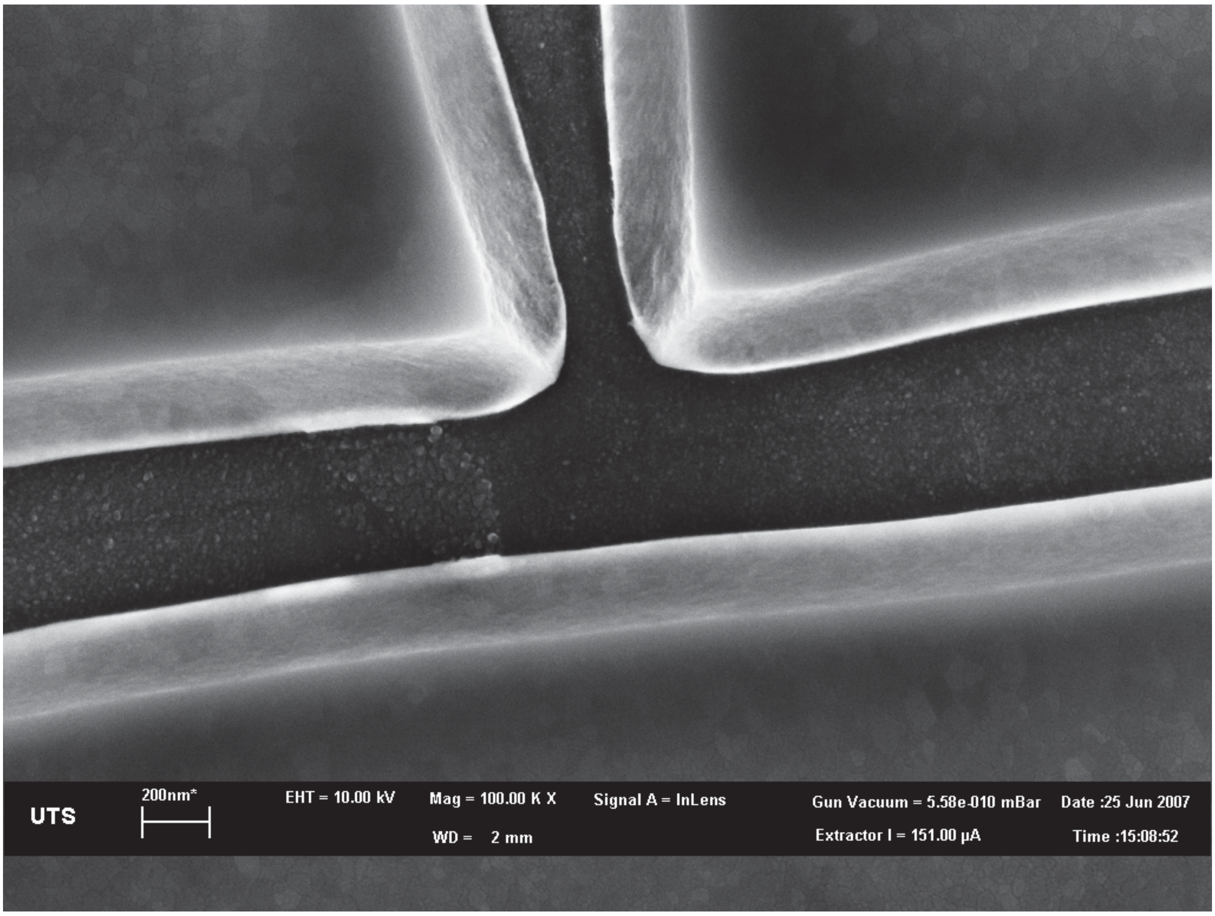

Figure 3.3 *SEM of 200nm thick zirconia sol gel coating on 75V anodised C.P. titanium showing cracking in coating.*

The surface finish of the substrate was critical in the ability of the zirconia sol gel to approach the critical film thickness of 200 nm with the roughest surface produced during testing the 75 volt anodised sample producing the greatest amount of cracking in the surface of the zirconia sol gel coating when approaching the 200 nm critical thickness limit. While the C.P titanium sample that was un-anodised produced the least amount of cracking as it approached the critical thickness limit as evidenced in figures 3.4 and 3.6.

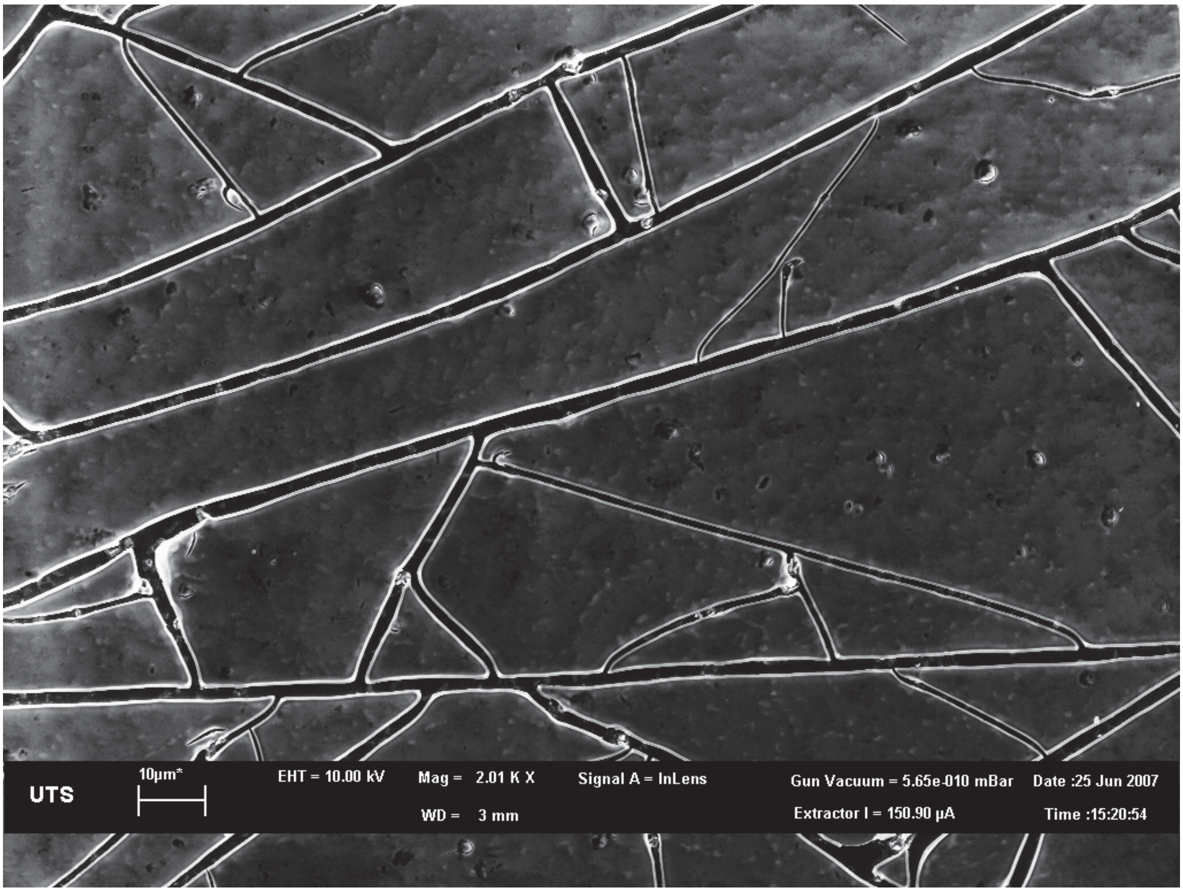

Figure 3.4 *SEM of 200nm thick zirconia sol gel coating on 75V anodised C.P. titanium showing cracking in coating.*

Figure 3.5 shows the transparent nature of the zirconia coating allowing the anodised layer to be clearly seen, with the differing colours giving an overview of the surface roughness and thickness of the titanium oxide formed after anodising at 75 volts. The increasing thickness of the titanium oxide layer formed by anodising at higher voltages results in surface colour changes due to the refraction of light a change in thickness of several nanometres can result in a colour change as evidenced in figure 3.5.

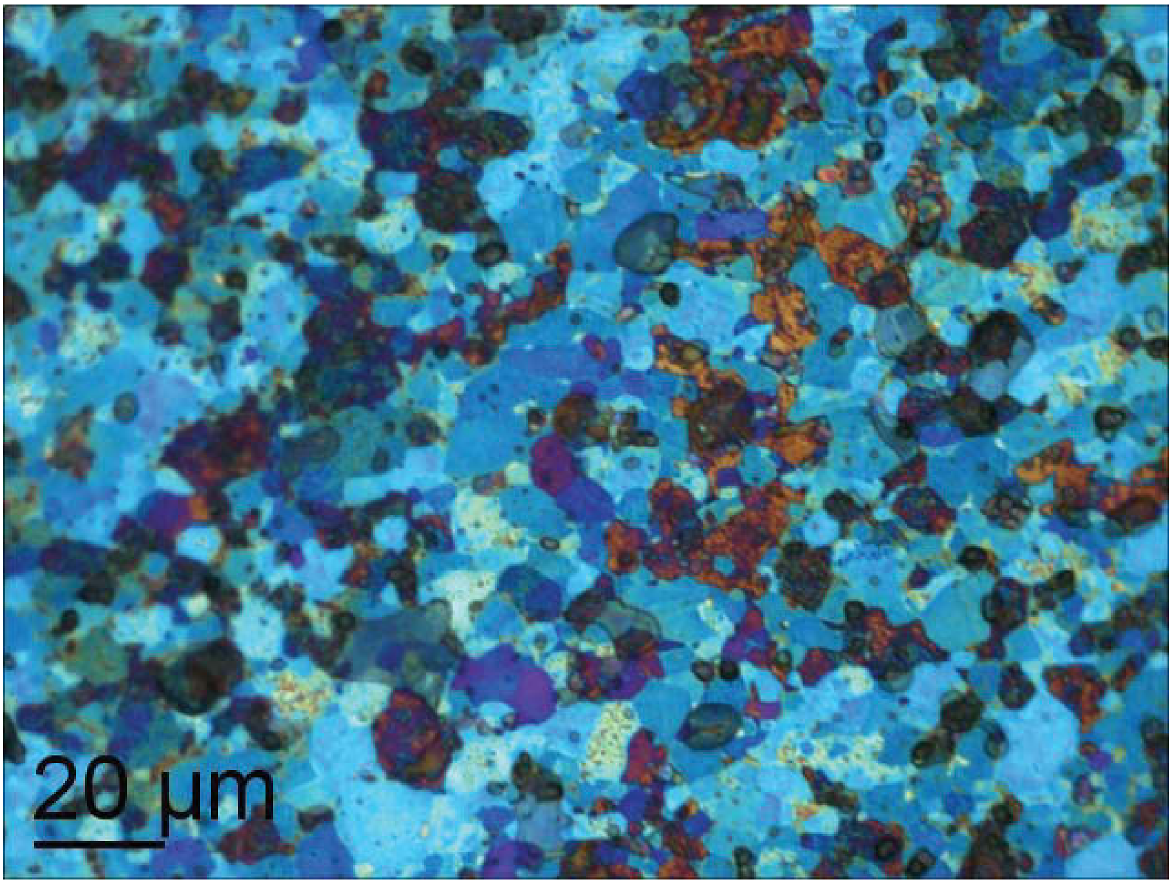

Figure 3.5 *Optical micrograph of 100nm thick zirconia sol gel coating on 75V anodised C.P. titanium showing crack free coating.*

Micro adhesion testing was carried out on the cracked and crack free samples to see if there was any difference in the coatings adhesion properties. Figures 3.6 and 3.7 show the effects of reduced viscosity on the cracking of the zirconia coating.

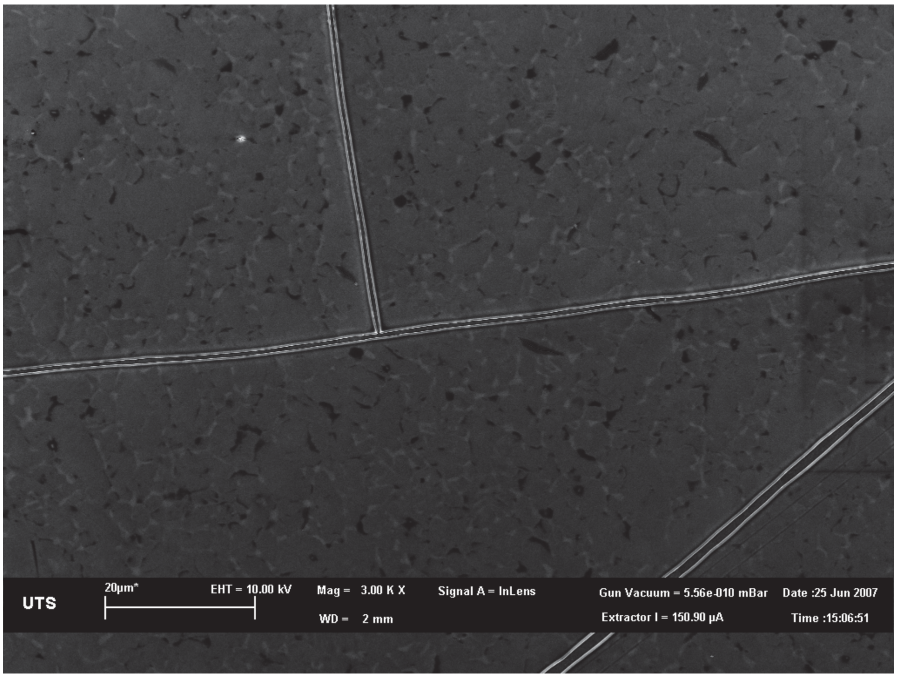

Figure 3.6 *SEM of 200nm thick zirconia sol gel coating on C.P. titanium substrate showing reduced cracking in zirconia coating with reduced viscosity (20CPS)*

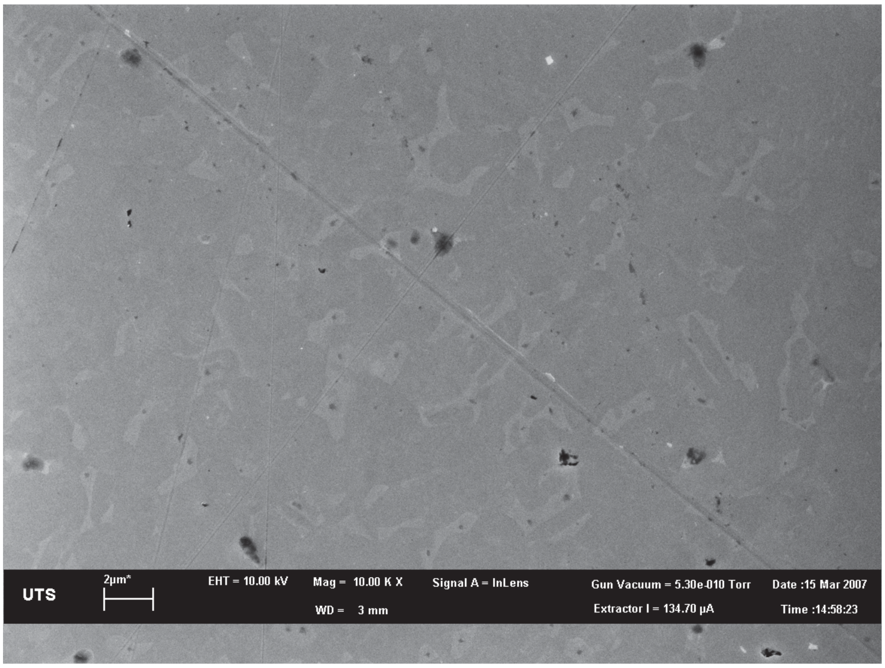

Figure 3.7 *SEM of 200nm thick zirconia sol gel coating on C.P. titanium substrate showing no cracking in zirconia coating with final viscosity (10-12 CPS).*

CHAPTER 4 – BIOCOMPATIBLE INTERFACES

4.1 CELLULAR ADHESION AND BIOCOMPATIBILITY

The adhesion of cells is involved with many natural phenomena from maintenance of tissue structure, immune responses, metastasis, and wound healing in addition to tissue integration of biomaterials. [131, 132] The biocompatibility is closely related to cell behaviour in contact with biomaterials and to the cell adhesion to the biomaterial surface. [131, 132] Surface characteristics of the biomaterials, their topography, chemistry or surface energy, all play an essential part in osteoblast adhesion on biomaterials. Table 4.1 shows the body's cellular products involved in the adhesion process and the receptors and responses to them. [133]

Properties of the Osteoblast Phenotype

Products;	***Receptors/responses to;***
Alkaline Phosphatase	**Parathyroid Hormone**
Type 1 Collagen	**Prostaglandins**
Osteocalcin	**$1,25(OH)_2D_3$**
Osteopontin	**Epidermal and transforming growth factors**
Osteonectin	**Interleukin 1**
Prostanoids	**Tumor Necrosis Factors**
Osteoclast stimulating factor	**Retinoids**
Growth Factors	

Table 4.1 *Properties of the Osteoblast Phenotype From Cell Biology of Bone by Martin et al. [133]*

Thus attachment, adhesion and spreading belong to the first phase of cell/material interactions and the quality of this first phase will influence the cell's capacity to proliferate and to differentiate itself on contact with the implant. Cell adhesion, viability and proliferation, as well as expression of alkaline phosphatase (ALP is an indicator of bone formation) were assessed as indicators of biocompatibility. [134]

The osteoblast adhesion on materials is vitally important in gaining an understanding of the bone/biomaterial interface it is also critical in gaining an understanding of the cell/biomaterial interface regarding the implantation of the orthopaedic biomaterials [131, 132] which is why this technique was covered in this section of the thesis.

4.2 IMPLANT INTERFACE DESIGN

Implant materials are being increasingly designed to provide the optimal pore structure for osteointegration to occur, and a subsequent increase in the bone to implant bond as stated by Zreiqat, H. Roest, R. Valenzuela, S. Milev, A. and Ben-Nissan, B. [135, 136] results in an increase in the surface bioactivity have been achieved by the creation of micro and nano-textured surfaces. While these provide a surface conducive to bone in growth, the material used needs more study with regard to the effect on cell activity and the changes which occur to intracellular processes in the presence of these implant materials. The following series of characterisation studies is designed to observe the changes occurring to the two osteoblast cell lines (Mg63 and Saos-2) when cultured on sol –gel surfaces, which can be used as implant coatings. [134]

4.3 OSTEOBLASTS ADHESION

Osteoblasts are cells which synthesize the bone matrix as stated by Martin et al. [133] but it is now recognized that the osteoblast family also comprises the related osteocyte and bone cell lining, and may include other yet unrecognized functional groups and types. [133] The adhesion molecules can be characterized by their capacity to interact with specific ligands. [131, 132] These ligands may be situated on the membranes of neighbouring cells or they may be extracellular matrix proteins. [131, 132] adhesion molecules belong to different families. The four main classes are immunoglobin superfamily, cadherins, selectins and integrins. [131, 132] it should also be noted that the increased surface roughness achieved by the galvanostatic mode of anodising covered in section 2.5 may provide a more advantageous surface for the adhesion of osteoblasts, and this is in covered in more depth in section 4.6 on cell growth.

4.4 OSTEOBLAST CELL CULTURING AND BIO-ASSAYS

Osteoclasts and Osteoblasts have a complementary function in the dissolution and deposition of bone respectively. Osteoblasts and mesenchmal cells have a common origin as the mesenchymal stem cells can differentiate into Osteoblasts.[131, 137]

Mg63 and Saos-2 are human osteosarcoma cell lines. Mg63 is derived from a 14 year old male Caucasian and Saos-2 is obtained from an 11 year old female Caucasian.

4.4.1 EXPERIMENTAL METHOD

Preliminary cell culture studies were conducted on the Osteoblast like – Human osteosarcoma cell lines Mg63 and Saos-2 (ATCC, USA) which were placed onto coated and uncoated titanium disks, to ensure that materials do not cause a loss in the expression of the osteoblast phenotype, and that the surfaces do not have any cytotoxic effects. The disks were sterilised prior to cell culture, using dry oven sterilisation at 200 degrees C for 2 hours.

Cell culture passages 1- 6 are used for the analysis, and each passage is conducted using trypsin/EDTA for 10 minutes, 5ml of the appropriate media is then added and the cells are spun down for 3.5 minutes at 1.2 rpm. Following this the solution is tipped off and the cell pellet resuspended in fresh media. Cells are counted using trypan blue and determined using a haemocytometer. The starting cell number is recorded at a concentration of 10,000 cells per ml for each experiment, and the cells are grown at intervals of 5, 10 and 14 days,

Mg63 cells are cultured in Eagles modified Essential Media (Sigma). Supplemented with a 10% Foetal Bovine Serum, Sodium Pyruvate and Sodium Carbonate. Saos-2 cells are cultured in McCoys 5A media (Sigma) supplemented with 15% Foetal Bovine Serum and L-glutamine, as per the supplied protocols. The cell culture media also had vitamin D added, as this is required in order for the cells to produce Osteocalcin. The osteocalcin concentrations are measured a Human Osteocalcin Immunoassay kit (Biosource) which measures intact osteocalcin. [134] The viability is measured using propidium iodide, and an ELISA reader. The samples are then freeze thawed to determine the total cell number. The absorbance’s are normalised using a standard curve.

The cell samples were then assessed for cell proliferation and viability using propidium iodide exclusion staining. [134]

4.5 Results and Discussion

Raw Data for Osteocalcin, a marker of bone formation

Disk 1 = C.P. Titanium (purple disk)

Disk 2= C.P. Titanium +Hap,

Disk 3= Anodised C.P. Titanium 50V (yellow)

Disk 4= Anodised C.P. Titanium 50V +Hap

Osteocalcin Concentration on Titanium Substrates

	Day 5	**Conc.**	**Day 10**	**Conc.**	**Day 14**	**Conc.**
Disk 4	0.235	9.39025	0.248	9.9226	0.238	9.5131
Disk 3	0.257	10.29115	0.353	14.2223	0.285	11.43775
Disk 2	0.253	10.12735	0.06	2.224	0.267	10.70065
Disk 1	0.252	10.0864	0.364	14.6728	0.27	10.8235
	Day 5	**Conc.**	**Day 10**	**Conc.**	**Day 14**	**Conc.**
Disk 4	0.092	3.5344	0.2	7.957	0.247	9.88165
Disk 3	0.101	3.90295	0.277	11.1101	0.262	10.4959
Disk 2	0.093	3.57535	0.287	11.5196	0.269	10.78255
Disk 1	0.101	3.90295	0.309	12.4205	0.258	10.3321

Table 4.2 *Osteocalcin Concentration Data over 14 day Period*

Osteocalcin Concentration on Titanium Substrates over 14 Days

		Day 5	**Day 10**	**Day 14**	**Standards**	**Conc. ng/ml**	**Blanks**
Saos-2	Disk 4	0.235	0.248	0.238	1.251	53	9.5131
	Disk 3	0.257	0.353	0.285	0.262	10.5	11.43775
	Disk 2	0.253	0.06	0.267	2.147	90	10.70065
	Disk 1	0.252	0.364	0.27	0.998	35	10.8235
Mg63	Disk 4	0.092	0.2	0.247	0.305	14	9.88165
	Disk 3	0.101	0.277	0.262	0.08	5	10.4959
	Disk 2	0.093	0.287	0.269	0.045	2	10.78255
	Disk 1	0.101	0.309	0.258	0.024	0	10.3321

Table 4.3 *Osteocalcin Concentration Data over 14 day Period with Standards and Blanks*

Tables 4.1 and 4.2 show that the cells produce Osteocalcin on all surfaces, Osteocalcin a marker of bone formation on all surfaces, the anodised titanium shows significantly less osteocalcin production than that of the other surfaces, with the C.P. titanium surface producing the best results. Figure 4.1 shows the osteocalcin standard curve over the 14 day period with the concentration up to 90 ng/ml.

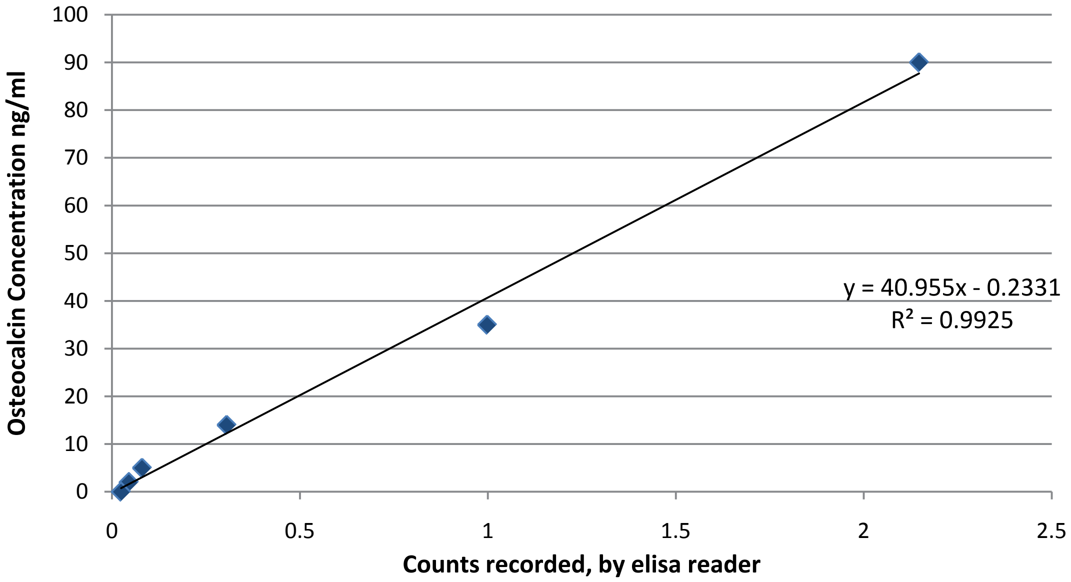

Figure 4.1 *Osteocalcin standard curve over 14 day period*

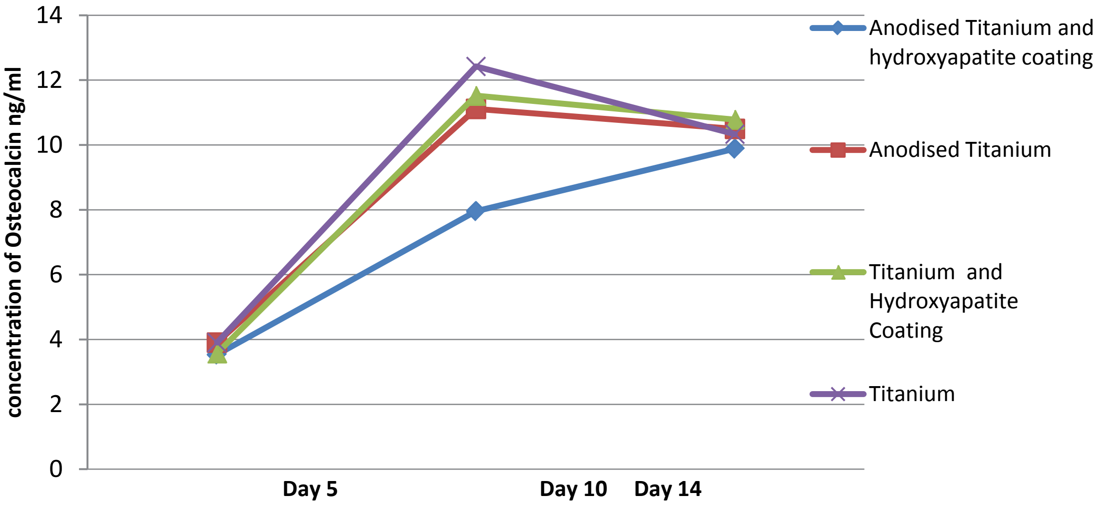

Figure 4.2 *Osteocalcin production over 14 day period*

In figure 4.2 it appears that the initial production of Osteocalcin if fairly uniform, with all surfaces being similar at the 5 day interval. Interestingly, the 14 day osteocalcin is also similar, which indicates, that the production may have ceased by 14 day. This indicates the need for an additional dose of vitamin D and that the osteocalcin begins to degrade quite rapidly once produced.

4.5.1 CELL GROWTH AND CYTOTOXITY

Figures 4.3 and 4.4 are the standard curves which are produced with Propium Iodide (PI) with known cell concentrations. The cells are freeze/thawed, to ensure cell death as PI produces fluorescence only when the cell membrane is destroyed or broken and can come into contact with the nucleus. The numbers obtained from the Elisa reader can then be used to determine the total cell number. Tables 4.5, 4.6, 4.7, 4.8 and Figures 4.5 and 4.6 show the data obtained when the Propium Iodide was used to ensure cell death and thus allow for the cells to be counted. The results also show the cell growth numbers over a 14 day period.

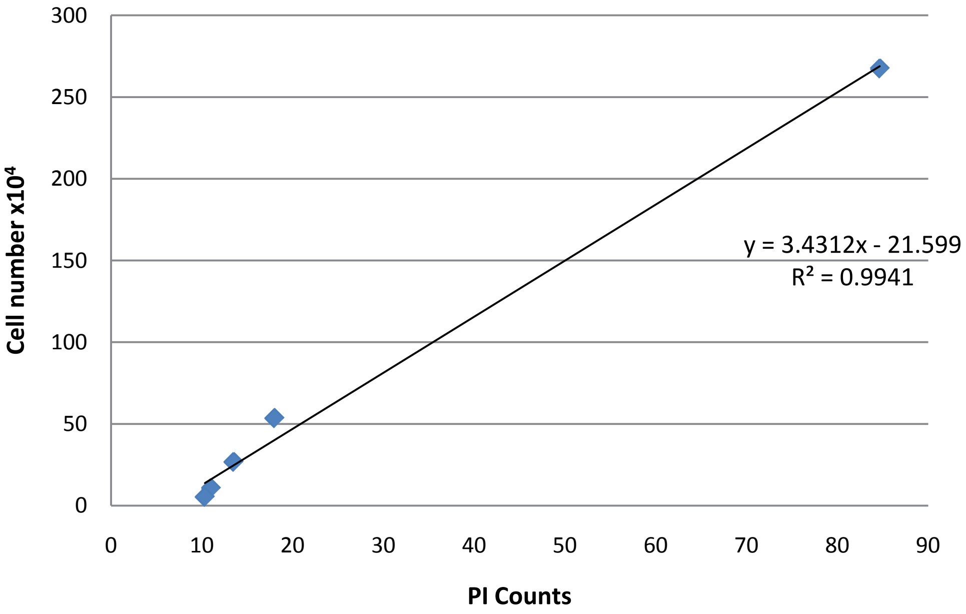

Figure 4.3 *Saos standard curve produced with Propium Iodide*

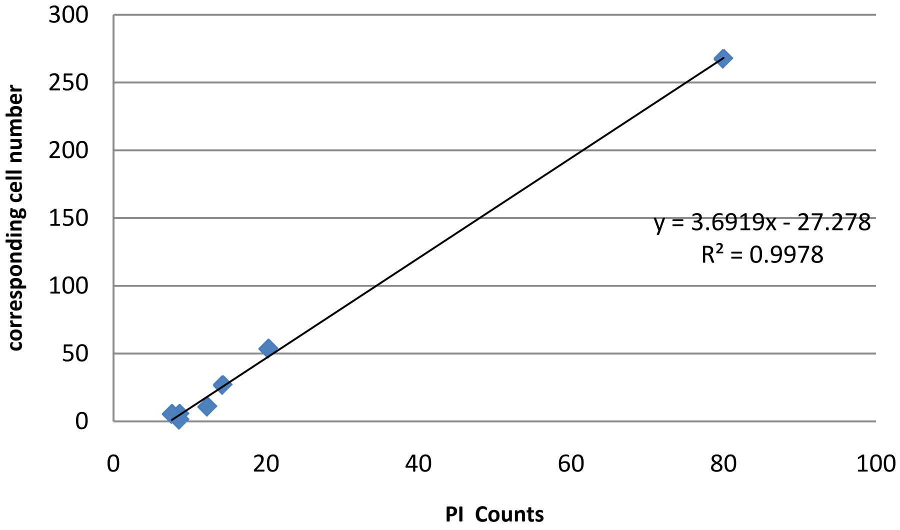

Figure 4.4 *Mg 63 standard curve produced with Propium Iodide*

SAOS Raw Data on Titanium Substrates

Titanium Saos day 14 supernatant				**Titanium Saos day 14 adhered**			
Disk 1	**Disk 2**	**Disk 3**	**Disk 4**	**Disk 1**	**Disk 2**	**Disk 3**	**Disk 4**
4	5	6	6	14	20	22	19
7	7	7	7	16	19	17	14
8	9	8	9	16	18	22	18
Titanium Saos day 10 supernatant				**Titanium Saos day 10 adhered**			
3	9	7	6	10	16	11	12
7	7	7	7	11	12	12	8
8	8	8	7	9	10	11	11
Titanium Saos day 5 supernatant				**Titanium Saos day 5 adhered**			
3	4	5	6	8	13	9	6
6	7	7	6	8	10	8	11
8	7	6	6	11	7	9	8

Table 4.4 *Saos raw data produced with Propium Iodide*

	Adhered Saos Averages			
Days	**Disk 1**	**Disk 2**	**Disk 3**	**Disk 4**
14	15.33	19	20.33	17
10	10	12.66	11.33	10.33
5	9	10	8.66	8.33

Table 4.5 *Saos raw data averages produced with Propium iodide*

MG63 Raw Data on Titanium Substrates

Titanium Mg63 day 14 supernatant				**Titanium Mg63 day 14 adhered**			
Disk 1	**Disk 2**	**Disk 3**	**Disk 4**	**Disk 1**	**Disk 2**	**Disk 3**	**Disk 4**
4	3	4	5	19	16	22	17
7	8	8	6	22	20	21	22
8	8	8	7	22	20	17	18
Titanium Mg63 day 10 supernatant				**Titanium Mg63 day 10 adhered**			
4	4	6	5	16	13	19	18
7	6	8	5	20	21	19	17
7	6	7	7	22	20	17	14
Titanium Mg63 day 5 supernatant				**Titanium Mg63 day 5 adhered**			
4	3	3	4	9	10	10	10
6	6	6	6	12	12	11	11
6	7	7	6	12	12	13	5

Table 4.6 *Mg63 raw data produced with Propium Iodide*

	Adhered Mg63 Averages			
Days	**Disk 1**	**Disk 2**	**Disk 3**	**Disk 4**
14	21	18.66	20	19
10	19.33	18	18.33	16.66
5	11	11.33	11.33	8.66

Table 4.7 *Mg63 raw data averages produced with Propium iodide*

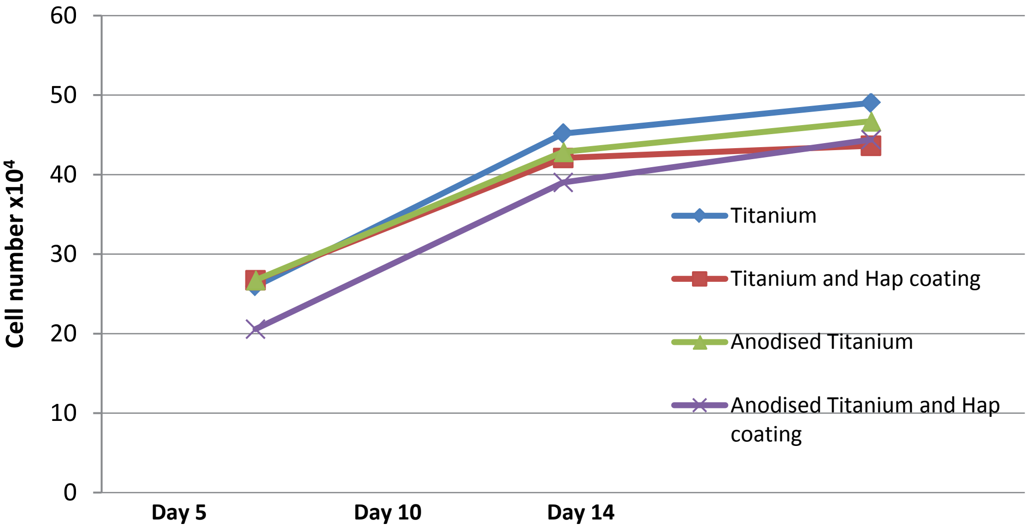

Figure 4.5 *Mg63 cell numbers produced with Propium iodide*

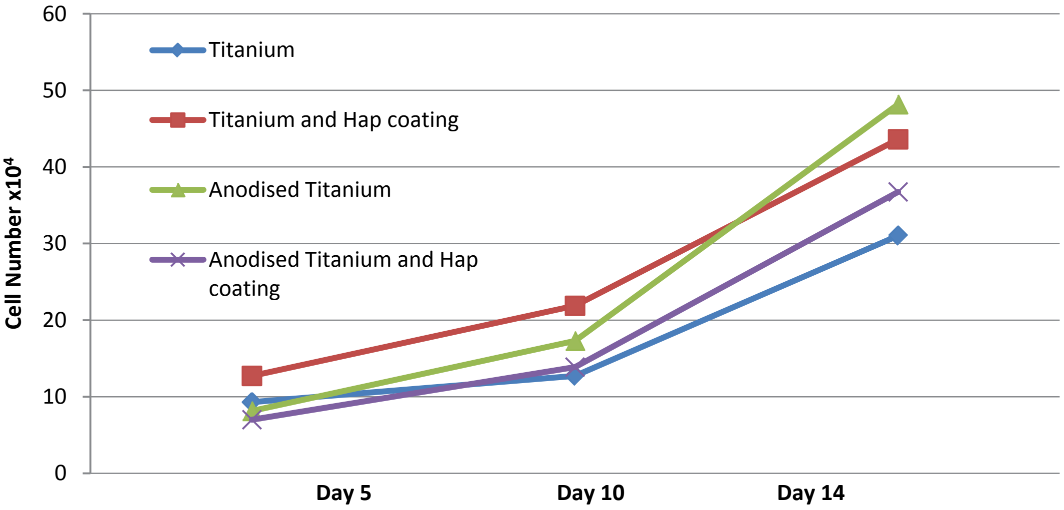

Figure 4.6 *Saos cell numbers produced with Propium iodide*

4.6 CELL GROWTH CONCLUSIONS

Osteoblast adhesion as termed by Anselme [131, 132] is a complex situation that involves differing phenomena from the attachment phase which occurs rapidly to short term events such as chemical linkages between cells and materials involving ionic forces [131, 132] van der walls forces.

The adhesion phase that takes place over a longer time frame involving various biological materials, matrix proteins cell membrane proteins and cytoskeleton proteins which all interact together. [131, 132]

Das, K., S. Bose, and A. Bandyopadhyay [138] with respect to titanium substrates have stated that higher surface roughness, low contact angle, improved wettability and high surface energy lead to better cell attachment. This is also in agreement with the work of Eisenbarth, E. Velten, D. Muller, M. Thull, R. and Breme, J. [139] , Kim, Yeonhee, Jang, Jun-Hyeog, Ku, Young, Koak, Jae-Young, Chang Ik-Tae Kim, Hyoun-Ee Lee, Jae-Bong and Heo, Seong-Joo [140] and Sul. [141-143]

The surface roughness of the anodised titanium samples tested in the Saos and Mg63 cell tests was 0.026 μm to 0.028 μm and for the titanium samples 0.005 μm to 0.006 μm and when compared to the work of Das et al. Sul and Kim et al. [138, 140, 141] who surface Ra ranged from 0.75 μm to 4.68 μm there is a significant difference in the surface roughness of the samples tested. Surface roughness was measured as previously covered in section 2.5 using a (ANSTO) stylus profilometer.

As stated previously in Das et al. the increased surface roughness results in better cell attachment and thus adhesion. So the fact that cells adhered on all the surfaces examined in this study despite the very low surface roughness values indicate that the substrates themselves allowed for osteoblast adhesion in both cell lines.

The number of dead cells present in the Saos and Mg63 PI tests was below the linearity of the standard curve, so levels of cell death were too low to indicate cytotoxic effects. The adhered cells are also very similar for all of the surfaces tested.

CHAPTER 5 – INTERFACE ANALYSIS WITH SIMS

5.1 SECONDARY MASS ION SPECTROMETRY (SIMS)

Secondary Ion Mass Spectrometry (SIMS) is a specialized analytical tool that combines high spatial resolution and high sensitivity. This technique uses a highly focused ion beam of caesium ions which 'sputters' material from a selected domain on the surface of interest, i.e. the zirconia and hydroxyapatite coated titanium surfaces in this study. The 'secondary ions' which are ejected from the sample are passed through a mass spectrometer which separates the ion according to their mass/charge ratio: in effect providing a chemical analysis of a very small sampling volume. [144, 145]

5.1.1 SECONDARY MASS ION SPECTROMETRY (SIMS) METHOD

SIMS measurements were performed using a CAMECA IMS 5f secondary ion mass spectrometer. A Cs+ primary ion beam was used for depth profiling by rastering an area of 250 x 250 μm^2 on the surface of the sample with net impact energy of 3keV. To eliminate any edge effects the actual analysis area was dictated by aperture settings which restricted the measurement of positive secondary ions to a 100μm diameter circular area within the rastered region. The measurement of MCs^+ molecular secondary ions, where M denotes the element of interest, was used for all samples as it can reduce the contribution of matrix effects on the SIMS results. [146] The depths of the SIMS craters were measured with an Alpha-step stylus profilometer in order to determine the average sputter rate of the analysis.

5.2 RESULTS AND DISCUSSION

Figure 5.1 shows the sputtered area of the SIMS instrument which is roughly 250 x 250μm resulting from a primary beam current of 10nA and an acquisition time of 1827 seconds. The crater floor shows the Ti6Al4V alloy itself after the zirconia coating has been sputtered off.

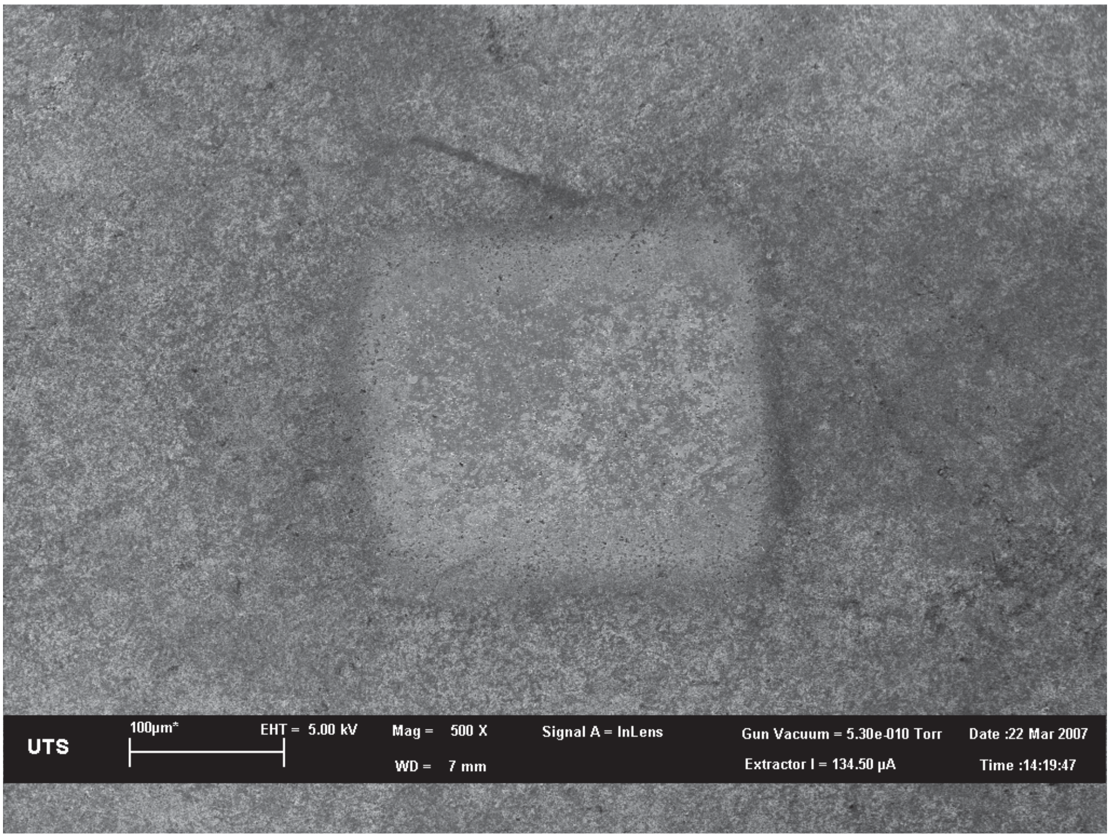

Figure 5.1 *Ti6Al4V Alloy with zirconia coating showing sputtered area through zirconia coating with the scale at 100 microns.*

This is further evident in figure 5.2 showing at higher magnification the interior of the sputtered crater, which is the pure Ti6Al4V alloy after sputtering of the sample in which the alpha and beta phases appear in the grain structure. The alpha phase appears as a whitish columnar type microstructure while the beta phase as a greyish matrix this as verified by using the SEM-EDS.

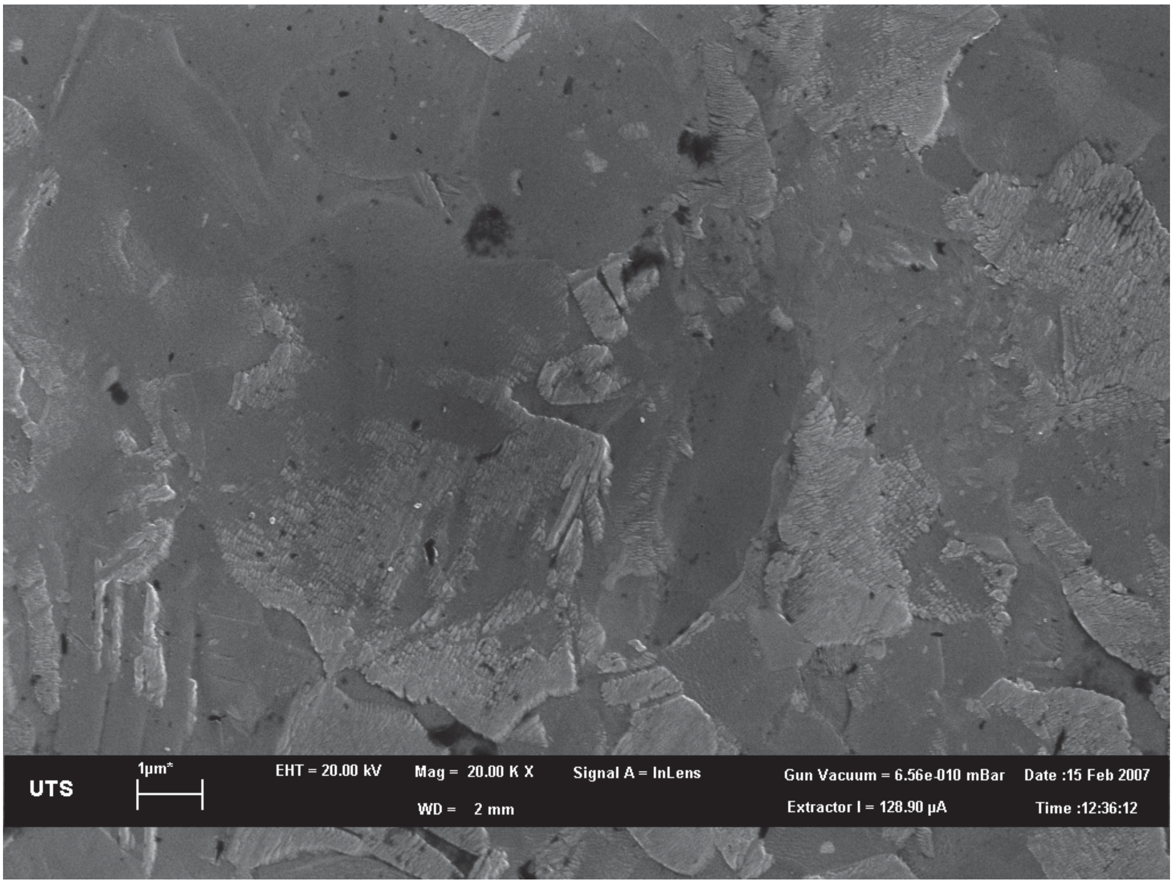

Figure 5.2 *Interior of SIMS sputtered area on Ti6Al4V alloy coated with zirconia showing alpha and beta grains.*

Figure 5.3 shows the interface area between the SIMS crater and the zirconia coating on a Ti6Al4V sample with the porosity that is generated at the interface of the SIMS crater. This also shows to some extent the fine microstructure of the sol gel coated zirconia. All samples tested both anodised and pure Ti6Al4V samples demonstrated similar type micrographs to the ones shown in figures 5.1, 5.2 and 5.3 with only the depth of the craters being a significant difference between the samples with the anodised sample in figure 5.4 showing a less well defined region between unsputtered and sputtered areas.

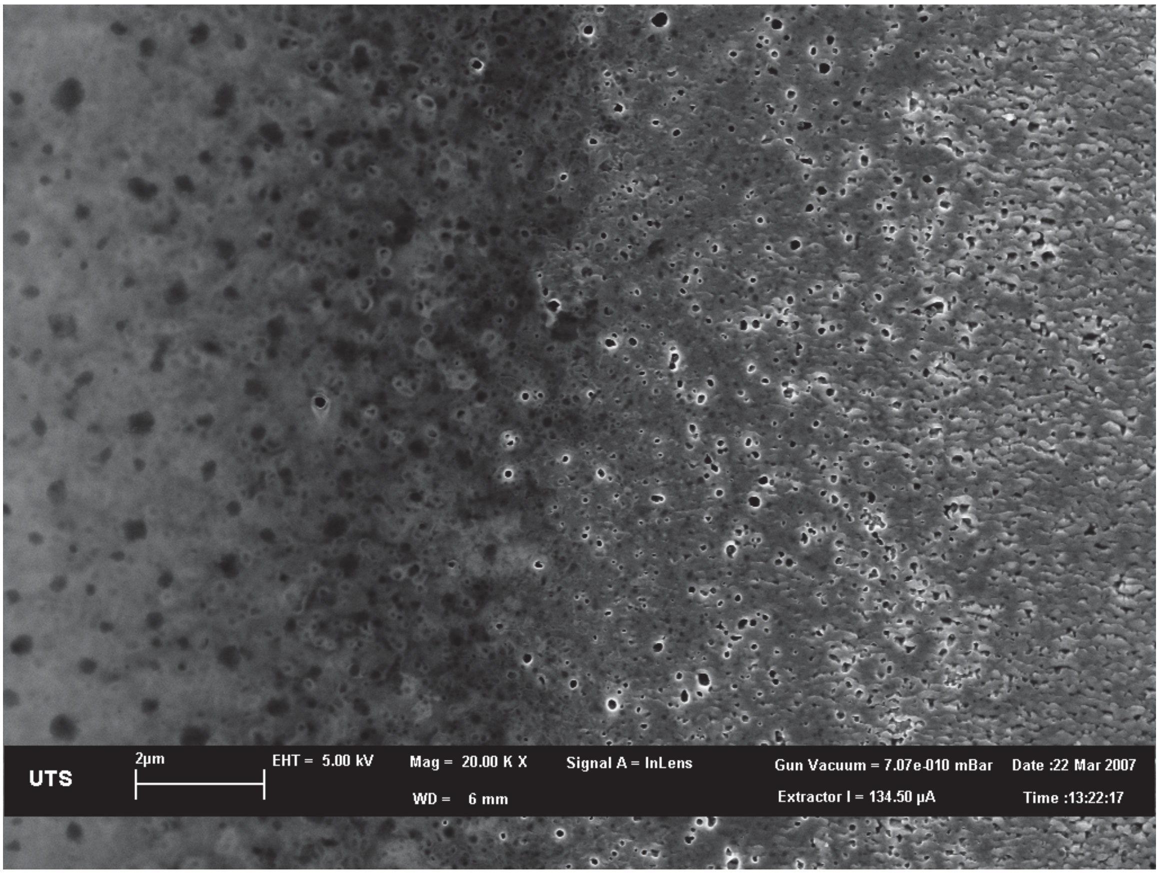

Figure 5.3 *Interface area of SIMS sputtered crater showing the nanoscale porosity generated as the crater was sputtered on anodised Ti6Al4V substrate.*

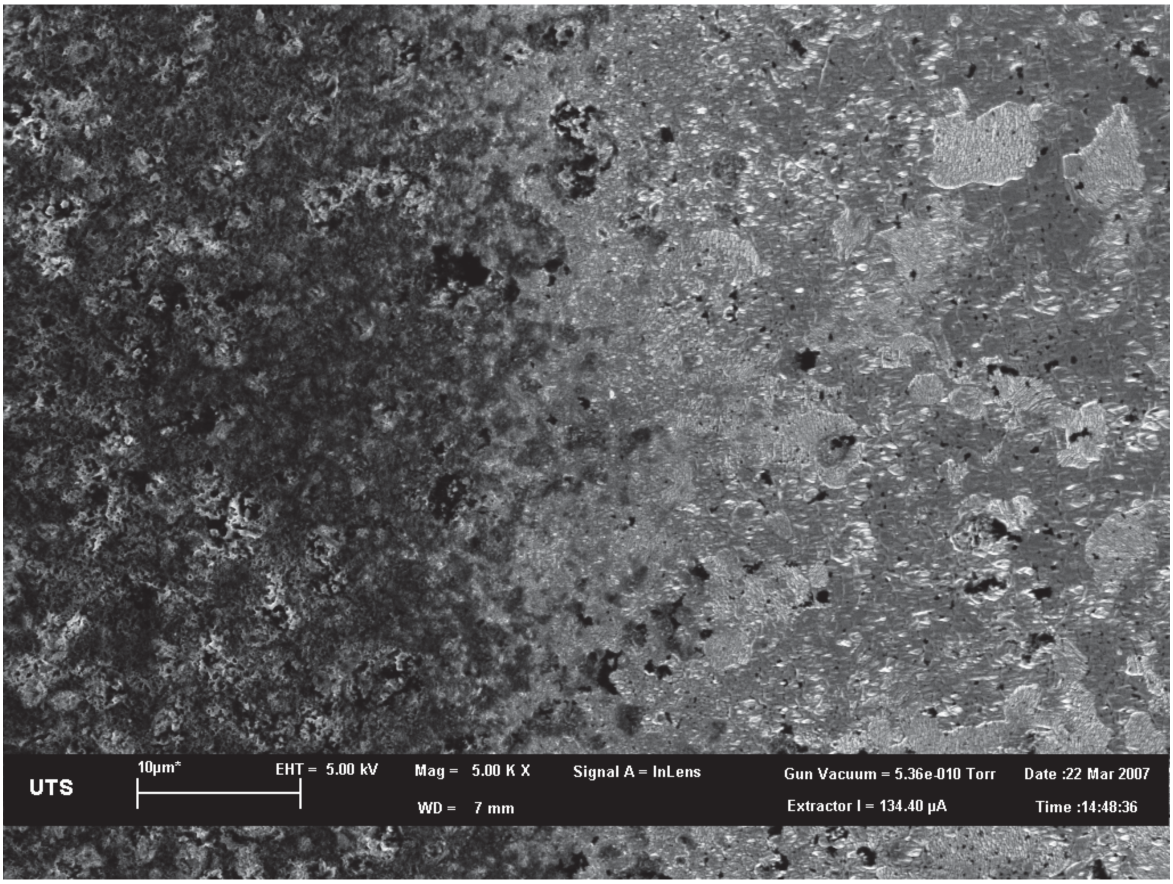

Figure 5.4 *Interface area of 75V Ti6Al4V anodised sample with Zirconia coating*

Figures 5.3 and 5.4 show the interface boundary area on both the anodised and Ti6Al4V samples, the Ti6Al4V sample has a much more clearly defined boundary with a degree of porosity in both the zirconia coating and the interface layer over a 2 - 10 micron scale area. The anodised sample shows a less well-defined boundary region in addition to a significantly smaller degree of porosity in both the coating and interface areas although the zirconia coating does appear to be significantly rougher in appearance which is in part due to the rougher surface of the grown anodic oxide layer formed by anodising at 75V. The result is an increase in the film thickness on the titanium substrate from 5-7 nm to 150 nm for the anodised layer of TiO_2. [80, 81]

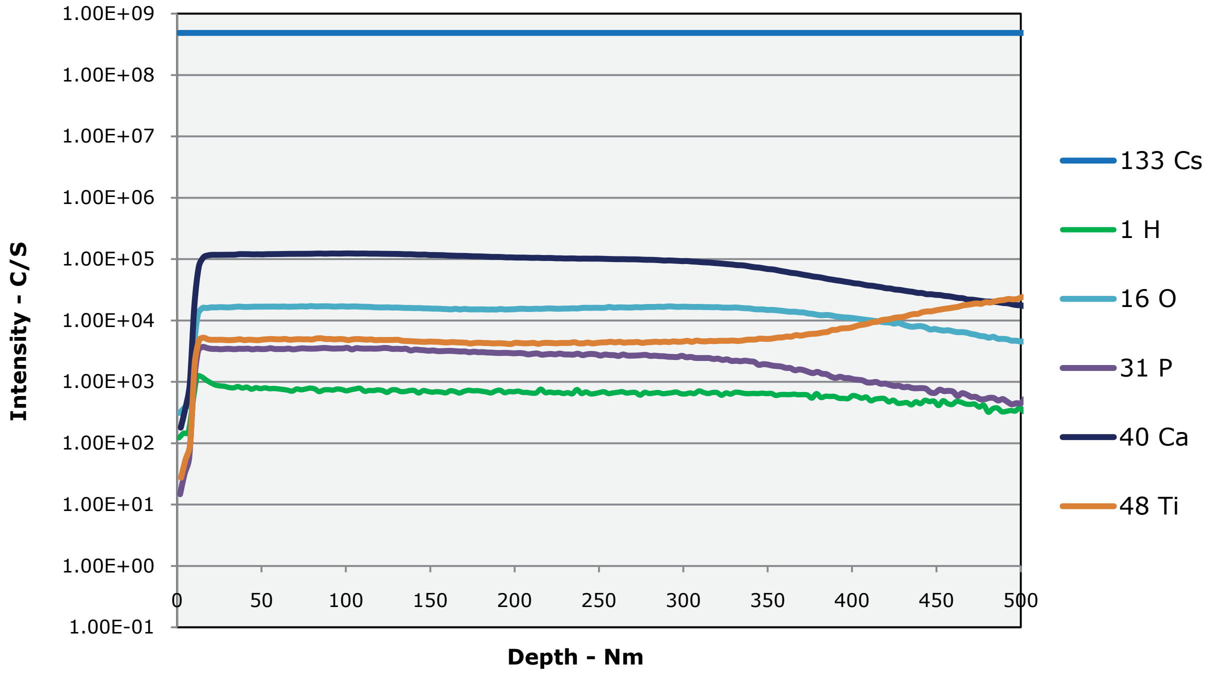

Figure 5.5 *C.P. Titanium SIMS Depth profile of Hydroxyapatite Coating*

Figure 5.5 shows the depth profile of the elements in a hydroxyapatite coating on a C.P. Titanium substrate, the phosphorus and calcium elements give an indication of the intensity or amount of the elemental ions detected at a specific depth. The Titanium ion intensity is consistent up to a depth of approximately 325 nm where it starts to increase in intensity giving an indication that the SIMS sputtering has begun to penetrate the substrate. While the calcium and phosphorus intensity counts start to decrease. Importantly what is shown by this graph is the slow decline in the intensity of the counts indicating that some of the calcium and phosphorus has possibly diffused into the substrate to a small degree with the relatively high spatial accuracy of the SIMS of 5-10 nm this indicated that the detection of the calcium and phosphorus is still occurring at a depth of 450 nm and well inside the spatial resolution of the system.

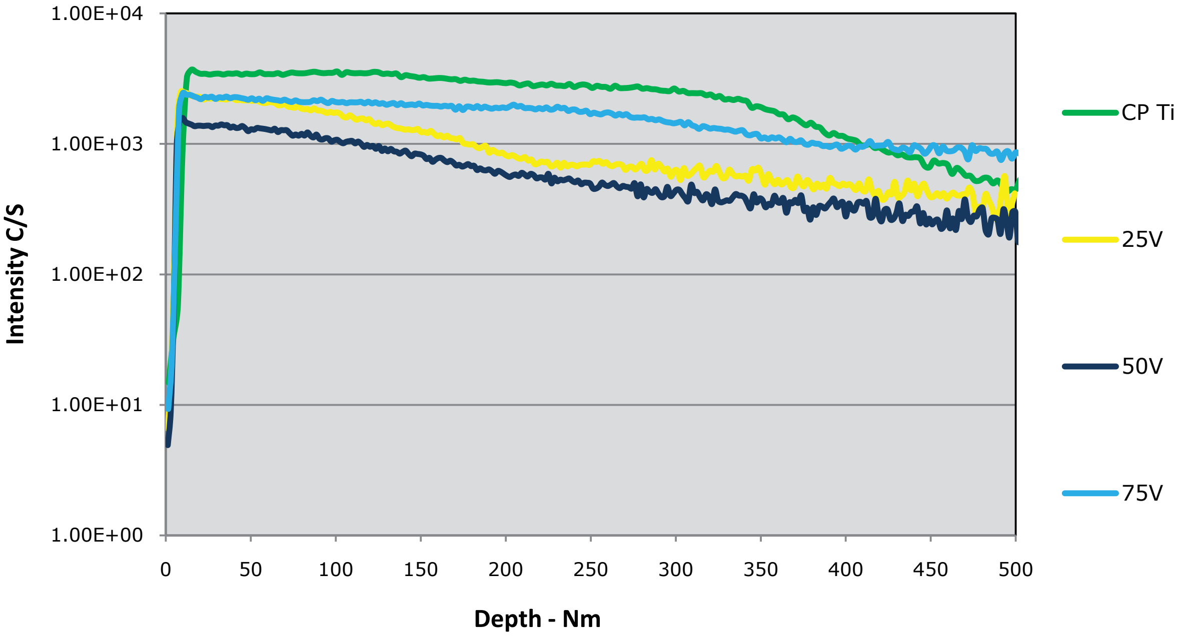

Figure 5.6 *Depth Profile of Phosphorus in C.P. Titanium samples including anodised samples*

The depth profile of phosphorus is shown in figure 5.6 for the C.P. titanium and the anodised 25V, 50V and 75V samples. The C.P. titanium sample has a thicker hydroxyapatite coating of approximately 300 nm whereas the 25V, 50V and 75V have a thinner hydroxyapatite coating of roughly 200 nm. The decrease in intensity of phosphorus again indicates the possibility of some diffusion of the phosphorus into the substrate.

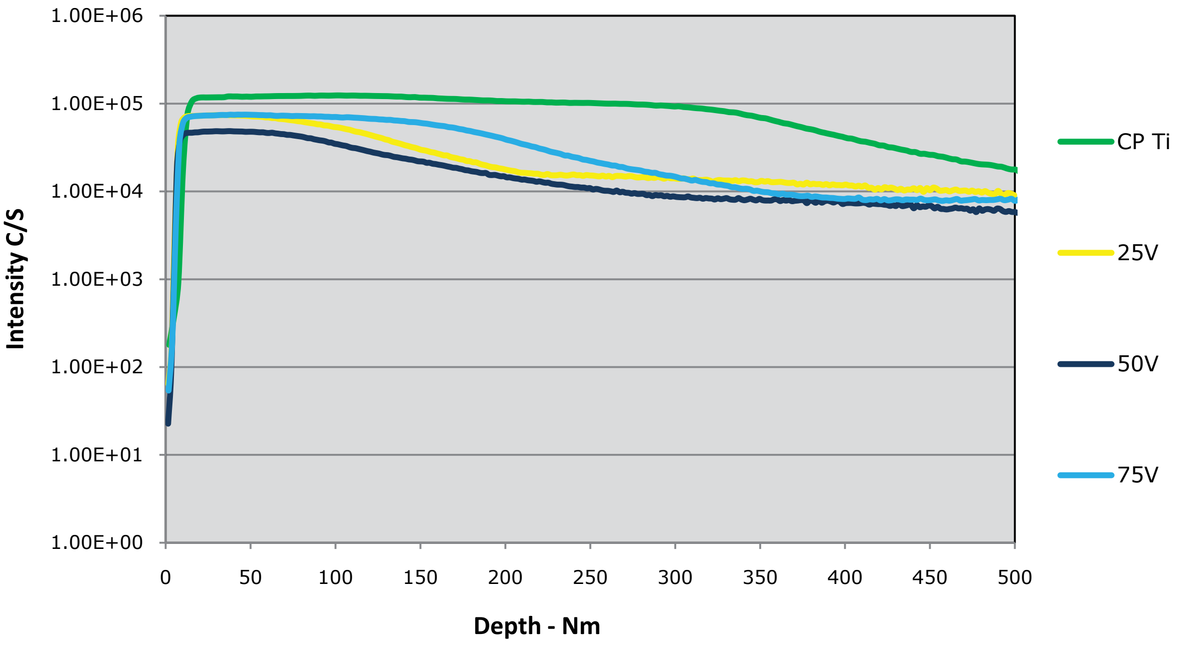

Figure 5.7 *Depth Profile of Calcium in C.P. Titanium samples including anodised samples*

The depth profile of calcium is shown in figure 5.7 for the C.P. titanium and the anodised 25V, 50V and 75V samples. The C.P. titanium sample has a thicker hydroxyapatite coating of approximately 300 nm whereas the 25V, 50V and 75V have a thinner hydroxyapatite coating of roughly 200 nm. The decrease in the intensity of the calcium again indicates some diffusion of the calcium into substrate. The diffusion of the calcium and phosphorus into the substrate in all samples gives an indication of the possibility of diffusion of these elements into the substrate.

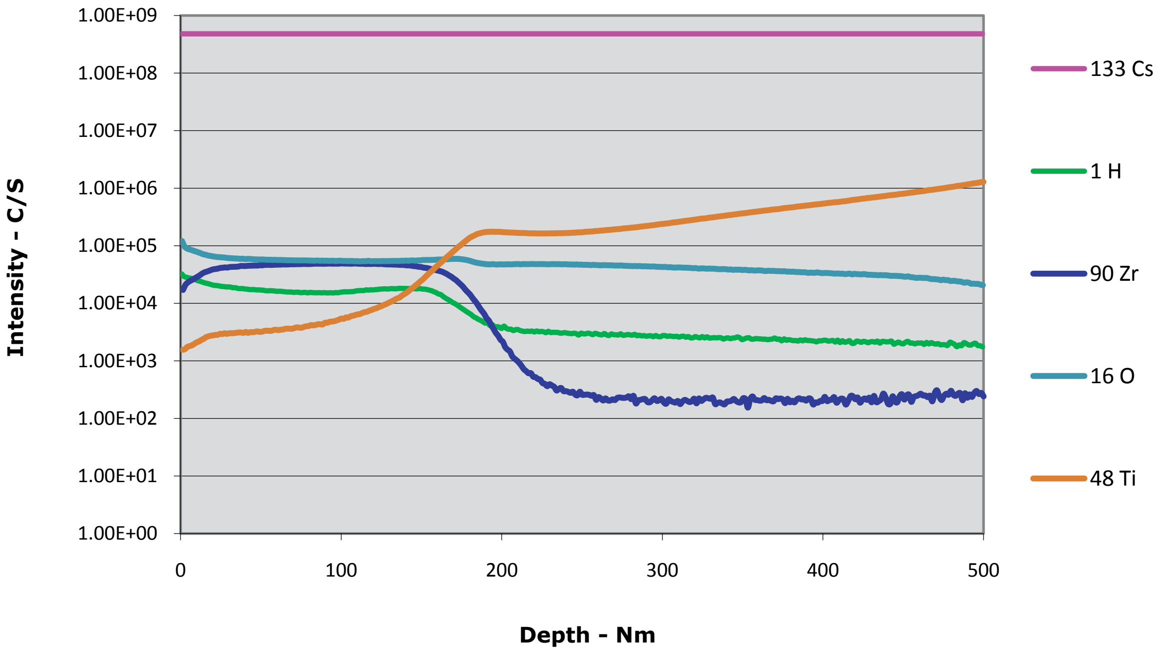

Figure 5.8 *C.P. Titanium SIMS Depth profile of Zirconia Coating.*

Figure 5.8 shows the depth profile of a 150 nm zirconia coated C.P. Titanium with elemental zirconia being detected up to the depth of 225 nm. The titanium ion intensity initially starts to increase at 125 nm with a sharp rise in intensity noted up to about 175 nm in concert with a decrease in the zirconia ion intensity corresponding with the SIMS sputtering penetrating the zirconia coating into the titanium substrate. Again the detection of the zirconium ion at a depth of 225 nm indicates the possibility of some degree of diffusion of the zirconia into the titanium substrate.

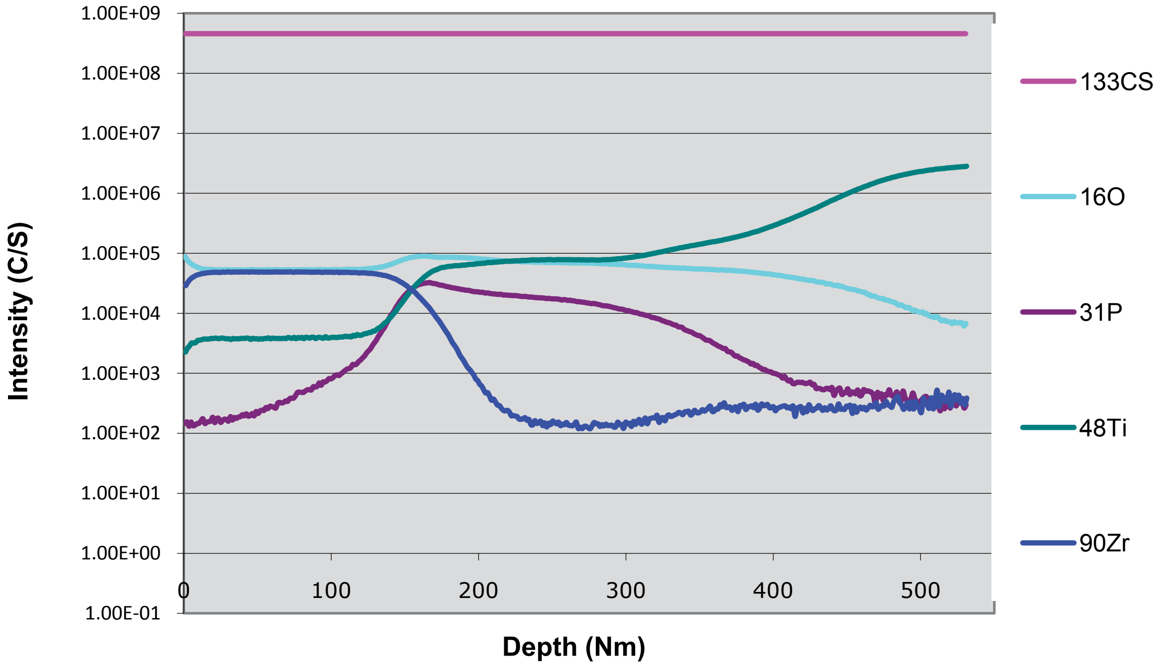

Figure 5.9 *75 Volt anodised C.P. Titanium SIMS Depth profile of Zirconia Coating.*

In figure 5.9 the sample is of a C.P. Titanium substrate that has been anodised at 75 volts. The titanium ion in this case shows two distinct increases in its intensity. The first increase is due to sputtering through the zirconia coating to the anodised titanium oxide layer of a predominate TiO_2 composition as evidenced in previous work [79-81]. The second rise in the titanium ion intensity is when the SIMS sputtering penetrates the anodised layer into the native titanium substrate, the anodised titanium oxide thickness of 150nm is in agreement with previous work showing the growth of the anodic oxide film of 2 nm per volt and 150 nm in total. [79-81]

5.3 SIMS INTERFACE CONCLUSIONS

The sol gel coating of ceramic based coating such as hydroxyapatite and zirconia are often used in variety of fields from biomedical to tribological. One of the main problems with the ceramic to metal bond is that the adhesion can be poor and regardless of the intended use of the coating it is imperative that the adhesion be good between the substrate and the coating.

Vieira, M.T., S. Roque, and A.S. Ramos, [147] have stated that the adhesion depends on the properties of both the substrate and the coating, in addition to the interface that exists between them. The adhesion requires the formation of stable chemical bonds at the interface including van der Waals and the formation of metallic, ionic and covalent bonding configurations. [147]

Viera et al. also states that the decrease in the differing stress arising from the different thermal expansion coefficients of the coating in this case the hydroxyapatite and zirconia sol gel coatings and the metal substrate in our case the titanium substrate. The titanium from grade 2 C.P. titanium to Ti6Al4V coefficient of thermal expansion is 9.1 to 9.8 x 10^{-6} C^{-1} while the thermal expansion coefficient for zirconia is 10.7 x 10^{-6} C^{-1} [148] and hydroxyapatite is 10 x 10^{-6} C^{-1}. [149] The thermal expansion coefficients on the coating and the substrate are very close so the resulting residual stress between them is low. In the case of zirconia sol gel coating and titanium grade 2 substrate a compressive stress of 38 MPa was determined using a finite element analysis (FEA) technique. [150]

Kang, K. J. Yao, N. He, M. Y. and Evans, A. G. [151] argues that for amorphous thin films there are no accurate techniques to calculate the residual stress of thin films having the acceptable precision of the curvature method. As this technique requires the substrate to be accurately thinned to a significant degree to allow measurement of the curvature of the substrate in the case of titanium. Kang et al. [151] has a new method for the in situ calculation of the residual stresses by combining the focused ion beam (FIB) imaging system and a high resolution mapping software system to calculate the residual stresses. [151]

The SIMS of both of the C.P. Titanium and Ti6Al4V and anodised samples are given in appendix 1 and 2. All samples tested demonstrated the possibility of a similar degree of diffusion in the zirconia and the elements of calcium and phosphorus in the case of the hydroxyapatite coating. This diffusion would indicate a good degree of adhesion as the interlayer existing between the ceramic coatings and the titanium substrates has a degree of bonding between the layers and further verification of the diffusion occurring would be possible by using the FIB technique to detect the zirconia ions in the anodised substrates, in addition the phosphorus and calcium ions. It would also be of interest to note if any further diffusion is occurring of other elements.

CHAPTER 6 – XRD ANALYSIS OF THIN FILMS

6.1 TITANIUM X-RAY DIFFRACTION (XRD)

The Zirconia and Hydroxyapatite sol gel coatings were analysed on a Siemens D-5000 Diffractometer, employing CuKα radiation (40kV, 30mA). The diffraction patterns were collected over the 2θ ranges 15-75^{o} using grazing angle incidence and using step time of 1.5 to 4.5 seconds with a step of 0.020 degrees.

6.1.1 XRD ANALYSIS OF TITANIUM SAMPLES

Titanium forms several oxides in differing crystal modifications. In normal conditions, the thermodynamically stable oxide is TiO_2, which exists in three allotropes: rutile, anatase and brookite.

The crystallographic features of anatase and rutile are unique. The anatase structure has a higher degree of tetragonality than the rutile structure, and the anatase structure is less closely packed. The density of rutile is 4.245 g/cm^3 whilst the anatase density is 9% less at 3.893 g/cm^3 [64, 70]. It is the anatase structure that is of interest, and the anodising solutions and processing parameters are designed to increase the anatase structure in the anodic film formed after anodising.

Fujishima and Honda [152] discovered the photocatalytic properties of TiO_2, with the anatase allotrope having the highest photocatalytic properties. The anatase structure formed is discussed in following paragraphs. Liang *et al*. [153] reported that titanium metal can bond to bone directly with alkali and heat treating of the surface of titanium, but that the specific crystalline anatase structure of the titanium surface yielded the most effective surface for bone bonding. In addition to these properties, Tomashov and Strukov [17, 28] postulated that the anodic oxide film formed, produced either amorphous or microcrystalline anatase. While Blondeau *et al*. [44] reported that at low anodising voltages, below 50 volts, the anodised oxide film was quasi-amorphous TiO_2, while the films formed above 50 volts were a TiO_2 anatase phase. Arsov [10], Aladjem [9, 46], Delplancke and Winand [36, 37], and Blondeau *et al*. [43, 67] in later work, argued that the oxide films formed over 50 volts consisted of a microcrystalline anatase structure.

Ohtsuka, T. and T. Otsuki [154], using electrochemical impedance spectroscopy, reported that the anodic film was hydrated titanium oxide and may exist as $TiO_2(H_2O)_{1.4}$ or $TiO_{0.6}(OH)_{2.8}$. Ask *et al*. [68] found that no crystalline areas corresponded with any diffraction patterns with TEM on CP titanium, but that the Ti6Al4V alloy did produce crystalline areas with an anatase crystalline structure for voltages over 50 volts.

6.2 TITANIUM X-RAY DIFFRACTION - EXPERIMENTAL RESULTS

The XRD diffractogram in Figure 6.1 shows an interesting peak reduction at approximately 36° on the two theta scale as the voltage for anodising increases from 25V to 75V on the CP Ti. This indicates that the rutile allotrope is being converted to the anatase allotrope in the anodised oxide film.

The XRD diffractogram in Figure 6.1 shows the reduction of the rutile peak at approximately 38° on the two-theta scale, as it is converted to the anatase micro-crystals, and it is believed that the anodised film formed consists of a mixed oxide film of varying titanium oxides, possibly even including some hydrated forms.

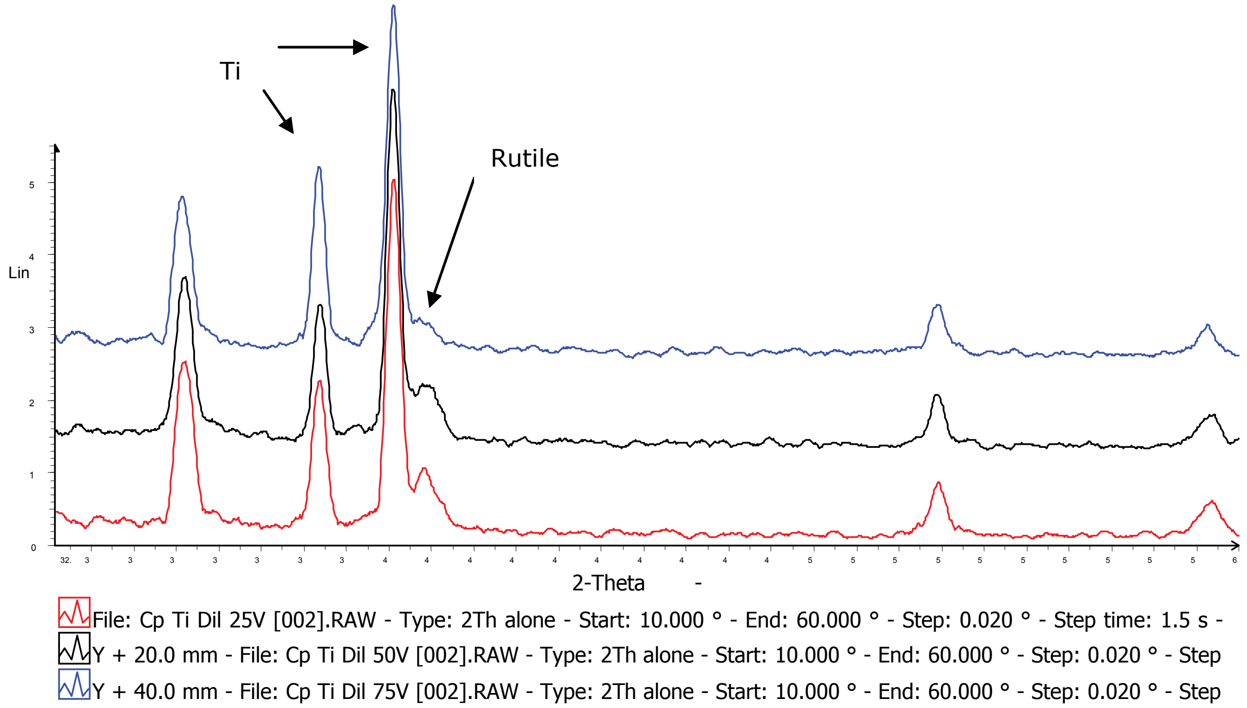

Figure 6.1 *XRD diffractogram of CP titanium anodised samples (25-75V).*

While there is evidence that the amount of the rutile phase is reduced, the XRD patterns show only small peak matches of the anatase structure pattern. This indicates that while there is some evidence of anatase films formed, it was not definitive. . This is in agreement with literature findings [10, 36, 66-68, 155]. Arsov [10, 65] and Blondeau *et al*. [43, 67] argue that the rutile phase is converted to the anatase phase as the voltage is increased.

Delplancke and Winand [36] argue that the oxide film formed with increasing voltage is a mixed oxide consisting of both anatase and rutile phases. Lausmaa *et al*. [58] state that the oxide formed has several different titanium oxides present in the film, including the Ti_2O_5 and Ti_2O_3 oxides, in addition to the rutile and anatase phases.

Similarly, the Ti6Al4V alloy as shown in appendix-3 show rutile peak reductions from the original titanium alloy with increasing anodising voltages at approximately 36° and 55° on the two-theta scale. There are a number of peak matches for the anatase crystalline structure, indicating that the rutile structure is being converted to the anatase structure as the anodising current is increased. The dominate oxides formed are of mixed titanium oxide structures.

6.3 HYDROXYAPATITE SOL GEL COATINGS XRD ANALYSIS

All samples analysed using XRD show the hydroxyapatite phase. Figure 6.2 show the consistent nature of the hydroxyapatite sol-gel coating formed, regardless of the substrate or sol-gel coating pre-treatments used. The only substantial difference in XRD peaks observed on hydroxyapatite-coated samples is shown in Figure 6.2, the 25V anodised sample at approximately 38° on the two-theta scale. This peak in the CP titanium diffractogram shows a double peak, while the 25V anodised sample has a single peak at 38° on the two-theta scale. This peak difference is due to the difference in the substrate, not the hydroxyapatite coating.

There was no sign of calcium oxide or calcium titanate in the XRD samples on any of the original, anodised or C.P Titanium and Ti6Al4V substrates with the diffractograms consistent for all titanium samples.

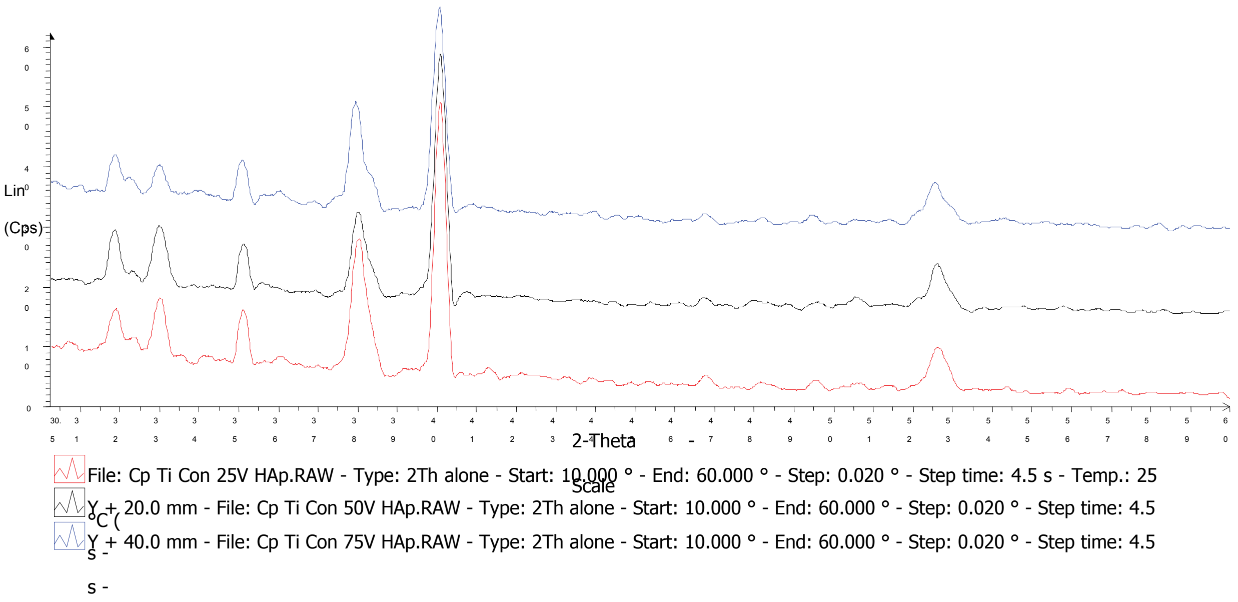

Figure 6.2 *XRD diffractogram of CP titanium – 25V (red), 50V (BLACK), 75V (BLUE) anodised and hydroxyapatite coated*

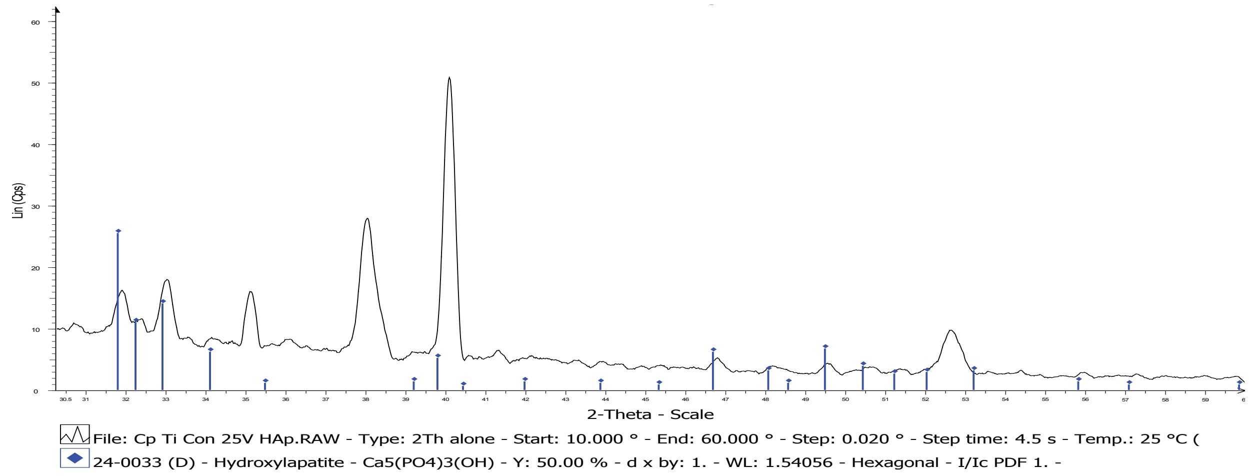

Figure 6.3 *XRD Diffractogram of 25V C.P. Titanium Sample with Hydroxyapatite Coating*

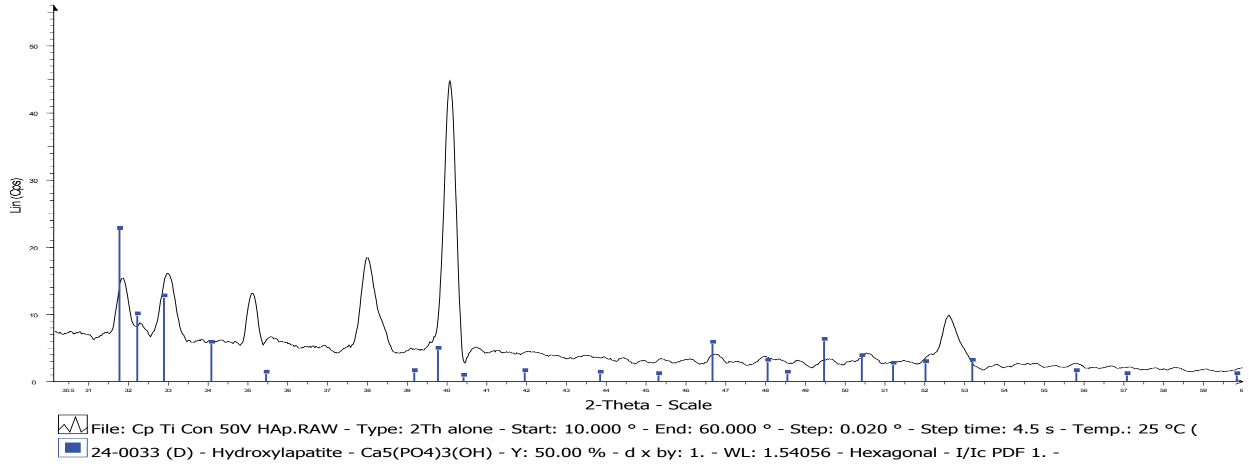

Figure 6.4 *XRD Diffractogram of 50V C.P. Titanium Sample with Hydroxyapatite Coating*

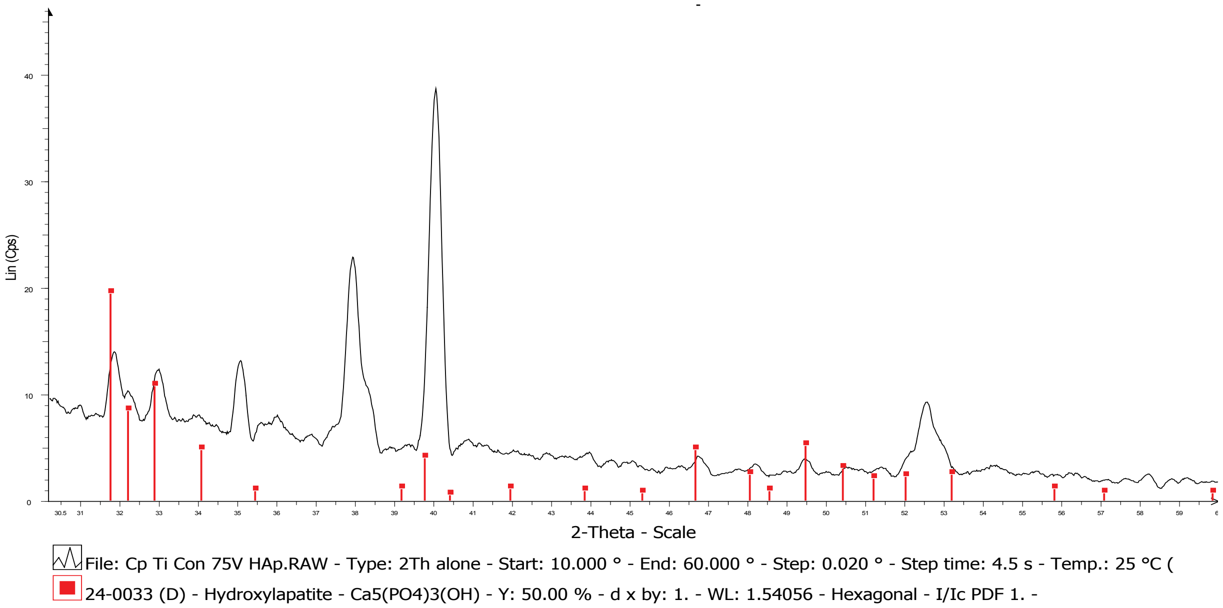

Figure 6.5 *XRD Diffractogram of 75V C.P. Titanium Sample with Hydroxyapatite Coating*

Figures 6.3 to 6.5 show the anodised titanium samples 25V through to 75V with hydroxyapatite coatings with the only differences being the peaks at 35 and 38 on the 2-Theta scale increasing due to the increasing titanium oxide film formed during anodising. All XRD diffractograms have the same hydroxyl apatite pattern indicating the consistent coating of hydroxyapatite on all samples produced.

6.4 ZIRCONIA SOL GEL COATINGS XRD ANALYSIS

All XRD diffractograms show ZrO_2 on titanium samples from the anodised CP titanium samples through to the C.P titanium samples as shown in Figure 6.6. The indicated peaks on the two-theta scale at 38, 35 and 50.5 degrees correspond to ZrO_2 and the titanium substrate at 38 and 40 degrees.

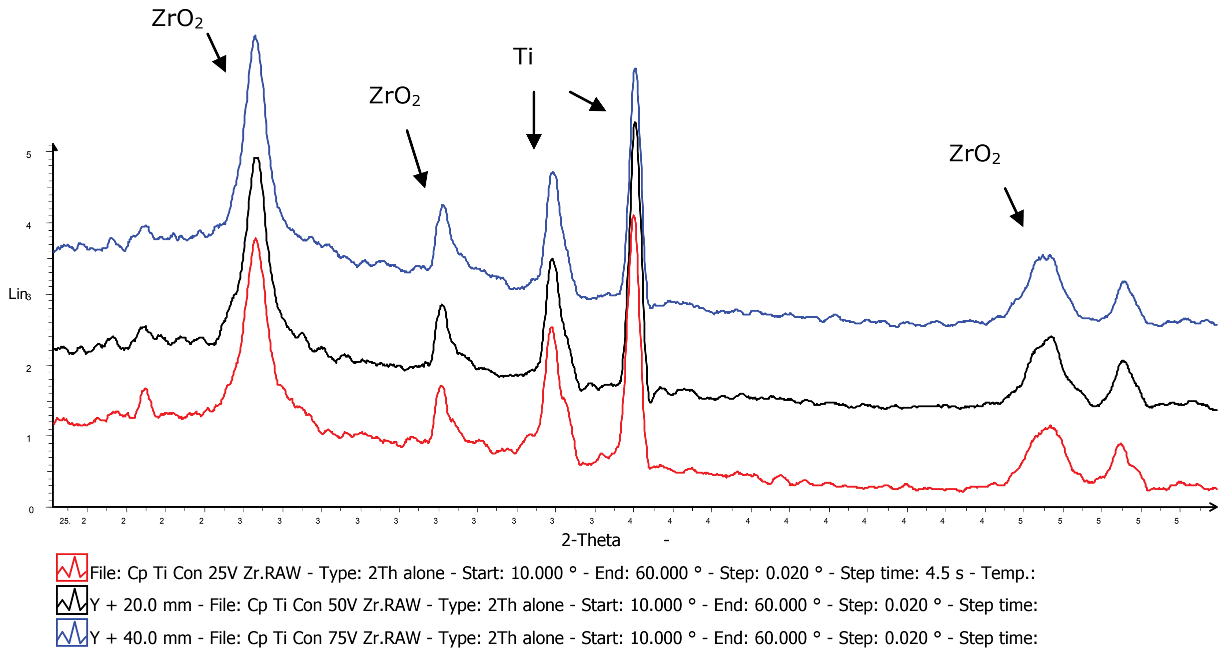

Figure 6.6 *CP titanium diffractogram – 25V (red), 50V (BLACK), 75V (BLUE) anodised – Zirconia-coated samples.*

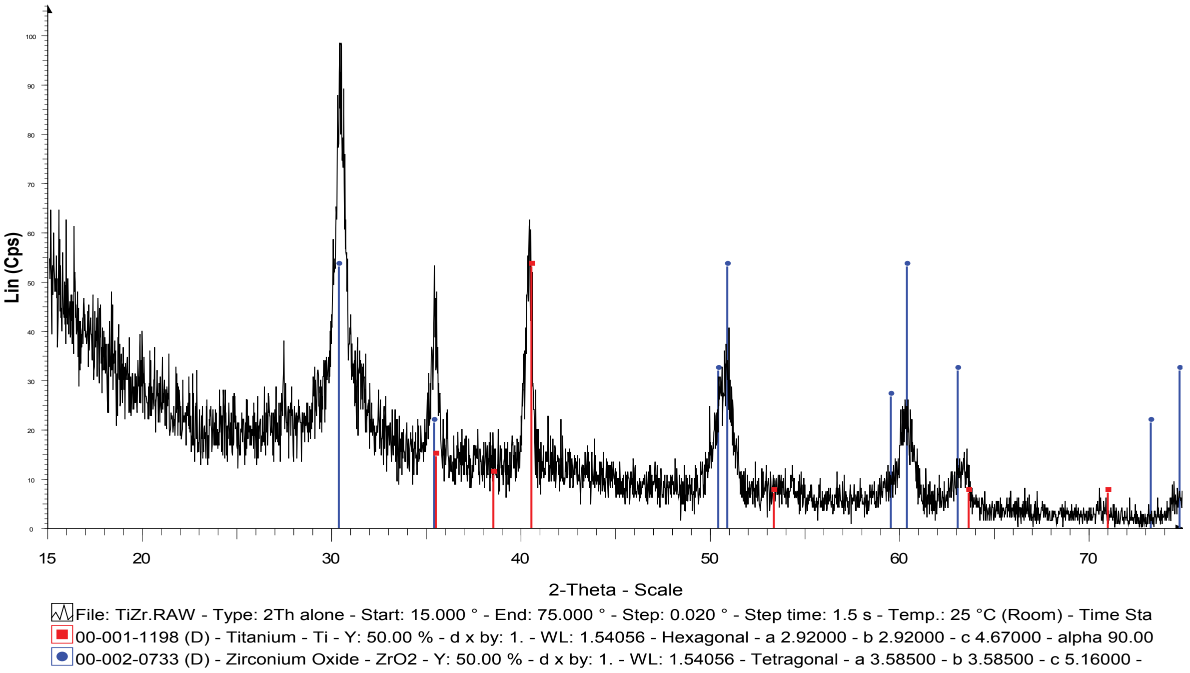

Figure 6.7 *Ti6Al4V Sample with Zirconia Sol gel Coating.*

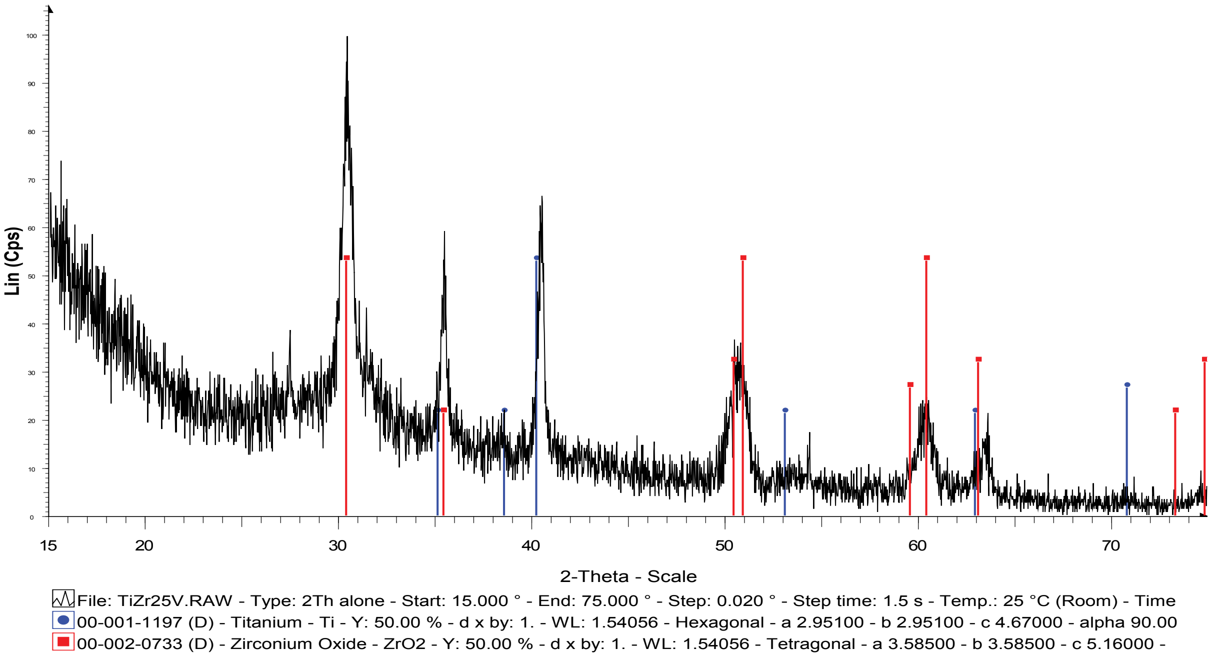

Figure 6.8 *Ti6Al4V anodised at 25V Substrate with Zirconia Sol Gel Coating.*

Figure 6.7 show the Ti6AL4V substrates with Zirconia coatings with figure 6.8 showing the Ti6Al4V Substrate that has been anodised at 25V with zirconia sol gel coating in addition the appendix-4 and appendix-5 samples which show that the zirconia coating produced on all samples is a zirconia coating with the tetragonal polymorph structure.

The crystallization of the metastable tetragonal at the final sintering temperature of 550°C is due to the excess energy in the thin zirconia film as it anneals at this temperature to reduce the residual stresses inherent in the zirconia thin film coating. This is in line with the work of Ehrhart, G. Capoen, B. Robbe, O. Boy, Ph Turrell, S. and Bouazaoui, M. [156] who found a metastable tetragonal phase at an annealing temperature of 450°C. also found that the film undergoes a transformation to the monoclinic phase over a large temperature range of 600-1000°C. [156] In pure zirconia, the tetragonal crystal structure exists when grains are below a critical grain size whereas when they are monoclinic above the critical grain size. Increasing the heat treatment temperature results in particle or grain growth and hence the tetragonal particles transform into the monoclinic form.

Further work is to be undertaken at higher sintering temperatures to see if the tetragonal zirconia formed at the final sintering 550°C changed to the monoclinic form at higher sintering temperatures, although the testing should keep in mind the 883°C temperature in which the titanium will undergo a phase transformation itself to the body centred cubic phase (BCC) or beta (β) phase but in line with Ehrhart, G. *et al.* work it is still possible to work up to the 883°C temperature. [156]

CHAPTER 7 – THIN FILM ADHESION AND SURFACE PROPERTIES

7.1 COATINGS FILM ADHESION

Adhesion is a complex phenomenon related to physical effects and chemical reactions at the interface of the substrate and the coating applied. Adhesive forces occur as the coating is applied to the substrate and during firing or drying. The magnitude of these forces will depend on the nature of the surface and the coating. These forces may be broadly categorised as one of the two types:

1/ Primary Interatomic bonds.

2/ Secondary bonding or Van der Waals bonding [157, 158].

Ionic and covalent bonds are examples of the primary Interatomic forces and provide much higher adhesion values than do the secondary bonds. Secondary bonding is based on much weaker physical forces typified by hydrogen bonds. These forces are more likely to be found in materials having polar groups such as carboxylic acid rather than on non-polar groups such as polyethylene.

The forces holding the two bodies – the coating and the substrate – together may be mechanical interlocking, electrostatic attraction or chemical bonding (diffusion) between coating and the substrate. Depending on the chemistry and physics of both the substrate surface and the coating used, one or a combination of these postulated mechanisms may be involved [157].

7.2 MECHANICAL THEORY

This mechanism of coating action occurs when the substrate surface upon which the coating is spread contains pores, holes, crevices, and voids into which the coating penetrates. The coating has a mechanical keying behaviour. Various surface analytical methods have indicated that the coating can indeed penetrate to complex tunnel-shaped undercuts and cracks which, upon firing or setting, provide mechanical attachment [157].

Adhesions of new coatings to old and weathered coatings as well as adhesion to sand-blasted substrates are examples of this type of adhesion mechanism. Surface roughness affects the interfacial area between the coating and the substrate. Hence, the forces required to remove coatings are related to the geometric surface area, whereas the forces holding the coating on to the substrate are related to the actual interfacial contact area. The stresses and adhesion of a coating can be increased by increasing the surface area [157].

An increase of the surface area can be accomplished by surface roughening via various mechanical abrasion methods. Greater surface roughness is only advantageous if the coating penetrates completely into all irregularities of the surface. Failure to completely penetrate can lead to less coating to interface contact than the corresponding geometric area and will leave voids between the coating and the substrate. Trapped air bubbles in these voids will allow accumulation of moisture and eventually loss in adhesion will result [157].

Although surface roughening generally improves the adhesion, care must be taken to avoid deep and sharp profiles. These types of profiles allow the formation of non-uniform films, which act as stress points that tend to reduce the coating durability by weakening the adhesion [159]. As long as the films are fluid, the shrinkage, uneven depths, and three-dimensional changes introduce little unrelieved stress. As viscosity and film stiffness increase and as film adhesion to the substrate develops, substantial stress are accumulated and retained in the final film.

This theory, however, is not true for every sol-gel film, due to the thin nanoscale nature of some sol-gels, Veronica Borsari, G.G., Milena Fini, Paola Torricelli, Matilde Tschon, Roberto Chiesa, Loris Chiusoli, Armando Salito, Andreas Volpert and Roberto Giardino [160] found that ultra rough coating on biological surfaces provided a good biological response similar to coatings already used in orthopaedics. If the sol-gel layer is sufficiently thin, surface roughening of the substrate will only lead to defects in the sol-gel layer and hence potential sites for failure of the coating. Poulingue, M., M. Ignat, and J. Dijon [161] argue that the stress raising effect exerted by the defects which would control the nucleation and propagation of the cracking process. The size of the defect appeared to be a critical factor for the cracking mechanism.

7.3 CHEMICAL BOND THEORY

Formation of covalent bonds across the interface of the substrate and coating is often possible. This type of bonding is expected to be the strongest and most durable. It does, however, require that there be mutually reactive chemical groups tightly bound to the substrate surface and to the coating. Some surfaces, such as previously coated surfaces, composites and some plastics, contain various chemical functional groups, which, under appropriate conditions, can produce chemical bonds with the substrate material. [159]

7.4 ELECTROSTATIC THEORY

It is possible that electrostatic forces in the form of an electrical double layer are formed at the coating-surface interface. Both coatings and surfaces contain residual electric charges dispersed throughout the system. Interaction between these electric charges can account for some adhesion of the coating. [157, 159]

7.5 DIFFUSION THEORY

When two phases of coating and a substrate attain molecular contact by wetting, atoms will diffuse across the interface to varying extents, depending on material properties and curing conditions. The phenomenon is a two-stage process; wetting is followed by interdiffusion of elements across the interface to establish a chemical bond [157, 159]. In order for the interfacial diffusion to take place the sol gel coating and the titanium oxide film must be thermodynamically compatible with each other.

7.6 MECHANICS OF ADHESION

When two dissimilar materials are brought into intimate contact, a new interface is formed at the expense of the two free surfaces in air. The nature of the interaction at the interface determines the strength of the bond which forms between the coating and the substrate. The extent of these interactions is greatly determined by the wettability of one phase by the other. In the case of coatings that are applied in liquid state, the mobility of the coating phase is also of great assistance [157, 159].

Wetting, therefore, may be viewed as intimate contact between a coating and a substrate. In order for adhesion between the substrate and the coating, in addition to initial wetting, it is important that intimate wetting and bonds remain intact after the coating has been applied. Coatings solidify as a result of cooling to below the glass transition temperature (Tg), or a chemical cross-linking reaction or evaporation of solvents and diluents [157, 159].

7.6.1 WETTABILITY AND SURFACE ENERGETICS

Wetting is a necessary criterion for adhesion. Mechanisms of adhesion previously discussed are operational only if effective wetting is present between the coating and the substrate. The wetting of a surface can be described in thermodynamic terms. The surface tension of the coating in its liquid state and the surface energetics of both the substrate and the solid coating are important parameters which can influence the interfacial bond and adhesion development [157, 159].

7.6.2 INTERFACIAL THERMODYNAMICS

The degree to which a liquid coating wets a solid surface is measured by the contact angle (Ø). When Ø = 0, the liquid spreads freely over the surface and is said to completely wet it. Complete wetting occurs when the molecular attraction between the liquid and the solid molecules is greater than that between similar liquid molecules. The surface tensions are related to the contact angle by an expression from equilibrium considerations.

Whether or not a given coating will wet a solid surface depends on the surface tension of both substances. The ability of a liquid to wet and spread on a solid is often described by the spreading co-efficient, which is related to the surface tension [157].

7.6.3 CONTACT ANGLE

A widely used method of determining the surface tension of a solid involves using contact angle measurements. The calculation of surface free energy from contact angle measurements remains the subject of much controversy because the surface free energy of a solid cannot be measured directly [157, 159]. Approximate and apparent contact angle can be measured using contact angle devices. One measure of the quality of a surface is the critical surface tension. This critical surface tension has been taken as an approximate measure of the surface free energy of the solid.

Surface tension, which is a measurement of surface energy, is the property, due to molecular forces, by which all liquids through contraction of the surface tend to bring the contained volume onto a shape having the least surface area. Generally there is poor surface wettability with low surface energy and a contact angle greater than 90°, and good surface wettability with high surface energy and a contact angle less than 60° [157, 159].

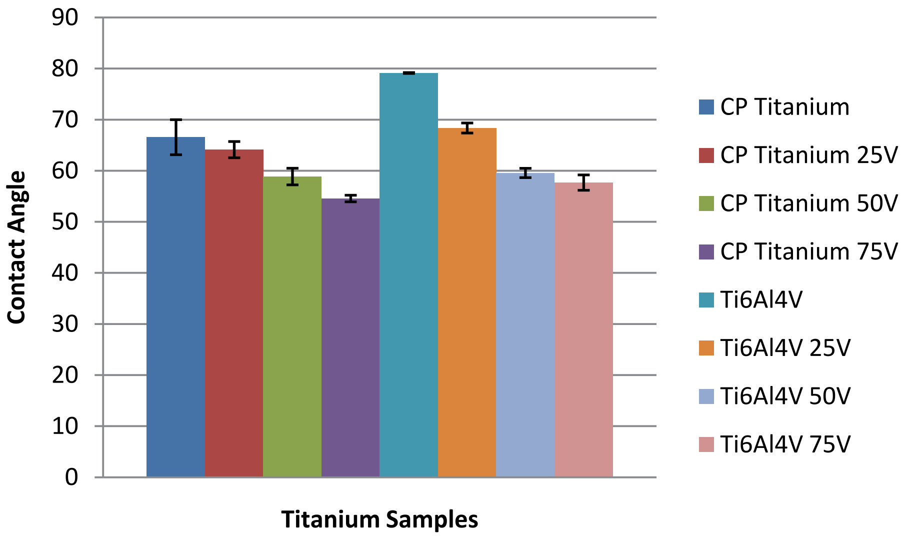

Figure 7.1 *Contact angle of titanium samples*

7.6.4 CONTACT ANGLE DISCUSSION

In table 7.1 and figure 7.1 the contact angle measured for both the C.P. Titanium and Ti6Al4V samples showed a distinct decrease in the contact angle for both the C.P. titanium and Ti6AL4V substrates as the anodising voltage was increased from the original contact values of 66.7° for the C.P. titanium substrate and 79.1° for the Ti6Al4V substrate to 54.6° for the 75 volt anodised C.P. titanium substrate and 57.7° for the75 volt anodised Ti6Al4 substrate.

The decreased contact angles for the anodised substrates leads to increased wettability and a higher surface energy for the substrates [157, 159]. The decrease in the contact angles has led to the significant improvement in the wettability of the anodised samples of both C.P. titanium and Ti6Al4V substrates allowing for the easy application and potentially improved adhesion properties of the hydroxyapatite and zirconia sol gel coatings.

Anodising is an technique which at the same time both grows the oxide film by titanium ions moving through the oxide to react with the oxide ions in solution and form the titanium oxide film and the dissolution of areas of the oxide film with the greatest exposure to the anodising solution. so in fact what is occurring is a levelling out of the titanium oxide film formed, hence the improved contact angles and also lower surface roughness figures. This process though is a balancing act though as rapid film formation through high voltages and short anodising times will produce rough porous oxide films and controlled low voltages over a longer time period will result in a more homogeneous smoother surface oxide film formed.

Contact Angle Measurements on Varying Titanium Substrates

Sample	**Theta - R**	**Theta - L**	**Theta (mean)**	**Fit Error**	**Average**	**Standard Deviation**
CP Titanium	66.4 63.3 73.3	64.7 64.3 67.5	65.5 63.8 70.4	2.66 4.8 3.41	66.57	3.43
CP Titanium 25V	65.2 61.8 64.5	64.8 62.8 65.7	65 62.3 65.1	3.42 5.23 5.89	64.13	1.59
CP Titanium 50V	60.6 61.6 56.8	57.9 59 57.4	59.2 60.3 57.1	4.73 2.46 4.96	58.87	1.63
CP Titanium 75V	55.3 55.5 54.7	52.9 55.2 54.2	54.1 55.3 54.3	3.98 2.69 2.59	54.57	0.64
Ti6Al4V	77.0 79.9 78.4	78.2 81.4 79.7	77.6 80.7 79.1	7.48 7.62 7.47	79.13	0.08
Ti6Al4V 25V	67.7 69.3 67.7	67.9 69.5 67.8	67.8 69.5 67.8	4.68 4.98 4.71	68.37	0.98
Ti6Al4V 50V	59.7 61.2 59.8	59.1 59.9 57.7	59.4 60.55 58.75	3.86 3.67 4.91	59.57	0.91
Ti6Al4V 75V	59.3 59.4 57.4	57.6 57.8 54.5	58.5 58.6 55.95	3.3 2.15 2.43	57.68	1.50

Table 7.1 *Contact Angle measured using drop shape analysis with 15μL drop*

7.7 SCANNING ELECTRON MICROSCOPY (SEM)

A Zeiss Supra 55 VP (variable pressure) scanning electron microscope was used to investigate the morphology of the coated samples. These types of field emission gun (FEG) microscopes can operate in conventional high vacuum mode, but can also be operated in low vacuum mode, thus allow imaging of electrically insulating materials in pristine condition. The samples were imaged using voltages (between 5 kV and 10kV) using the new in-lens secondary electron detector, which provides high signal/noise images.

7.8 SURFACE ROUGHNESS

All the samples were measured with a KLA Tencor Alpha-step IQ surface profiler at ANSTO's Materials Engineering division. Samples were measured using a stylus profilometer (Alpha-Step IQ, Tencor) for three different regions on each sample surface. A scan length of 2 mm was used and the raw data were filtered to enable surface roughness values to be obtained.

The contact angle of pure distilled water drops on the surface of the anodised and titanium substrates was examined using an in-house built device. A drop of water 15 µL in volume was deposited on the sample surface from a pipette positioned directly above.

A camera was situated at 90° to the sample and focussed on the droplet and used to capture images to a Macintosh computer and then to an image analysis program (Scion Image, National Institute of Health, USA) was used to calculate the contact angle from the drop shape. Several samples were used in each instance and the averages obtained for at least 5 droplets per sample tested. [162]

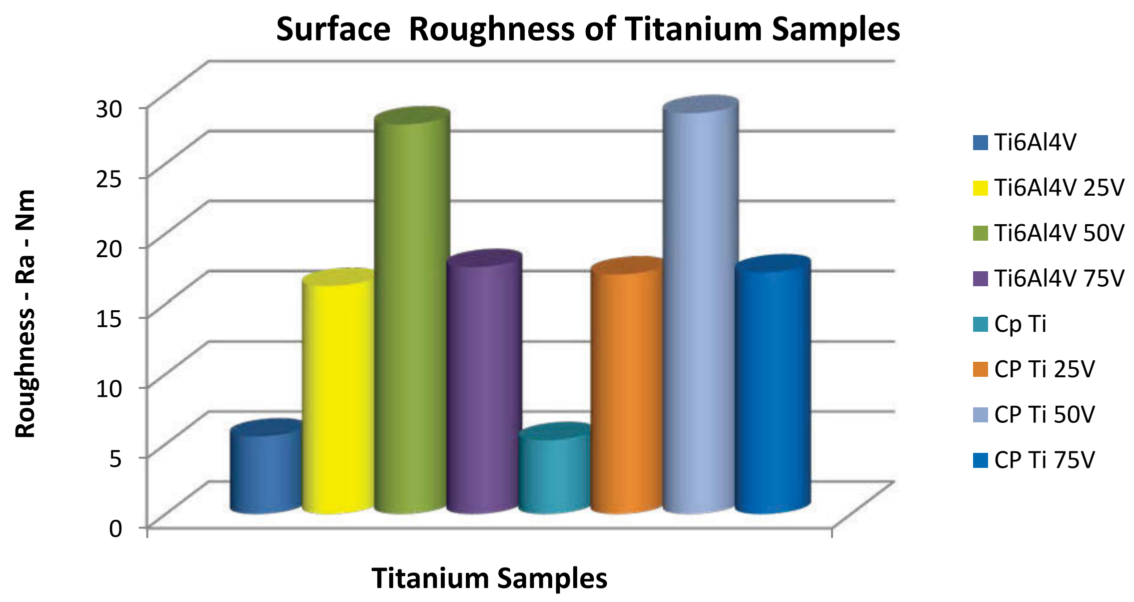

Figure 7.2 *Surface Roughness of Titanium Samples measured using KLA Tencor Alpha-Step IQ Surface Profiler.*

7.8.1 SURFACE ROUGHNESS DISCUSSION

The tables 7.2 and 7.3 give a surface roughness figure for all anodised and coated samples showing the roughness both before and after coating and fired with the hydroxyapatite and zirconia sol gel coatings. The distinct increase of the surface roughness after anodising is shown graphically in figure 7.2 with the 50V samples having the greatest surface roughness measurements on both C.P. titanium and Ti6Al4V samples this is in part due to the actual combined growth method used to anodise the samples with the 50 volt samples having the highest current applied and thus the roughest surfaces the 75 volt surfaces even though having a higher potential were slowly brought up to this voltage and the resulting current was reduced by the time it formed the same oxide thickness of the 50 volt samples and the increasing voltage slowly increased as the voltage was increased due to the limited current carrying ability of the rectifier used.

Surface Roughness of Anodised Titanium Substrates

Anodised Samples CP Titanium					**Average-(µm)**	**Nm**
Surface Roughness -(µm)						
Sample						
CP	0.0053	0.0055	0.0052	0.0065	0.00554	5.54
25V	0.01746	0.01639	0.0155	0.0166	0.01624	16.24
50V	0.0338	0.0237	0.0255	0.0288	0.0278	27.8
75V	0.0182	0.0202	0.0201	0.0145	0.0176	17.6

Anodised Samples - Ti6Al46V alloy					**Average-(µm)**	**Nm**
Surface Roughness -(µm)						
Sample						
Alloy	0.0052	0.0054	0.0054	0.0055	0.00528	5.28
25V	0.01744	0.01625	0.0166	0.0172	0.0170	17.07
50V	0.0355	0.0258	0.0255	0.0288	0.0286	28.6
75V	0.0178	0.0191	0.0177	0.0166	0.01722	17.22

Table 7.2 *Surface Roughness of Titanium Samples measured using KLA Tencor Alpha-Step IQ Surface Profiler*

Surface Roughness of Sol Gel Coated Titanium Samples

	CT Titanium Samples -(µm)					
					Average	**Nm**
CP Ti HAp	A	0.0062	0.0064	0.0052	0.0059	5.93
25V HAp	B	0.0062	0.0056	0.0072	0.0063	6.33
50V HAp	C	0.0062	0.0165	0.0145	0.0124	12.4
75V HAp	D	0.0092	0.0101	0.0126	0.0106	10.63
CP Ti ZrO2	E	0.0062	0.0126	0.0181	0.0123	12.3
25V ZrO2	F	0.0062	0.0232	0.0108	0.0134	13.4
50V ZrO2	G	0.0062	0.012	0.0156	0.0112	11.26
75V ZrO2	H	0.0062	0.0222	0.0234	0.0172	17.26
	Ti6Al4V Alloy					
					Average	**Nm**
Ti6Al4V HAp	I	0.0315	0.0181	0.0129	0.0208	20.83
25V HAp	J	0.0067	0.0294	0.0108	0.0156	15.63
50V HAp	K	0.0272	0.0208	0.0343	0.0274	27.43
75V HAp	L	0.0148	0.0118	0.0171	0.0145	14.56
Ti6Al4V ZrO2	M	0.0153	0.0161	0.0185	0.0166	16.63
25V ZrO2	N	0.0185	0.0147	0.0175	0.0169	16.9
50V ZrO2	O	0.0191	0.0193	0.0182	0.0188	18.86
75V ZrO2	P	0.0176	0.0091	0.0185	0.0150	15.06

Table 7.3 *Surface Roughness of Sol Gel Coated Titanium Samples measured using KLA Tencor Alpha-Step IQ Surface Profiler.*

CHAPTER 8 – MECHANICAL MICRO ADHESION AND NANO HARDNESS TESTING

8.1 MECHANICAL SAMPLE PREPARATION

All titanium samples used in the experiments were prepared on a Struers Rotoforce-4 Auto polisher, the surfaces of samples for microstructure characterization and nano-indentation testing were ground on successively finer grades of polishing surfaces, using successively finer grades of diamond paste and finally polished with a colloidal silica suspension with 5% H_2O_2 solution. Following washing and drying, the samples were stored under laboratory conditions (room temperature, 40% relative humidity). The polishing methods are further outlined in Tables 8.1 and 8.2.

All samples used in this thesis had the same polishing preparation before anodising and sol gel coatings were carried out on the polished surfaces so that they all had the same initial surface finish, and any differences would be down to what processes had been carried out on the sample tested.

Polishing Techniques and Materials

Polishing Surface	Grit/Grain	RPM	Force	Time(Min)	Lubrication
MD- Piano	220	150	15N	6	Water
MD- Largo	15µm	150	15N	4	15µm diamond Suspension
MD- Largo	6 µm	150	15N	4	6µm diamond Suspension
Neoprene	OP-S*	150	10N	4	Colloidal silica suspension with 5% H_2O_2

Table 8.1 *Ti6AL4V Sample polishing method using STRUERS Autopolisher*

Polishing Surface	Grit/Grain	RPM	Force	Time(Min)	Lubrication
MD- Piano	220	150	15N	6	Water
MD- Largo	15µm	150	15N	4	15µm diamond Suspension
MD- Largo	6 µm	150	10N	6	6µm diamond Suspension
Neoprene	OP-S*	150	10N	4	Colloidal silica suspension with 5% H_2O_2

Table 8.2 *C.P Titanium Sample polishing method using STRUERS Autopolisher*

8.2 ADHESION TEST METHODS

The multitude of test methods for coating adhesion includes more popular approaches involving tensile "pull-off" or scratch testing [122, 163-166]. However, few of these methods are directly applicable to thin film systems, specifically nano-coatings.

In test situations such as scratch testing, where the test specimen design does not necessarily preclude the testing of thin films [122], complex stress states make analysis of the interface properties extremely difficult [122]. Solutions to the tensile and shear stress distributions at the substrate surface and interface respectively can be mathematically difficult [122, 167].

A common and relatively simple experimental method for studying the crack evolution and mechanical properties of brittle thin films on ductile substrates consists of straining the system in uniaxial tension. A network of transverse cracks develops in the brittle film, while possible adhesion failure may occur at the interface [168]. The extent of the damage as the test proceeds can be related to the following mechanical properties of the system: Young's Moduli of the film and substrate, fracture toughness of the film, the interfacial strength and residual stresses in the film [122, 168, 169].

8.3 MICRO-ADHESION TESTING OF THIN FILMS

The mechanics of cracking and loss of adhesion occurring in uniaxially stretched film/substrate systems are numerous. The cracking and decohesion of thin films has been investigated by Hu and Evans, for brittle chromium films on ductile aluminium and stainless steel substrates [168, 170].

The work of Hu and Evans in analysing the brittle chromium films on ductile substrates [170], enabled the micro-adhesion uniaxial testing system to evaluate a critical non-dimensional parameter of the decohesion process - Ω_c, where

$$\Omega_c = k_c / \sigma . \sqrt{h} \qquad (8.1)$$

with k_c being the material fracture resistance along the fracture path (interface, substrate, film) [170], σ is the total tension in the film (residual + applied) and h is the film thickness. The quantity, Ω_c, depends upon the ratio of the Young's Modulus of the film, E_f, to that of the substrate, E_s, as well as the ratio of the film thickness to the substrate thickness, h.

Typically, the film is adherent and decohesion occurs by growth of the cracks in the substrate parallel to the interface and k_c becomes the substrate toughness, k_c^s [170-172]. When the substrate is ductile, the cracked film can either remain attached to the substrate or delaminate along the interface, depending upon the film adhesion and substrate yield strength [170-172].

8.4 MECHANICAL PROPERTIES

From a load-displacement curve obtained from the micro-adhesion test it is possible to then calculate stress versus strain curve.

Stress = $\sigma = P / A = P / w.t$ (8.2)

Strain = $\varepsilon = \Delta L / L_o$ (8.3)

P = force measured in N during experiment

A = Area = width of sample x thickness of sample

ΔL = Displacement

L_o = Gauge length

w = width

t = thickness

Analysis of film cracking behaviour observed using optical microscopy from the micro-adhesion testing and using the data from the stress/strain curve allows for the calculation of the strain at the first point of cracking in the film, and strain at the initial point of debonding, if seen. The fracture strength and fracture toughness of the zirconia and hydroxyapatite nano coatings on the titanium substrates were investigated using micro adhesion tensile tests, the tests were conducted using a small in-house built mechanical tester equipped with a 2500 N capacity load cell.

The samples were fixed in place on the device and pulled at a rate of 3 μm/s with the mechanical testing device positioned directly under the objective lens of an optical microscope (Zeiss, Axioplan) at a fixed magnification of 500×.

Load and displacement were recorded every second along with corresponding images of the coated surfaces using an analogue camera. The combination of the images captured and the stress–strain data calculated from the experimental measurement of the load and displacement are the key to the calculation of the mechanical properties. The testing was based on previous work by Latella and Ignat. [169, 173, 174]

8.4.1 CRITICAL STRESS FOR CRACKING

$$\sigma_c = \varepsilon_c . E_f + \sigma_r \qquad (8.4)$$

σ_c = Critical stress for cracking

ε_c = Strain at first cracking in film

E_f = Young's modulus of film

σ_r = Residual stress

8.4.2 FRACTURE ENERGY OF FILM

$$\lambda_f = \sigma_c^{\,2} . t / E_f \; [\pi . g(\alpha) + \sigma_c / 3\tau] \qquad (8.5)$$

λ_f = fracture energy of film (Jm^{-2})

σ_c = critical stress for cracking

t = thickness of film

E_f = Young's modulus of film

A = Dundas parameters = $E_f - E_s / E_f + E_s$

g(ɑ) = constant from tables in Hu and Evans [170]

τ = $\sigma_y / \sqrt{3}$ = σ_y = yield stress (from exp.)

8.4.3 FRACTURE FILM TOUGHNESS

$$K_{IC} = (\lambda_f . E_f)^{1/2} \qquad (8.6)$$

K_{IC} = film toughness

λ_f = fracture energy of film (Jm^{-2})

E_f = Young's modulus of film

All equations are taken from work of Hu and Evans, Ignat, Beuth and Klingbeil [169, 170, 175, 176].

8.5 DOG-BONE SAMPLES USED IN MICRO-ADHESION TESTING

The dog bone samples for the micro-adhesion tester were made from 1 mm thick CP titanium plate (Titanium International), and were wire cut to the specified dimensions. These samples were polished using the same technique and with the same sample holders before anodising and sol gel coating as the original titanium samples used in the XRD and SEM work had been. Each sample was individually packed in a separate container to ensure no possibility of damage to the coating.

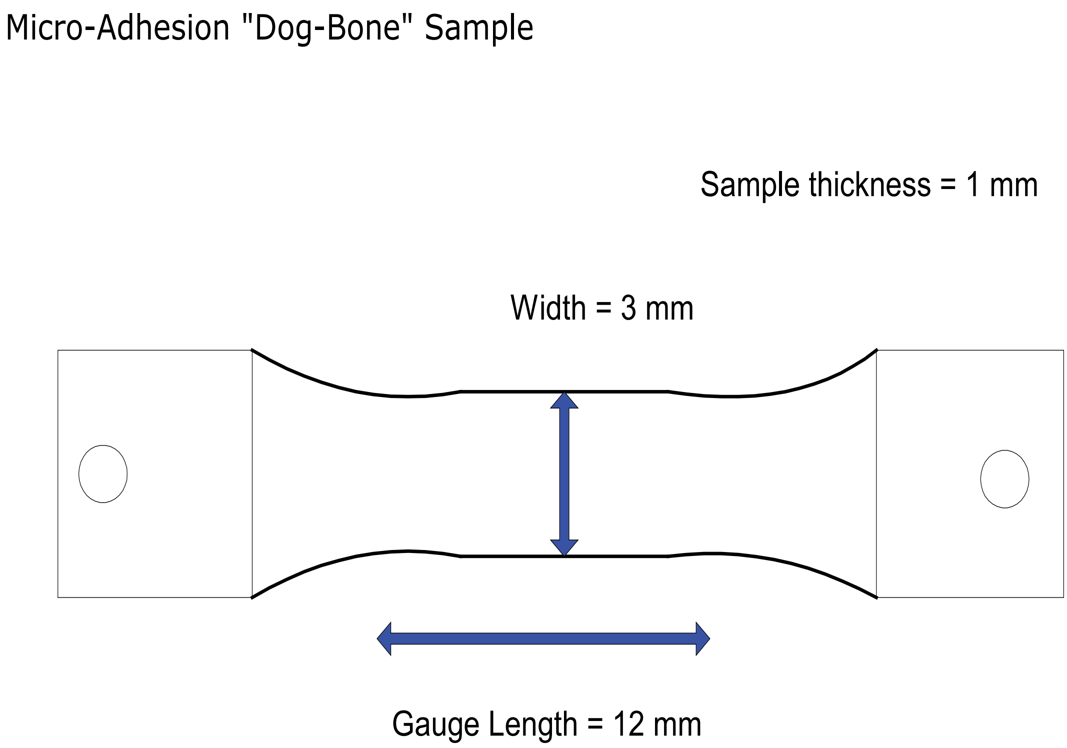

Figure 8.1 *Micro-adhesion test sample.*

8.5.1 Micro-Adhesion Testing Method

The flat, "dog-bone-shaped" titanium samples (figure 8.1) were anodised and coated as indicated in previous chapters, and were tested in tension at a rate of 0.005 mm/s using a specially designed high-stiffness small mechanical testing device positioned directly under the objective lens of an optical microscope (Zeiss Axioplan) at a fixed magnification of 200x (Figure 8.3). The device is shown in Figure 8.2.

The set-up described above allowed the direct observation and recording of crack initiation and evolution, and debonding of the thin films on the titanium specimens. The applied load and the imposed displacement were recorded during the tests (every 2 seconds). Simultaneously, optical images of the coated surface were captured every 2 seconds using a MTI analogue camera with image analysis software (Scion Image, NIH); the complete micro-adhesion set-up is shown in Figure 8.3. After testing, the samples were imaged using a LEO SUPRA 55VP SEM.

The adhesion testing allowed for the calculation of the stress and strain at the initial cracking and initial debonding points, which were recorded during the tests. Using the equations from the works of Hu and Evans, Ignat, Beuth and Klingbeil [169, 170, 175, 176], this allowed for the calculation of the fracture toughness and interfacial fracture energy of the film.

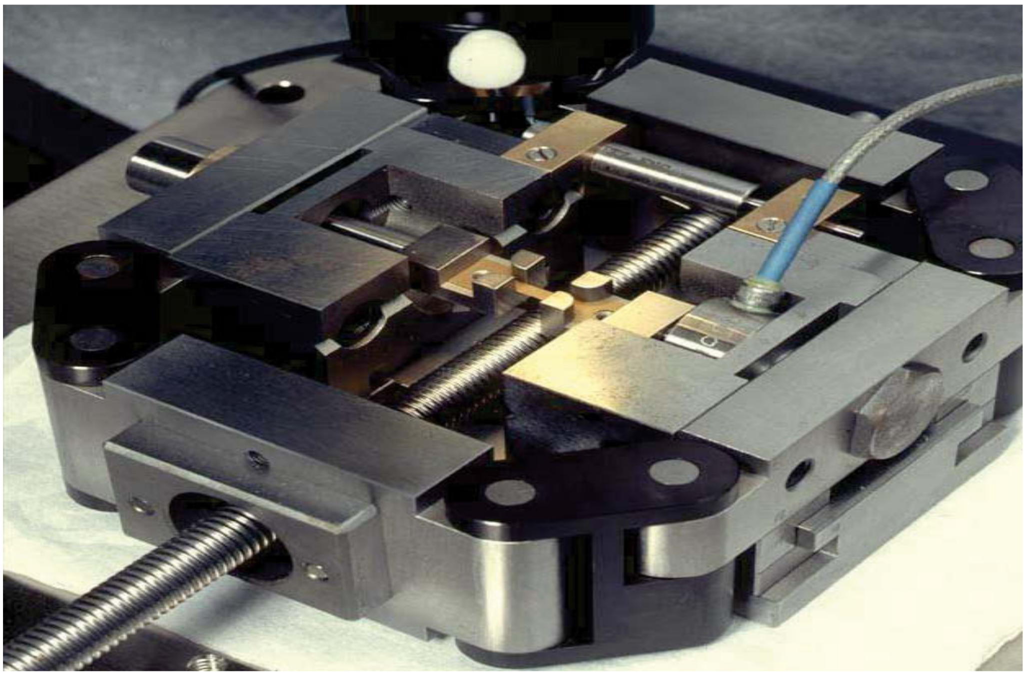

Figure 8.2 *Micro-Adhesion Tester*

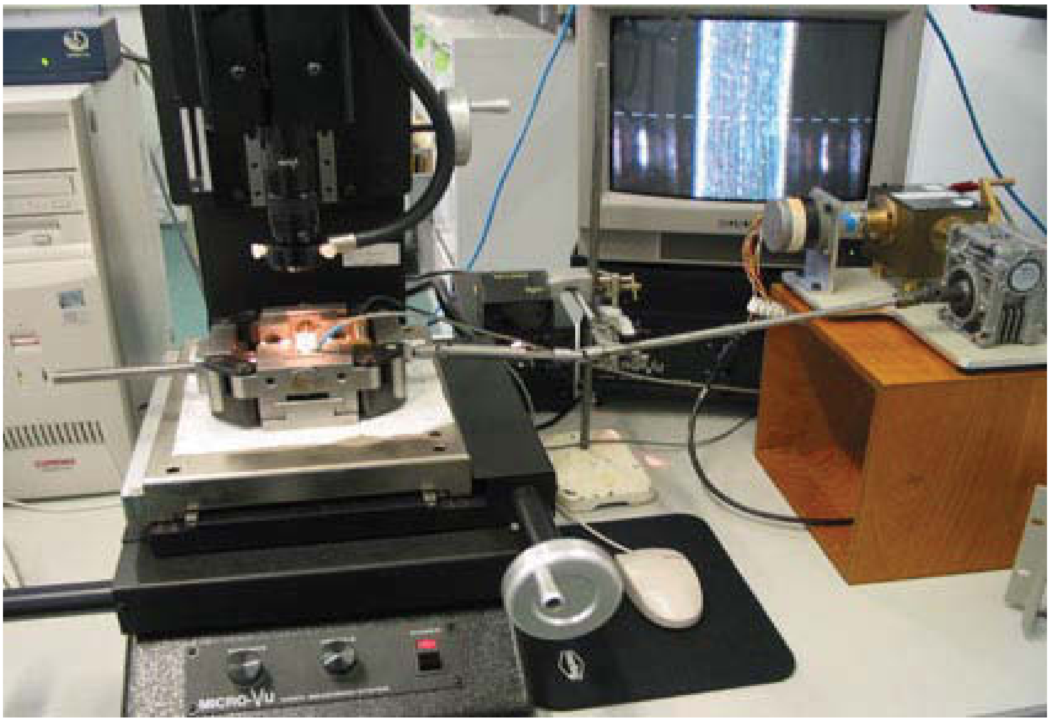

Figure 8.3 *Micro-adhesion test set-up showing the video attachment, monitor and measuring devices.*

8.6 MICRO-ADHESION TESTING RESULTS

The micro-adhesion testing is a good technique for gathering a wide range of interface, thin film and substrate combinations allowing for the quantitative measurement of the systems to give an overview of the thin film systems. There is a substantial theoretical and experimental load of work relating to brittle films on ductile substrates form the work of Hu and Evans [170], Thouless [172, 177] and Ignat [169, 175].

Bordet *et al.* [178] investigated the interfacial roughness effect and the modification of the physical or chemical parameters used in the thin film system preparation for coatings of the thin film on the substrate. The micro-adhesion testing systems allows for the thin films systems adhesion properties to be quantified such as the interface energy of the thin film system and the shear stress of the system.

8.6.1 MICRO-ADHESION DISCUSSION

Interface energy calculations for the zirconia thin films were firstly conducted on the cracked zirconia coatings derived from the original zirconia sol gel solution, which yielded a thin film thickness of 200 nm thus exceeding the critical cracking thickness of the zirconia sol gel thin films [129, 130]. Measurements were the performed using the modified zirconia solution that yielded 100 nm films, which showed no cracking.

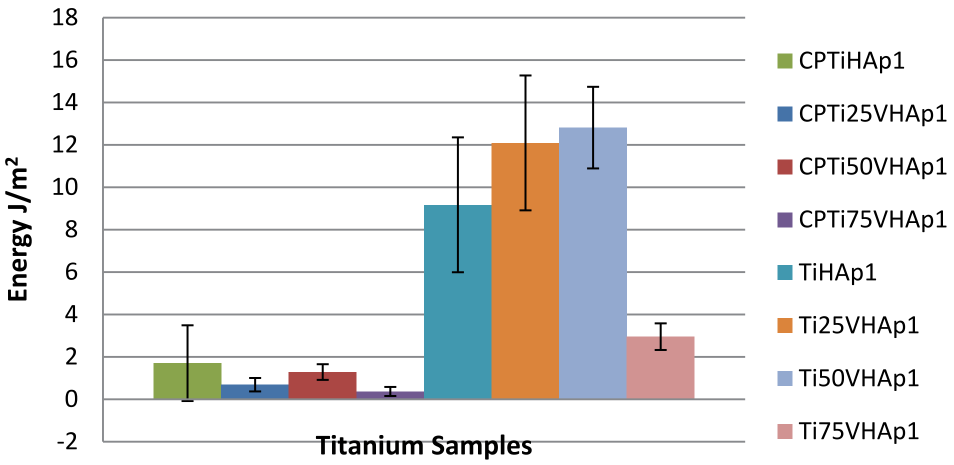

Figure 8.4 *Interface energy of Hydroxyapatite coatings on CP and Ti6Al4V Substrates.*

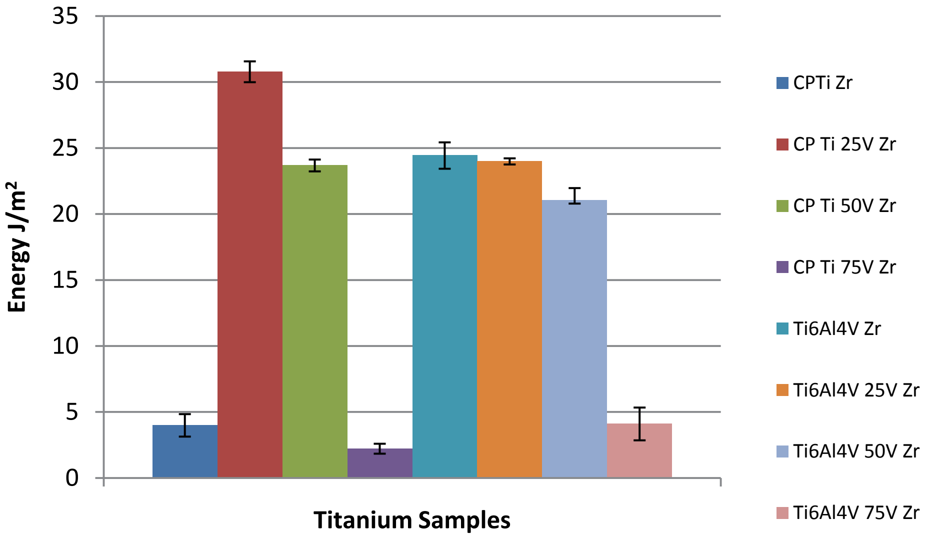

Figure 8.5 *Interface energy of crack free Zirconia coatings on Titanium Substrates.*

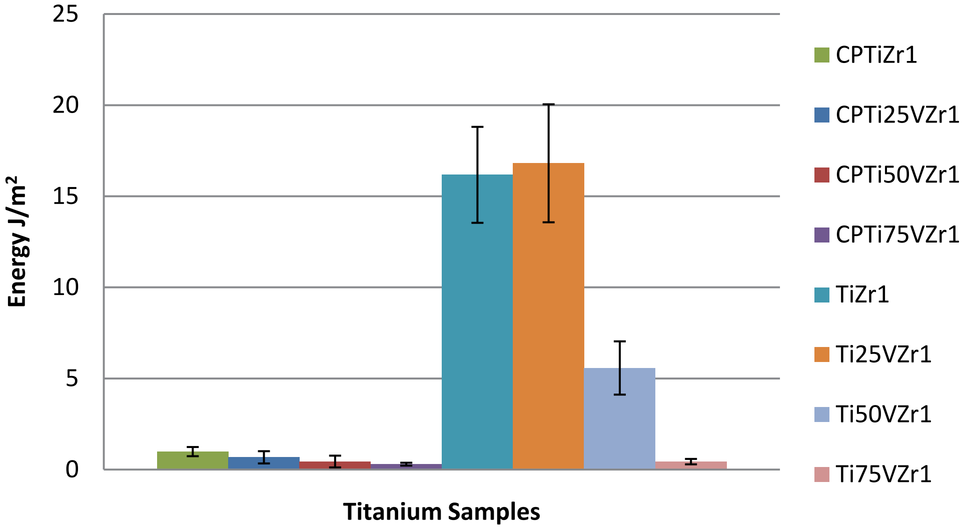

Figure 8.6 *Interface energy of (200nm) cracked Zirconia coatings on Titanium Substrates.*

Figure 8.4 shows the interface energy of the hydroxyapatite coatings on the C.P. and Ti6AL4V substrates. The results show a significant improvement in interfacial adhesion of the films on Ti6AL4V over the C.P. titanium substrates with the anodised 25 volt and 50 volt Ti6Al4V substrate yielding a value of 12.1 and 12.8 J/m^2 compared with values of less than 2 J/m^2 for the C.P. titanium samples.

Figures 8.5 and 8.6 show the differences in the cracked and crack free zirconia coatings with the crack free coating have significantly improved values over the cracked coatings demonstrating the improved properties of the crack free coatings.

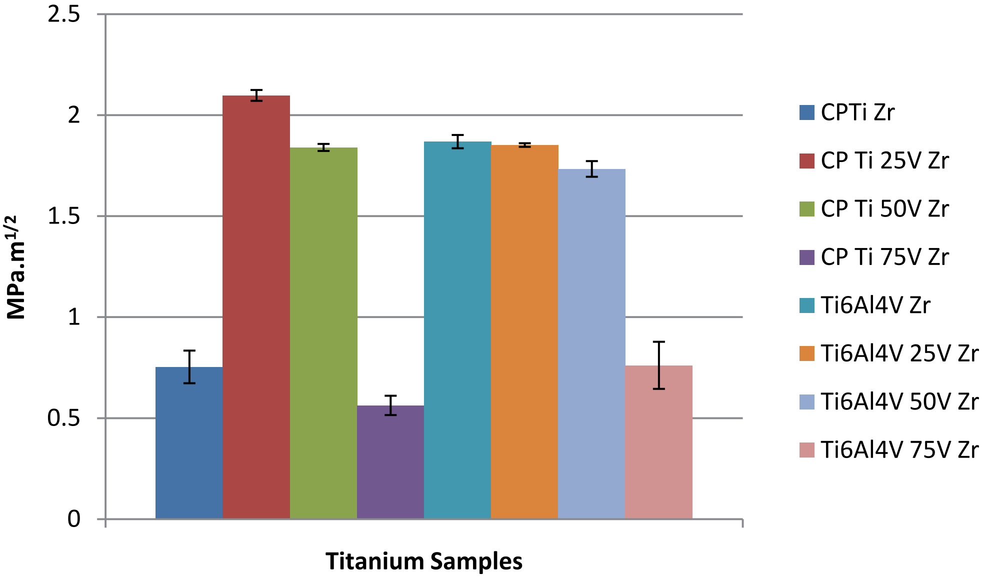

Figure 8.7 *Interface Toughness of Crack Free Zirconia coatings on Titanium Substrates.*

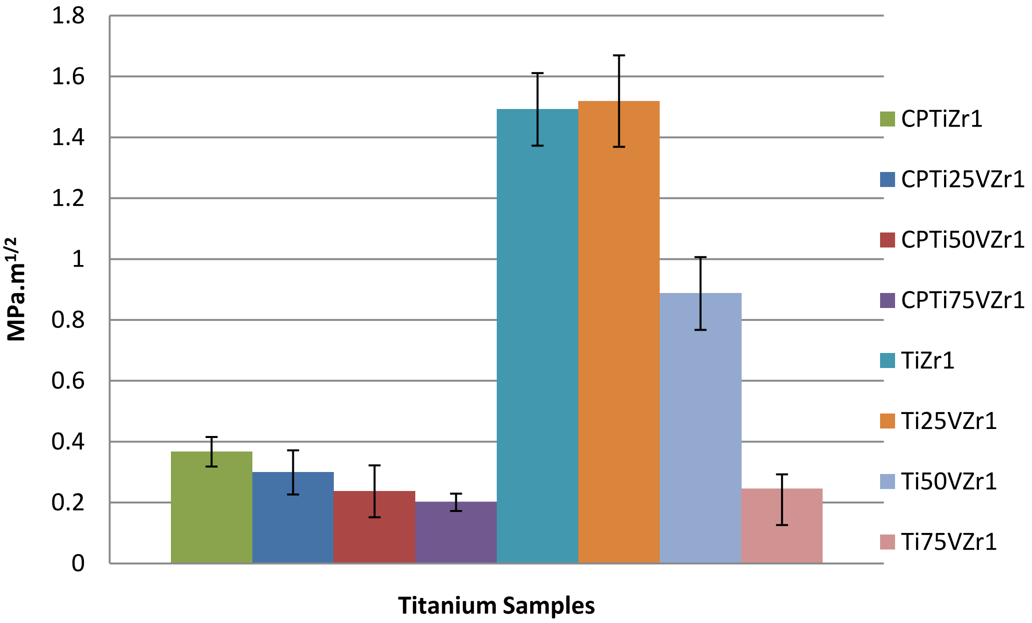

Figure 8.8 *Interface Toughness of Cracked Zirconia coatings on Titanium Substrates.*

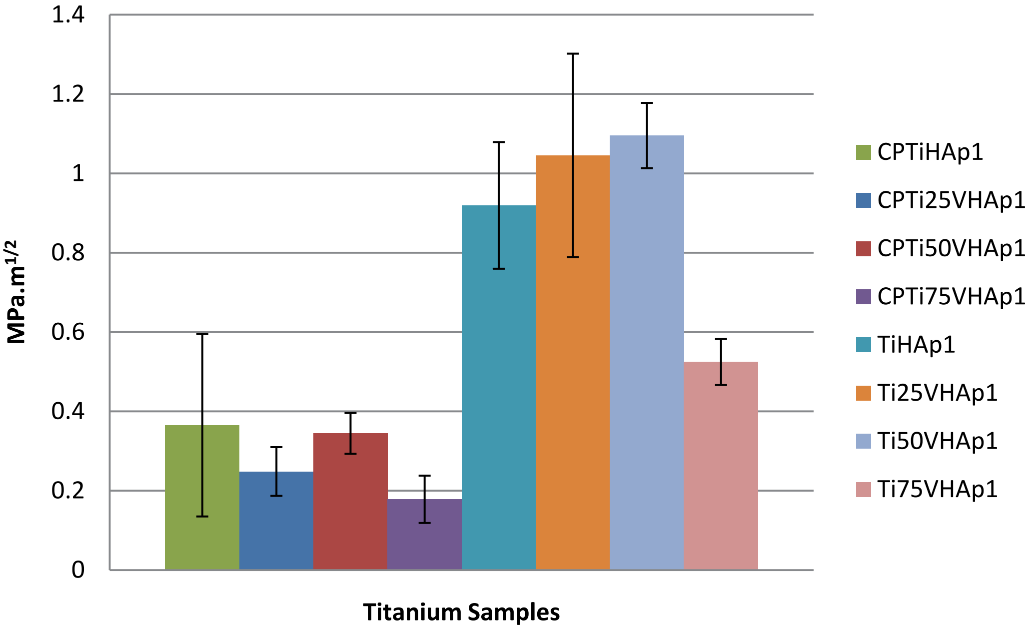

Figure 8.9 *Interface Toughness of Hydroxyapatite coatings on Titanium Substrates.*

Figures 8.7 show that for both substrates the 25 and 50 volt anodised samples for the crack free zirconia show that the interface toughness values in excess of 1.5 MPa.m$^{1/2}$ in addition to them the Ti6Al4V substrate also is in excess of 1.5 MPa.m$^{1/2}$ indicating that these samples all possess good interface toughness values while the other substrates have toughness values half the previously mentioned samples of about 0.75 MPa.m$^{1/2}$.

Figure 8.8 show the effect of the pre-existing cracks in the zirconia coating with all results significantly lower than for the crack-free zirconia coatings for all substrates but like the crack free coatings the Ti6Al4V substrates show higher values than the C.P. titanium substrates.

In figure 8.9 the hydroxyapatite coatings show that again the 25 volt and 50 volt anodised Ti6Al4V substrates demonstrate the highest toughness values with the Ti6Al4V substrate only slightly lower value than the 25 volt and 50 volt samples. The C.P. titanium samples for all substrates recorded values lower than 0.4 MPa.m$^{1/2}$ indicating the poor adhesion that exists for these substrates.

Figure 8.10 shows the C.P. titanium anodised 25 volt substrate with hydroxyapatite showing the cracking and delamination from the micro adhesion testing, indicating the poor adhesion values in the hydroxyapatite coating.

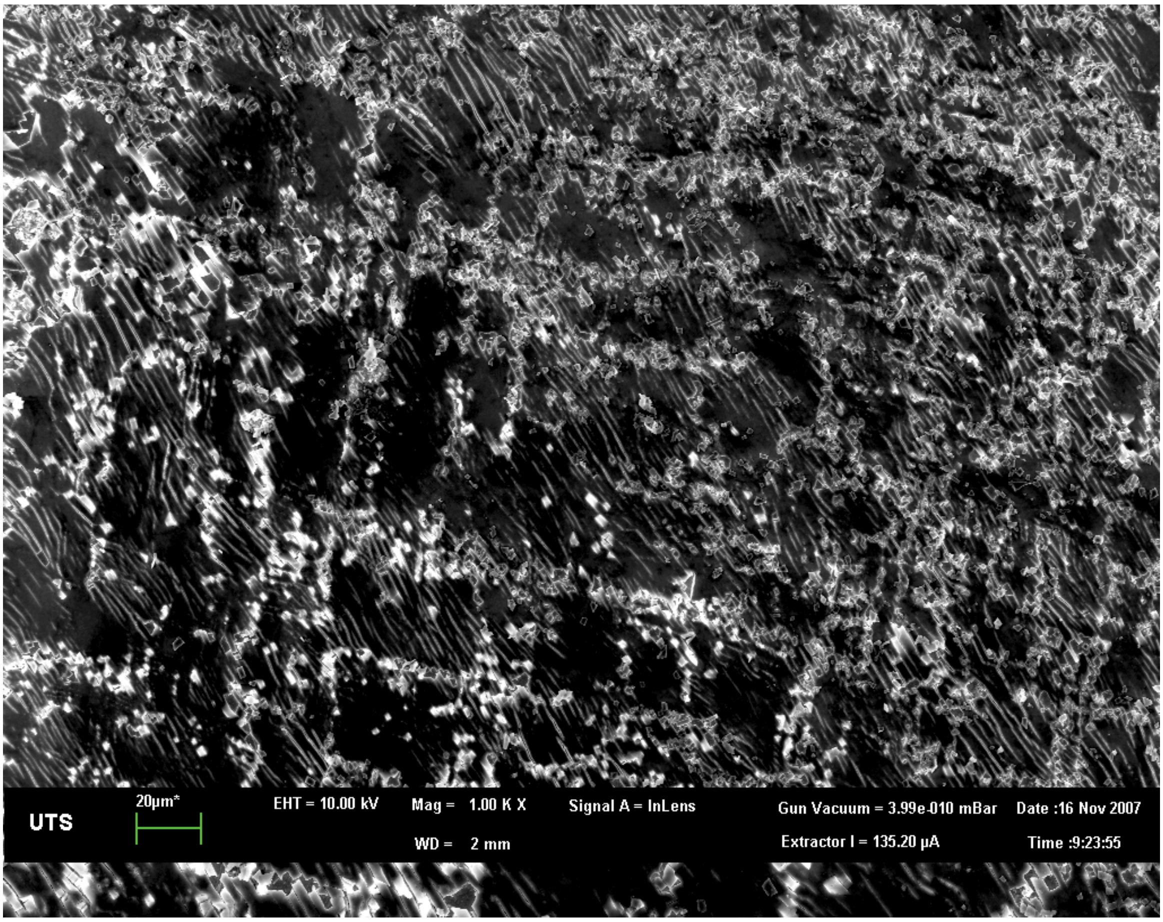

Figure 8.10 *SEM micrograph of 25 Volt anodised C.P titanium sample with hydroxyapatite Coating after Micro-Adhesion Testing.*

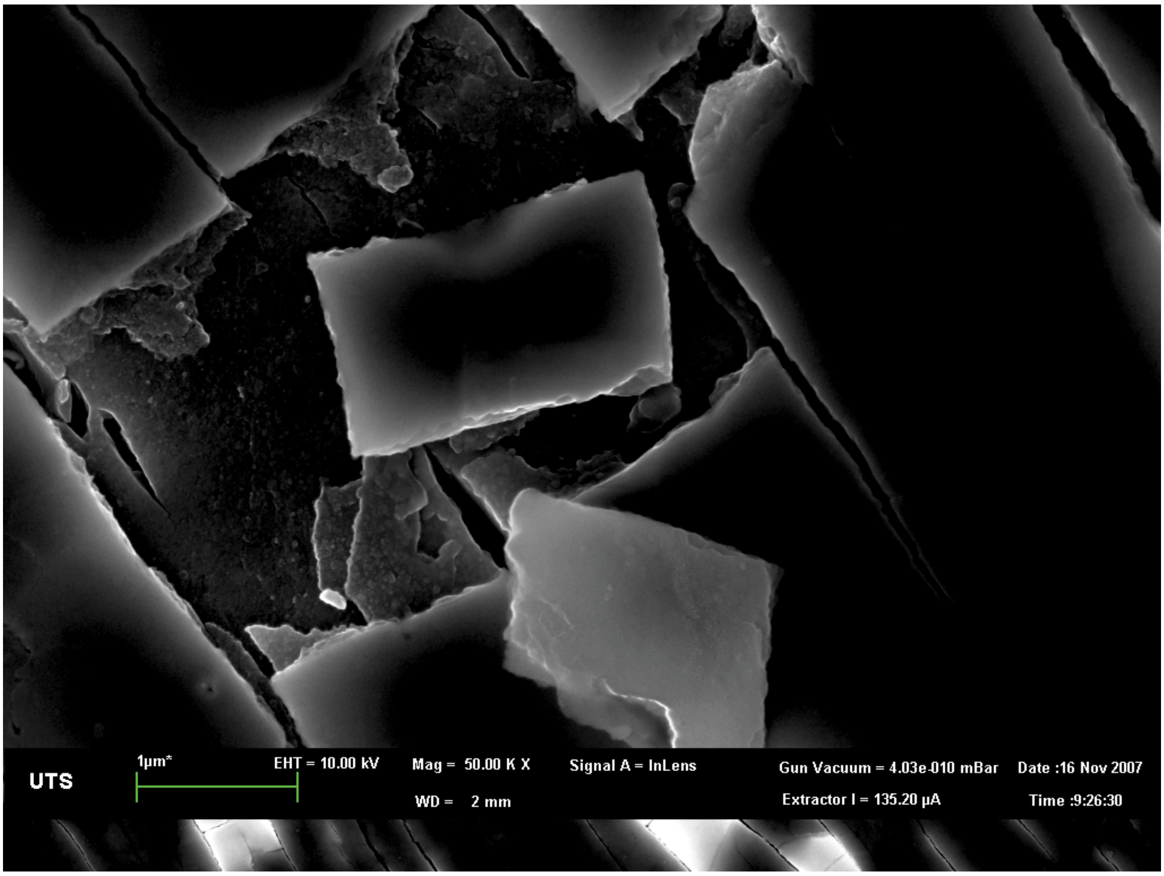

Figure 8.11 *SEM micrograph of 25 Volt anodised C.P titanium sample with hydroxyapatite Coating after Micro-Adhesion Testing.*

Figure 8.11 shows the delamination of the hydroxyapatite coating from the 25 volt anodised titanium substrate showing several large pieces of the hydroxyapatite coating separated from the substrate. Also evident in the SEM micrograph is the cracking in the anodised substrate. There also appears to be some evidence of the hydroxyapatite coating still adhered to the substrate with the hydroxyapatite breaking in the actual hydroxyapatite region of the coating. This type of cracking and delamination is evident in all C.P titanium samples coated with hydroxyapatite.

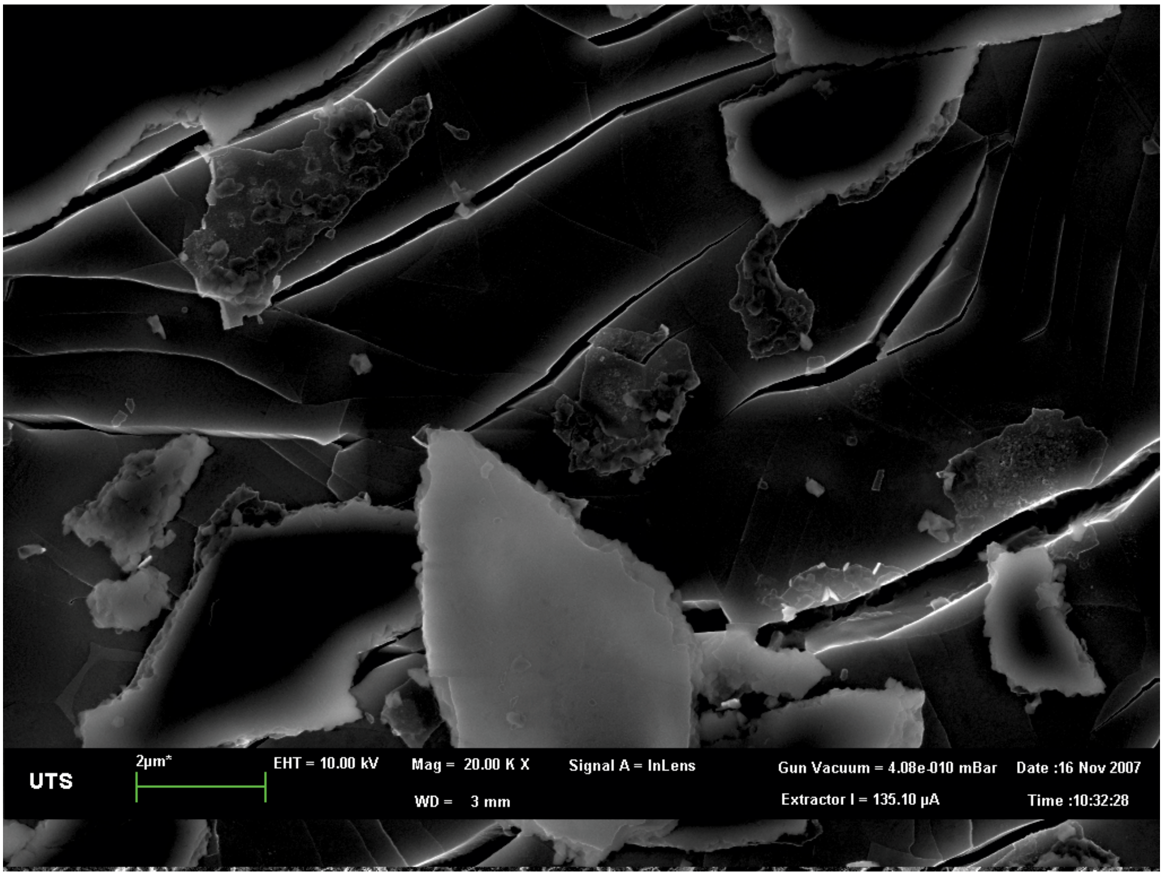

Figure 8.12 *SEM micrograph of C.P titanium sample with hydroxyapatite Coating after Micro-Adhesion Testing.*

The C.P. titanium substrate coated with hydroxyapatite the titanium samples were strained so that shear deformation occurred in the C.P. titanium substrate in addition to the delamination of the hydroxyapatite there are also areas where parts of the hydroxyapatite is still adhered to the substrate shattering in the hydroxyapatite layer itself. Appendix-6 shows the 25 volt anodised substrate with classic shear stress cracks running at 45 degrees to the tensile parallel cracks, there are also areas of delamination in the hydroxyapatite coating.

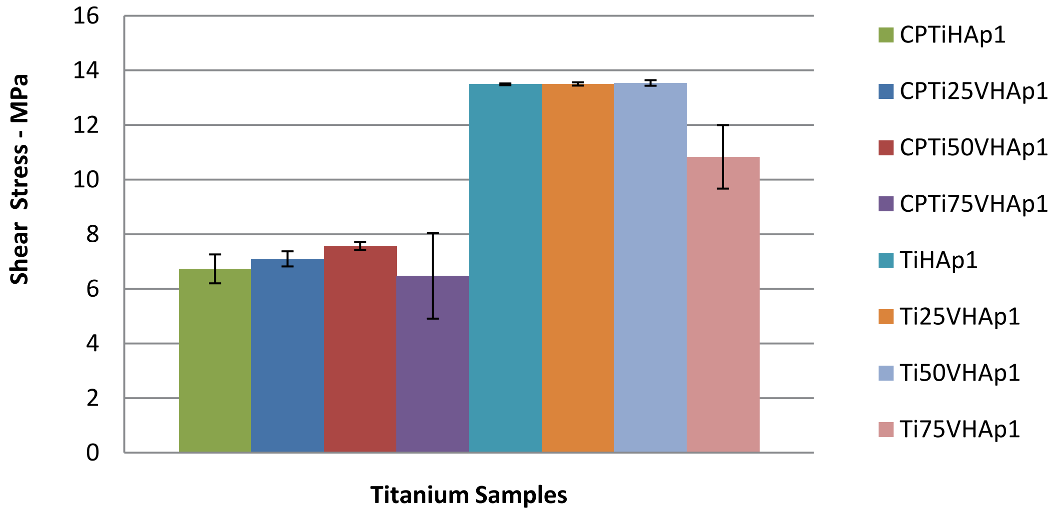

Figure 8.13 *Shear stress of hydroxyapatite coatings on Titanium Substrates.*

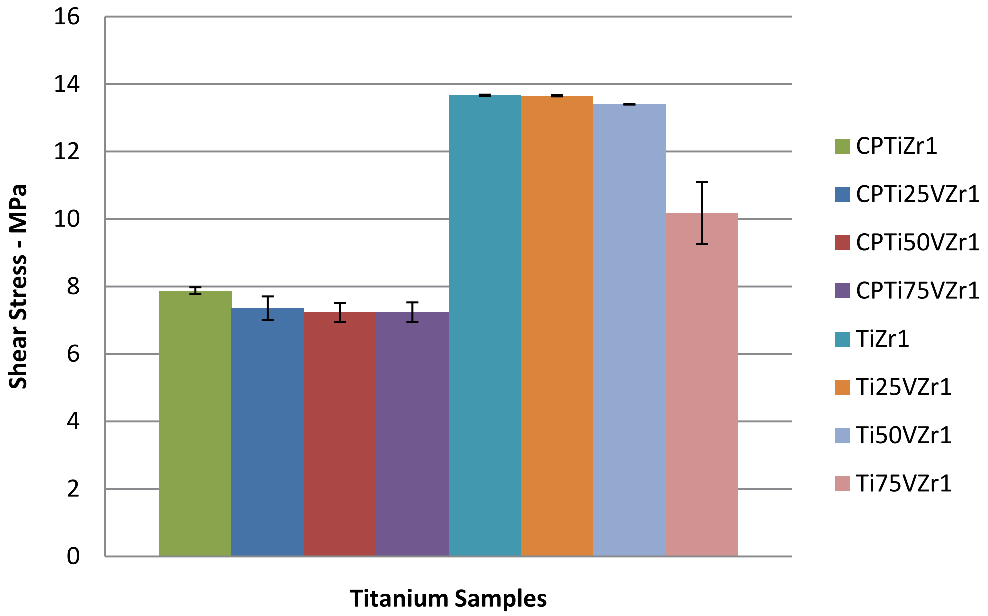

Figure 8.14 *Shear stress of Zirconia coatings on Titanium Substrates.*

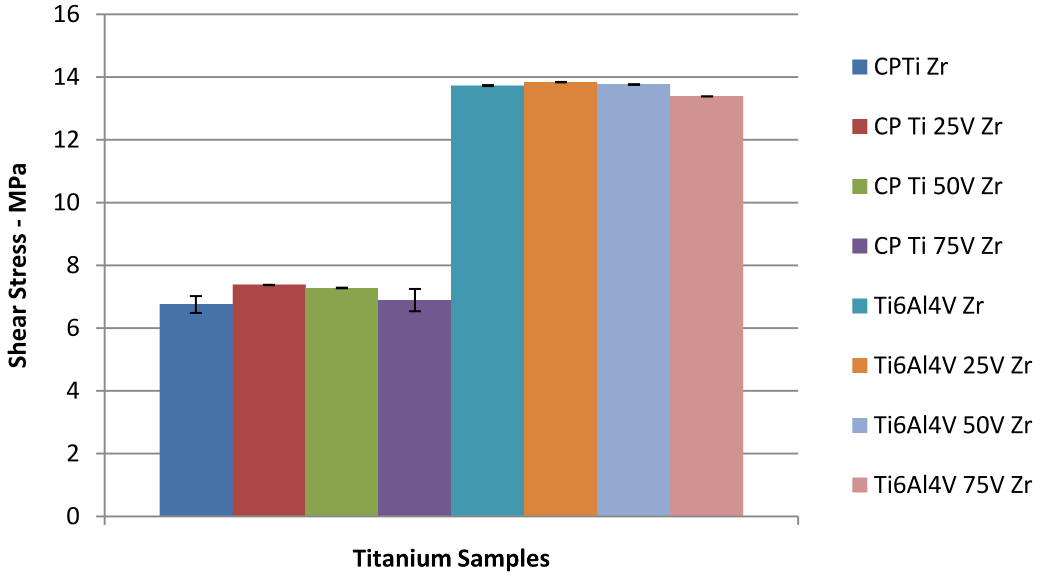

Figure 8.15 *Shear stress of Thin Zirconia coatings on Titanium Substrates.*

Figures 8.13, 8.14 and 8.15 show the shear stress results are consistent in all titanium substrates with the Ti6Al4V yielding slightly higher values regardless of the sol gel coating on the substrate and this is in line with expectations as is visible in figure 8.12 with the shear stress in the substrate evident with cracks running both in the direction of the micro adhesion testing and 45 degrees to the micro adhesion testing, characteristic of shear stress in the base titanium substrate.

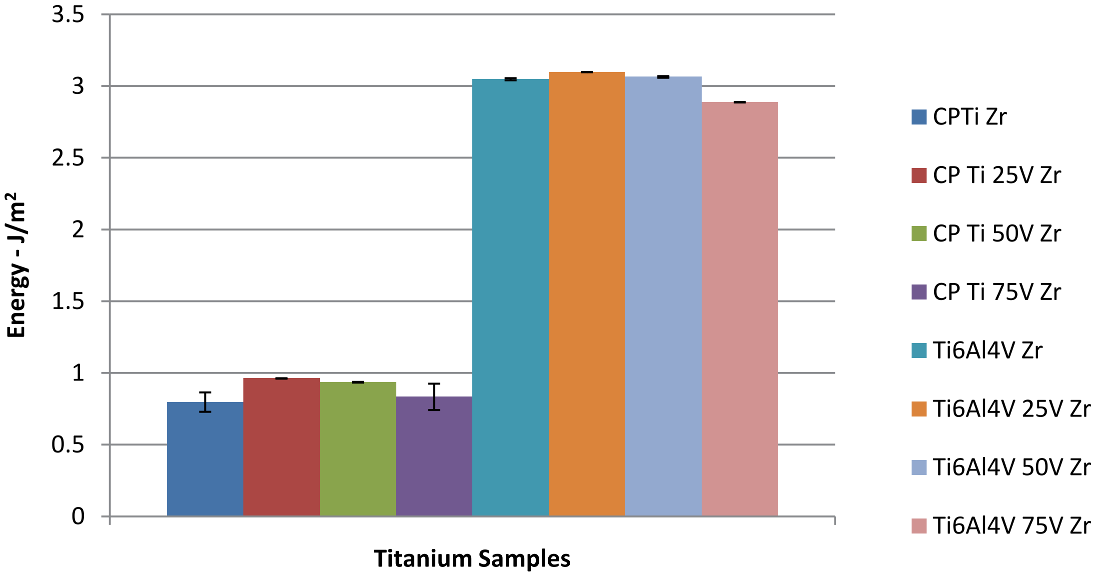

Figure 8.16 *Film Fracture Energy of Thin Zirconia coatings on Titanium Substrates*

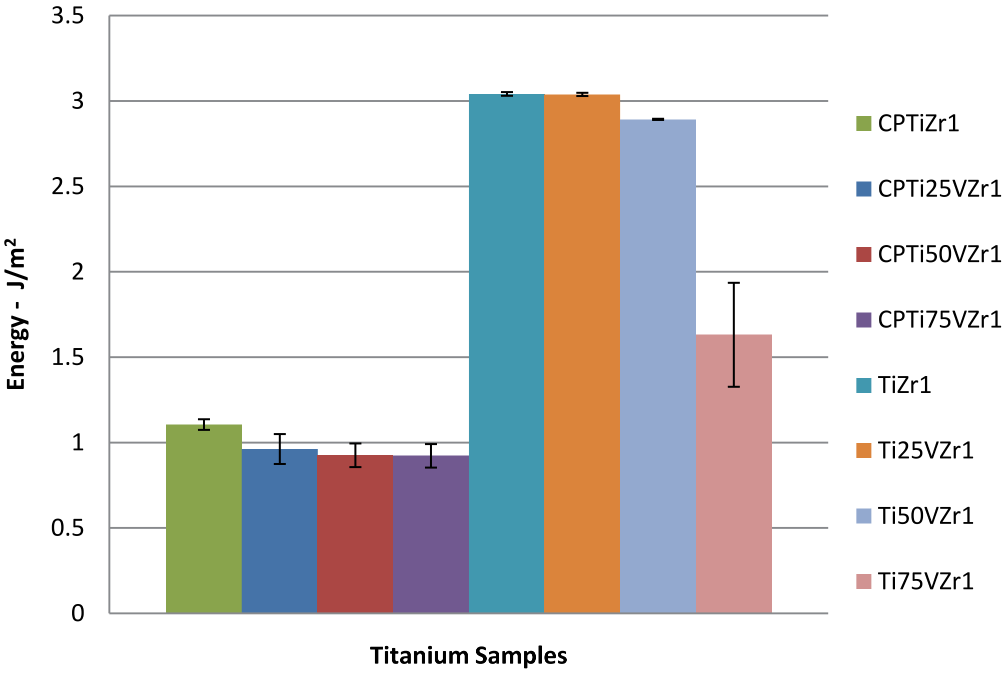

Figure 8.17 *Film Fracture Energy of Zirconia coatings on Titanium Substrates*

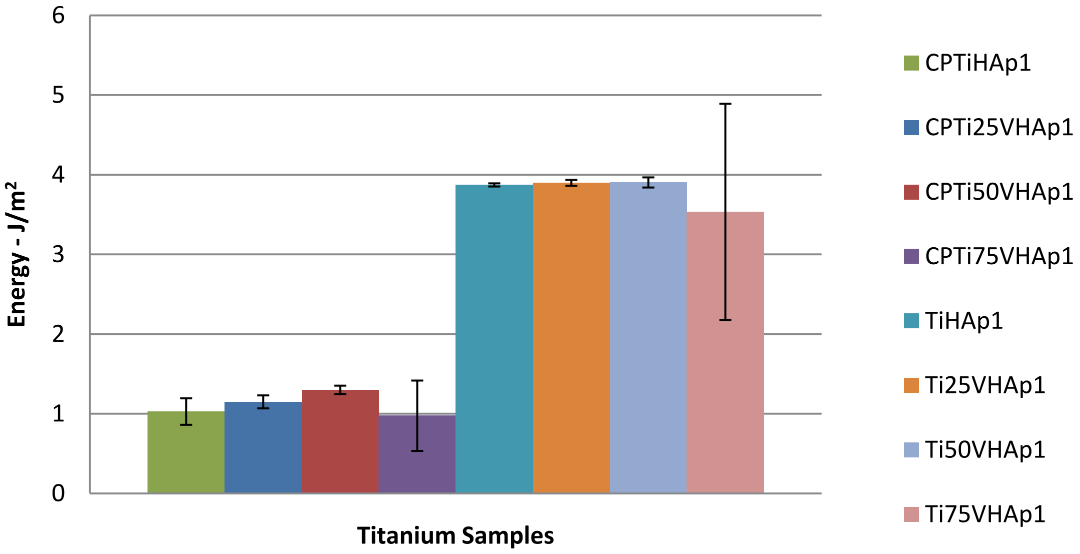

Figure 8.18 *Film Fracture Energy of Hydroxyapatite coatings on Titanium Substrates*

Figures 8.16, 8.17 and 8.18 show the film fracture energy for the zirconia and hydroxyapatite sol gel coatings on titanium and anodised titanium substrates. What is evident in the charts is the lower values for the C.P. titanium in both the zirconia and hydroxyapatite coatings showing that the substrate is having some effect on the coatings although the slight differences between the 25 volt, 50 volt and 75 volt show that this effect is small regardless of the coating.

8.7 MICRO-ADHESION CONCLUSIONS

The zirconia sol gel initially used before modification when spin coated yielded a cracked structure due to the zirconia coating thickness being above the 200 nm of the critical cracking thickness for zirconia sol gel coatings as described by Mehner *et al.* and Scherer. [129, 130] The modification of the zirconia sol gel coating reducing the viscosity to 10-12 Centipoises with 1-butanol resulted in a zirconia coating thickness around 100 nm after spin coating at 3000 rpm for 20 seconds that was completely crack free on all substrates tested. These coatings produced are in agreement with the work of Mehner *et al.* and Scherer on the critical thickness of the zirconia sol gel coating being below 200nm despite the fact the solutions they used have differing composition and chemistry it is argued that the residual stress existing in the zirconia thin film itself is the limiting factor in the sol gel films. [129, 130]

Testing for both the cracked and crack free zirconia thin films was carried out with the crack free yielding superior results on every test from the interface energy to the film toughness results, as expected. Of interest was the 25 volt and 50 volt result on the C.P. titanium substrate which yielded comparable results with the Ti6Al4V substrate, 25 volt Ti6Al4V substrate and the 50 volt Ti6Al4V substrate in both the interface energy calculations and the interface toughness calculations. Yet the shear stress, film toughness and film fracture energy calculations for the 25 volt and 50 volt result on the C.P. titanium substrate yielded far lower results indicating the improved adhesion properties evident on the Ti6Al4V substrates.

The Ti6Al4V 75 volt anodised substrate yielded significantly lower values for all calculations indicating that the increased oxide thickness around 150 nm was inhibiting the performance of the coating due to the failure of the anodised oxide film during tested as evidenced in appendix-13 and 14 which show the large cracks from the micro adhesion testing and shear stress also occurring in the anodised substrate leading to large areas of delamination in the zirconia coating, next to areas where the zirconia coating is still firmly adhered to the anodised substrate. Appendix-15 shows the 50 volt anodised titanium substrate with micro- adhesion testing cracks evident in the zirconia coating but no delamination of the zirconia coating indicating the improved adhesion properties of this zirconia coating on this substrate.

The hydroxyapatite results yielded significantly lower results than the crack free zirconia coatings but this is in part due to the nature of the hydroxyapatite coating which is a brittle coating. But as in the zirconia results the 25 volt and 50 volt anodised Ti6AL4V substrates yielded the highest results from the Evans interface toughness and interface energy calculations with the shear stress and film toughness calculations showing the Ti6Al4V substrate on a par with the 25 volt and 50 volt anodised samples. The 75 volt anodised samples again show a lower fracture energy and film toughness in comparison to the other anodised substrates similar to the zirconia results further adding evidence that the increased anodised oxide film formed is failing before the hydroxyapatite coating leading to the low adhesion properties of this substrate.

8.8 NANO-INDENTATION TESTING

The nano-indentation testing was carried out at ANSTO and was based on the work of Field and Swain [179, 180] to determine the Young's modulus and hardness of the thin sol-gel coatings. In this technique the load is increased incrementally and the penetration of the indenter is measured at each step. The increasing load produces corresponding increases of elastic/plastic deformation. The separation of the data into the elastic and plastic components is critical for the information needed to obtain the mechanical properties of the material tested.

Indentation with multiple partial unloading is described by Field and Swain [179, 180], whose method allows for the elastic component to be estimated directly at each step. Data obtained from this method is presented as a plot of load versus penetration.

The quoted literature values for hydroxyapatite is in the range of 35 – 120 GPa for bulk HAp [6, 181], although this value is dependent on porosity and the presence of impurities, etc. [6, 181]. The nano-indention values shown in figures 8.19 and 8.20 for the hydroxyapatite and zirconia are respectively 25 GPa and 138 GPa.

Elastic modulus and hardness are important parameters used by industry with the indentation techniques measuring a wide range of materials including thin films [182] with the hardness values obtained in figures 8.21 And 8.22 for the hydroxyapatite and zirconia sol gel coatings yielding a hardness value of 0.38GPa for the hydroxyapatite coating and a hardness value of 4.2GPa for the zirconia coating. M. Anast, B. Ben-Nissan, J.R. Bartlett, J.L. Woolfrey, J.M. Bell, J.T. Bell, D.R. de Villers, L. Spiccia, B.O. West, G.R. Johnson and I.D. Watkins in the first published work on zirconia sol gel nano hardness yielded a hardness value of 10.3GPa for the strained tetragonal zirconia film fired at 500°C [125] which is very similar to the bulk hardness values for zirconia. It is also consistent with their work at higher temperatures yielding lower nano hardness values for the tetragonal zirconia film as it is converted to monoclinic zirconia at higher temperatures, with the zirconia films produced in this work all conducted at 550°C and the tetragonal form of zirconia still detected by XRD at this temperature, indicating that this temperature is close to the optimum for the tetragonal form of zirconia formed by zirconium alkoxide, with higher temperatures leading to monoclinic zirconia formation. M.J. Paterson, P.J.K. Paterson, and B. Ben-Nissan yielded a hardness value of 6.12 GPa for a 900nm thick zirconia film fired at a similar temperature. [126]

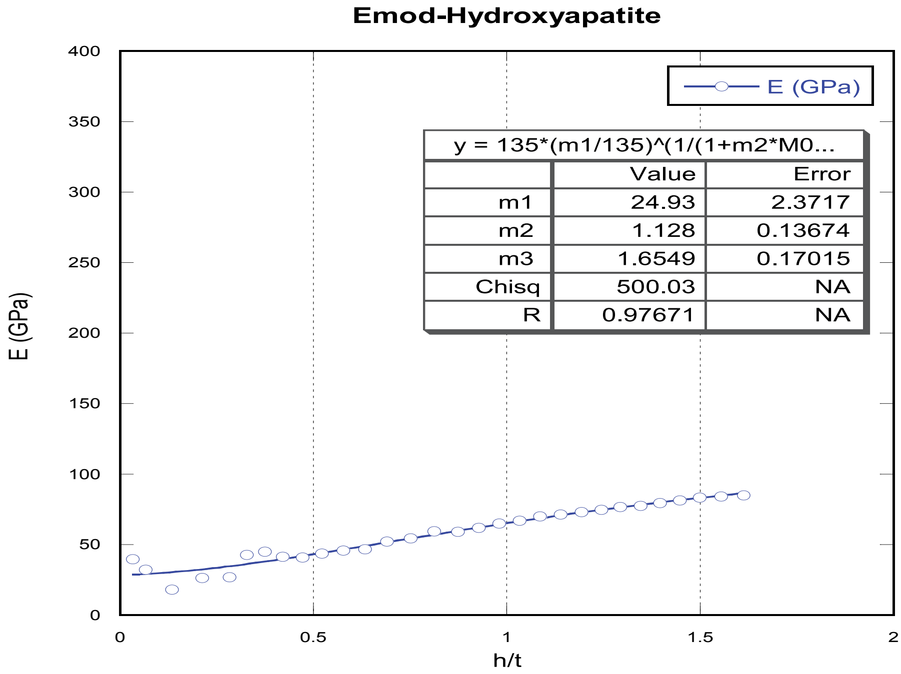

Figure 8.19 *E Mod Nano-Indentation graph of Hydroxyapatite Sol Gel Coating*

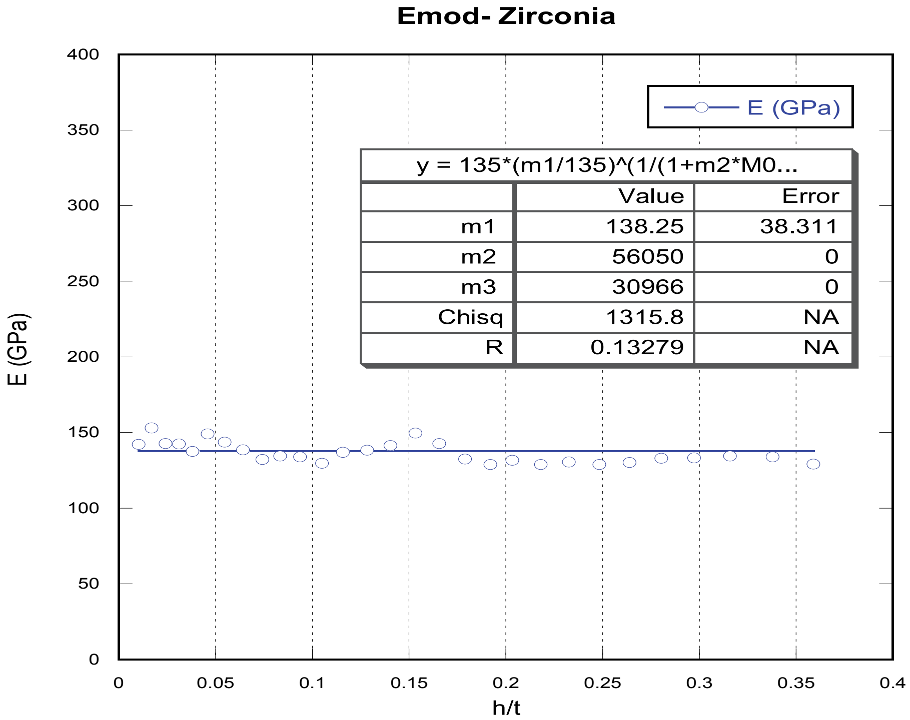

Figure 8.20 *E Mod Nano-Indentation graph of Zirconia Sol Gel Coating*

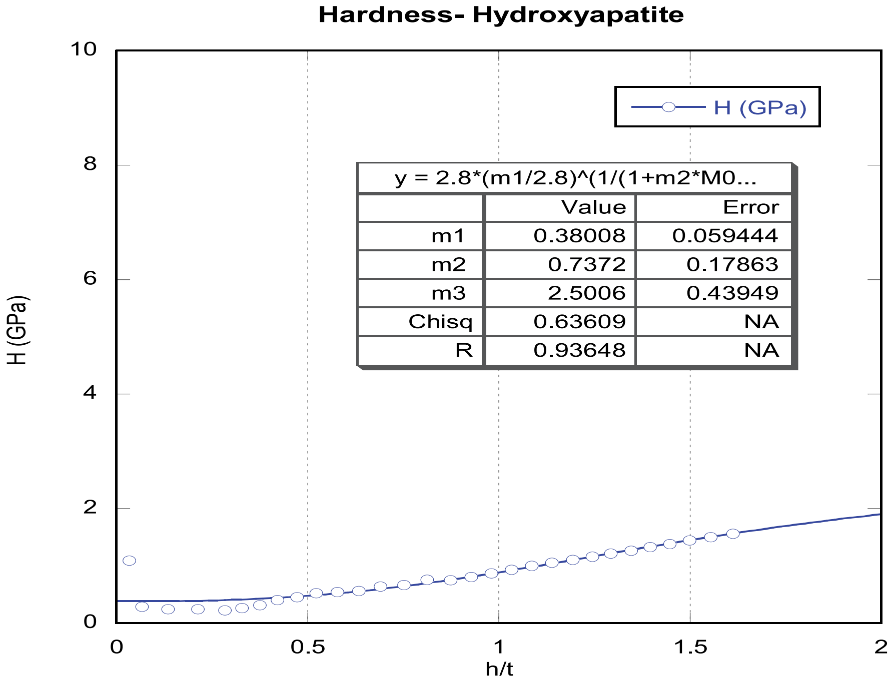

Figure 8.21 *Hardness measurements in Nano-Indentation graph of Hydroxyapatite Coating*

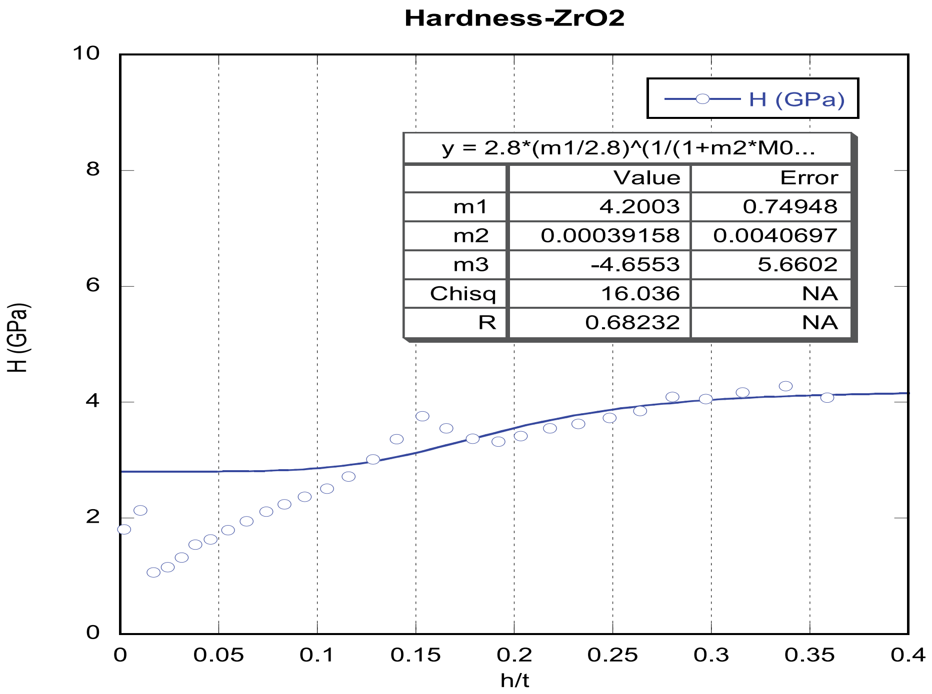

y = 2.8*(m1/2.8)^(1/(1+m2*M0...		
	Value	Error
m1	4.2003	0.74948
m2	0.00039158	0.0040697
m3	-4.6553	5.6602
Chisq	16.036	NA
R	0.68232	NA

Figure 8.22 *Hardness Measurements in Nano-Indentation graph of Zirconia Coating*

Elastic modulus and hardness are important parameters used by industry with the indentation techniques measuring a wide range of materials including thin films [182] with the hardness values obtained in figures 8.21 And 8.22 for the hydroxyapatite and zirconia sol gel coatings yielding a hardness value of 0.38GPa for the hydroxyapatite coating and a hardness value of 4.2GPa for the zirconia coating.

The Appendix 7 through to Appendix 12 show the E modulus values from 25 volt anodised substrate at 198.7 GPa to the 50 volt anodised titanium substrate at 153.3 GPa and the 75 volt anodised substrate at 138.5 GPa. The Hardness values for the 25 volt substrate are 7.6 GPa, the hardness value of the 50 volt substrate is 5.6 GPa and the hardness value for the 75 volt substrate is 5.1 GPa.

CHAPTER 9 – TRIBOLOGICAL PROPERTIES

9.0 TRIBOLOGY

Tribology is the science of interacting surfaces in relative motion and of related areas [183, 184]. When two nominally flat surfaces are in contact, surface roughness causes contact to occur at contact points and interfacial adhesion occurs [183, 184]. Friction is the resistance to motion that occurs when one body moves over another [183, 184]. Wear is the surface damage or removal of material from one or both bodies in moving contact. Selection of materials, coatings and surface treatments is made to minimise friction and wear [183, 184].

9.1 FRICTION

The co-efficient of friction is defined as the ratio of friction force to the normal load [183, 184]. Friction involves mechanisms of energy dissipation during relative motion. As two surfaces are brought into contact together, contact occurs at asperities, the load is supported by the deformation of the contacting asperities, and the distinct contact points are formed [183, 184]. The proximity of asperities results in adhesive contacts caused by either physical or chemical interactions.

Radchik *et al*. [185, 186] state that when two surfaces are brought together, contact will initially occur at a few points, and as the surfaces move closer together, a number of large asperities on the two surfaces come into contact. The total area of these point contacts forms a real area of contact.

Friction arises due to adhesion and deformation [183, 184]. The adhesion term constitutes the force required to shear the adhesive bonds formed at the interface in regions of real areas of contact [183, 184]. In the case of metals and ceramics, the deformation term constitutes the force needed for deformation of asperities (micro-scale) and/or ploughing, grooving or cracking of one surface by asperities of the harder mating material (macro-scale) [183, 184]. Ploughing of one or both surfaces can also occur due to wear particles trapped between the surfaces [183, 184].

Adhesion is present in all contacts and the degree of adhesion is a function of the interface conditions. The adhesive component of friction can be reduced, by reducing the real area of contact and the adhesive strength. The deformation component of friction can also be reduced by reducing the interface roughness, by selecting materials of close to equal hardness and by removing wear and contaminant particles from the interface [183, 184].

9.2 CERAMICS WEAR

Ceramics have high mechanical strength, do not lose much mechanical strength or oxidise readily at elevated temperatures and are resistant to corrosive environments [183, 184]. As previously stated by Radchik *et al*. [185, 186] the real area of contact occurs when the taller asperities come into contact as two surfaces move closer together. This is of relevance to ceramics, due to the difficulties involved in surface polishing and surface preparation of the ceramics on both a micro and nanoscale with regard to the size and shape of the asperities, and the mechanical properties of the two surfaces in contact [185, 186].

9.3 TITANIUM – FRICTION PROPERTIES

The co-efficient of friction of CP titanium is in the range of 0.30 –0.4, with lower figures in the range of 0.25 – 0.30 for titanium alloys [2, 187]. Three fundamental factors combine to give titanium its high co-efficient of friction and cause the poor tribological properties of the metal. The first arises from titanium's atomic structure, which can be marginally improved by bulk or surface alloying to form a harder and more wear resistant structure. The second factor comes from the crystal structure of titanium. Modification by alloying occurs naturally in a range of titanium alloys, which, to various extents, offers better resistance to wear, compared to CP titanium.

The third problem is the relatively low tensile and shear strengths of the titanium oxide film. When adhesive bonding occurs in rubbing contact with other adjacent titanium or other metal surfaces, the fracture occurs in the oxide rather than at the interface, resulting in large amounts of material transfer, galling, and high wear rates [72, 121].

It is possible to overcome this problem, and indeed the other two factors mentioned, by removing the titanium entirely from the tribological system by coating with another material, in this case with the zirconia sol-gel.

Tribology Testing Matrixes

No Anodising- CP Titanium
No Coating - G
ZrO2 Coated - 550˚C - H
ZrO2 Coated - 550˚C – 2 x ZrO2 Layers - I
50V Anodised - CP Titanium
No Coating - J
ZrO2 Coated - 550˚C - K
ZrO2 Coated - 550˚C – 2 x ZrO2 Layers - L
No Anodising- Ti6Al4V
No Coating - M
ZrO2 Coated - 550˚C - N
ZrO2 Coated - 550˚C – 2 x ZrO2 Layers - O
50V Anodised -Ti6AL4V
No Coating - P
ZrO2 Coated - 550˚C - Q
ZrO2 Coated - 550˚C – 2 x ZrO2 Layers - R

Table 9.1 *Tribology Testing Matrixes for Titanium Samples with Cracked Zirconia Coating.*

9.4 TRIBOLOGY TESTING

The tribology testing was conducted under the supervision of Professor Alan Eberhardt at the Department of Biomedical Engineering, University of Alabama at Birmingham. The present wear testing was performed using an Ortho-pod MTI, Watertown, MA), a six-station pin-on-plate type wear-testing machine with independent servo-controlled variables that correspond to rotary motion of both the plate and the six pins, and the normal load on the six pins.

The pin rotation feature gives this machine the ability to generate pin/plate sliding motions that are typically not available on standard pin-on-disc machines. The Ortho-pod is an excellent tool for the testing of implant materials whose wear characteristics depend upon various sliding directions (crossings) as well as load, in a fully lubricated environment.

9.4.1 TRIBOLOGY TESTING PROCEDURE

Commercial grade ultra-high molecular weight polyethylene was machined to provide pins for the present tests. The ultra-high molecular weight polyethylene was chosen for the fact that it is used in a variety of medical implants, such as the socket in some hip joints. The pins were tested against a variety of titanium discs as shown in Table 9.1.

Compression moulded ultra-high molecular weight polyethylene irradiated in Argon at 25 – 40 kGy (Arcom®, Biomet, Inc., Warsaw, IN) was machined into cylindrical wear pins 9.5 mm in diameter with a step down to 4.76 +/- 0.03 mm diameter on the contacting surface, giving a contact area of approximately 17.8 mm^2 (Figure 1). The Arcom® pins were used for the first nine tests. Biomet was unable to provide another set of Arcom® for the final test, and non Arcom® pins were used. For the tenth test, virgin UHMWPE from resin type two, and the fabricated material met the ASTM requirements of F648-00. The pins were soaked in distilled water for a minimum of two weeks prior to wear testing.

9.4.2 FRICTIONAL WEAR TESTING

Before tests began, pins and disks were sonicated in a 10% LiquiNox® (Alconox Inc., White Plains, NY) solution, rinsed with deionised water, and submerged in ethyl alcohol. Then all of the samples were dried in a vacuum for thirty minutes. The pins were each weighed five times on a Mettler Toledo AG245 microbalance (Columbus, OH) with a resolution to .00001 grams.

During each test, the pins and disk samples were submerged in a lubricant of bovine serum (Hyclone, Logan, UT). It was mixed into a lubricant that contained 53% bovine serum and deionised water. Anhydrous ethylenediaminetetraacetic acid, or EDTA (Sigma-Aldrich, St. Louis, MO), was added to bind the calcium in the solution and prevent precipitation of abrasive components onto the bearing surfaces. Sodium azide was also added to prevent bacterial depredation. The mixture was filtered with a .22 micron filter, and warmed to 37° C. The lubricant temperature was maintained at body temperature throughout testing.

Wear testing was performed in an OrthoPOD® six station pin-on-disk machine (Advanced Mechanical Testing, Inc., Watertown, MA). Ten tests were performed. The C.P. samples were tested separately from the Ti6Al4V samples. Each test had several different samples with different coatings. The sample positions were rotated after each test. Six pins and five disks were used during each test. The sixth pin was used for a soak control, and had no articulation or wear.

The OrthoPOD® recorded the coefficient of friction and three dimensions, x, y and z, of force at intervals of 25,000 cycles. Each test had a length of 500,000 cycles. The horizontal force measurements had an accuracy of +/- 2N, and the vertical forces were accurate +/- 8N. The polyethylene pins were loaded end wise into the OrthoPOD® against the test face of the metal disks. The contact surface area of the metal counter face is flat. The wear path followed a figure eight pattern at a frequency of 1.5 Hz and a sliding speed of .4 m/s. A constant load of 10.7 MPa was applied.

After the 500,000 cycles the pins and disks were removed from the machine. The pins were soaked in deionised water for two days and measured again to calculate mass loss. The soak control accounted for any change in mass due fluid absorption.

9.5 STATISTICAL ANALYSIS

Due to the fact that n = 3 or n = 4 for each group of specimens, the Kruskal-Wallis one-way analysis of variance by ranks was applied to test the hypothesis that the mean wear rates among the different test groups were the same. This type of non-parametric statistics substitutes the ranking of the wear value for the actual value and the sum of ranks is used to test for differences among the group. The test statistic in this case is designated, H, and is calculated according to the following equation:

$$H = \frac{12}{n(n+1)}\left(\frac{S_1^2}{n_1} + \frac{S_2^2}{n_2} + \ldots + \frac{S_k^2}{n_k}\right) - 3(n+1) \qquad (9.1)$$

where S_k is the sum of the ranks for sample k, n_k is the number of samples of each group k, n is the combined number of observations for each sample, and k is the number of populations.

k-1 represents the degrees of freedom – in this case, k = 12, therefore, k-1 = 11. For this number of degrees of freedom, the critical H value at the 0.05 significance level is 19.675. [188]

9.6 RESULTS AND DISCUSSION

The calculated H statistic of 38.563 indicated that indeed there are statistically different wear rates among the groups ($p < 0.001$). No post-hoc analysis is available to test for differences between individual groups – the Kruskal-Wallis approach simply provides a ranking of best to worst.

In this light, the four best performing surfaces were, from best to worst, surfaces Cp Ti once coated with ZrO_2 at 550° C, uncoated anodised CP Ti, uncoated Ti6Al4V samples, and uncoated Ti6Al4V anodised samples. The four worst performing surfaces were all coated twice with ZrO_2 at 550° C. From worst to best, the worst performing surfaces are CP Ti, anodised Ti6Al4V, Ti6Al4V, and anodised CP Ti. Uncoated CP Ti, anodised CP Ti once coated with ZrO_2 at 550° C, Ti6Al4V once coated with ZrO_2 at 550° C, and 50V Anodised Ti6Al4V once ZrO_2 coated at 550° C were ranked among the middle of the pack as demonstrated in figure 9.1 and table 9.2.

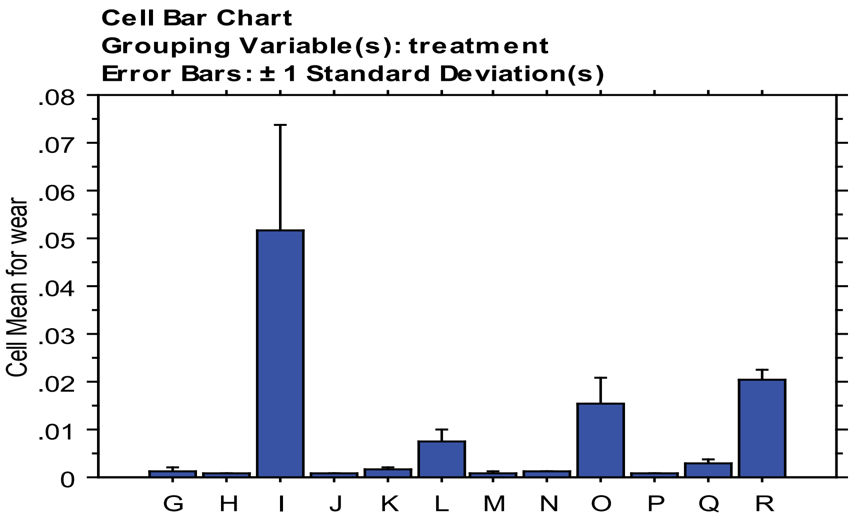

Figure 9.1 *Wear chart showing material loss after testing*

Kruskal-Wallis Test for wear
Grouping Variable: treatment

DF	11
# Groups	12
# Ties	1
H	38.563
P-Value	<.0001
H corrected for ties	38.566
Tied P-Value	<.0001

2 cases were omitted due to missing values.

Kruskal-Wallis Rank Info for wear
Grouping Variable: treatment

	Count	Sum Ranks	Mean Rank
G	4	70.000	17.500
H	4	14.000	3.500
I	4	160.000	40.000
J	4	26.000	6.500
K	4	88.000	22.000
L	4	122.000	30.500
M	3	36.000	12.000
N	3	49.500	16.500
O	3	105.000	35.000
P	3	41.500	13.833
Q	3	81.000	27.000
R	3	110.000	36.667

2 cases were omitted due to missing values.

No Anodising- CP Titanium
No Coating - G
ZrO2 Coated - 550°C - H
ZrO2 Coated - 550°C – 2 x ZrO2 Layers - I
50V Anodised - CP Titanium
No Coating - J
ZrO2 Coated - 550°C - K
ZrO2 Coated - 550°C – 2 x ZrO2 Layers - L
No Anodising- Ti6Al4V
No Coating - M
ZrO2 Coated - 550°C - N
ZrO2 Coated - 550°C – 2 x ZrO2 Layers - O
50V Anodised -Ti6AL4V
No Coating - P
ZrO2 Coated - 550°C - Q
ZrO2 Coated - 550°C – 2 x ZrO2 Layers - R

Table 9.2 *Wear tables for zirconia coated titanium samples and list showing samples used in testing*

The original hypothesis, that the zirconia coating of titanium surfaces would create less wear is supported in the case of the single coated at 550°C C.P. Titanium sample. The next best performing surfaces were all without a coating of zirconia. The rest of the coated surfaces failed to support the suspicion that coated surfaces would outperform uncoated surfaces. After recognizing that the single coated C.P. Titanium outperformed the uncoated surfaces, the remaining coated surfaces were outperformed by the uncoated surfaces. It should also be considered that due to an inability to source all the UHMWPE pins from the same source there may have been a slight discrepancy introduced further testing is undergoing to rectify this problem in testing.

The main reason the zirconia coated samples did not show better wear results is due to the fact that the zirconia coating was cracked due to the zirconia coating thickness being above the critical cracking thickness of zirconia as stated by Mehner *et al.* and Scherer [129, 130]

This was in part due to the unmodified zirconia solution and a set of crack free samples was prepared and sent over to the University of Alabama for testing and these results are integral to obtaining a more accurate idea of the tribological properties of the zirconia coatings. Figure 9.3 and 9.4 show the cracked coatings of the zirconia coating used in the tribological testing with the C.P. titanium sample having significantly less cracking in the zirconia coating compared to the 75 volt anodised C.P. titanium sample.

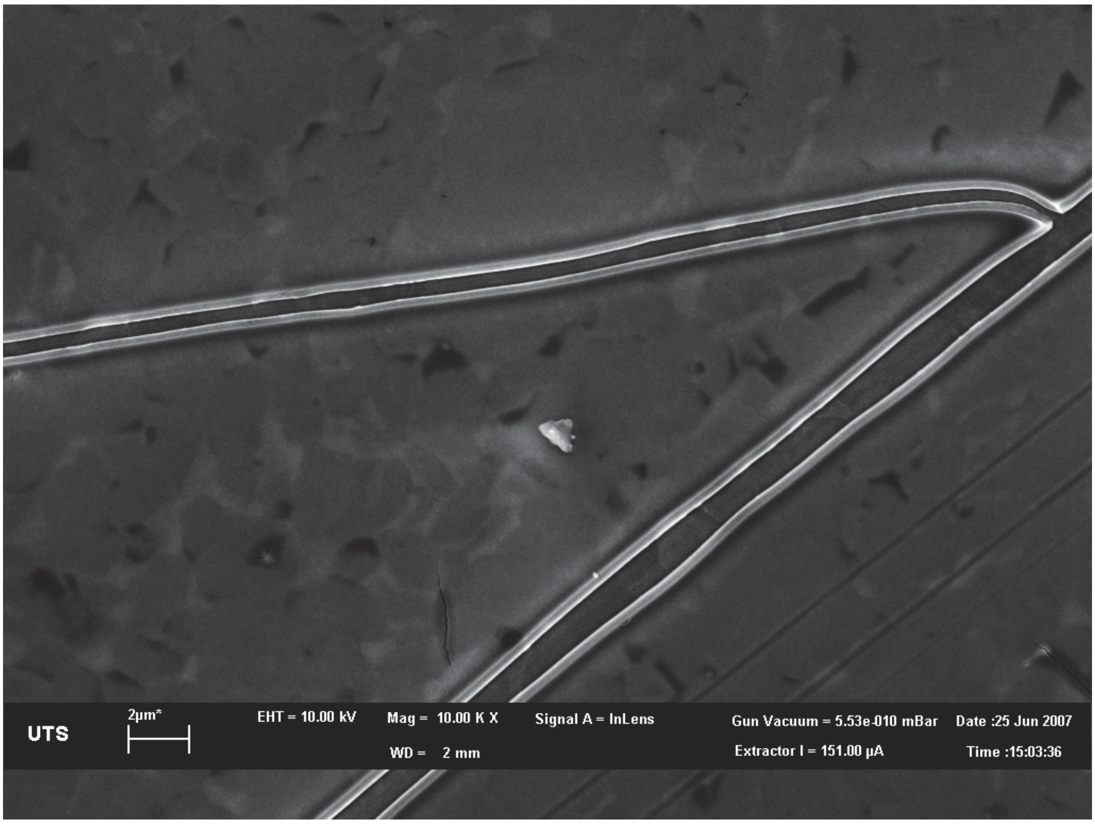

Figure 9.2 *C.P Titanium sample with cracked Zirconia coating.*

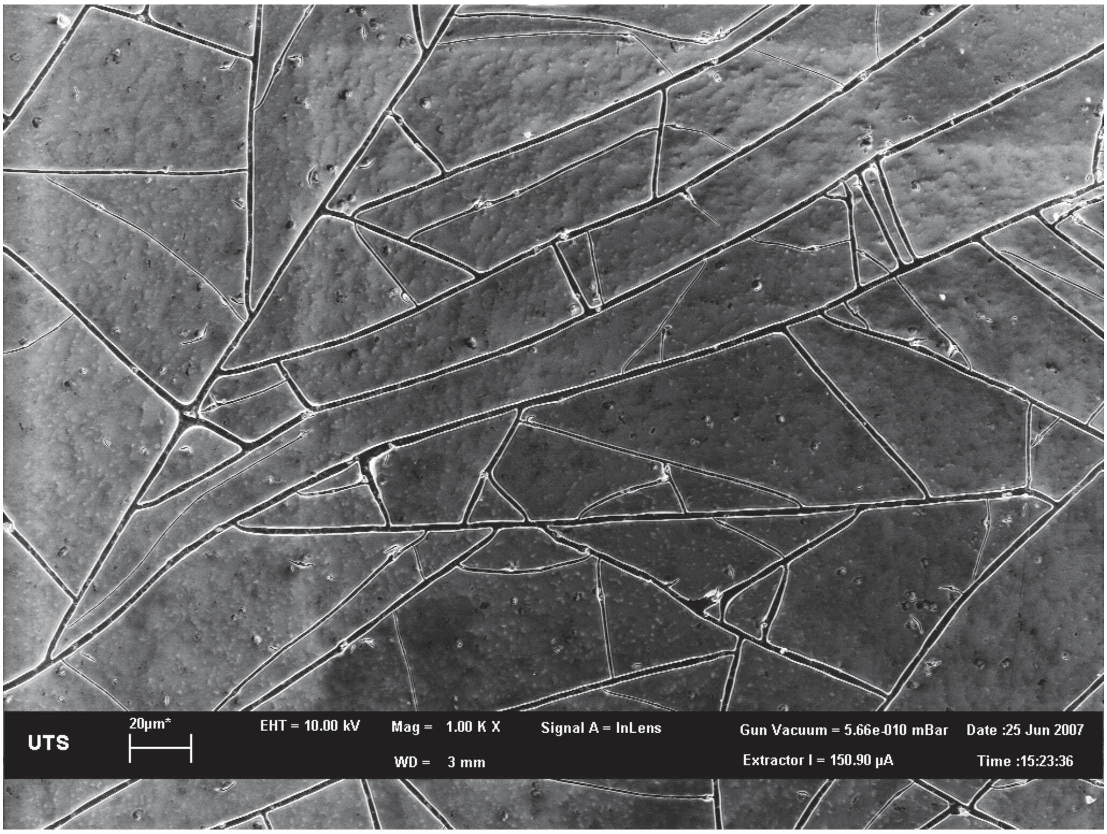

Figure 9.3 *75 volt anodised C.P Titanium sample with cracked Zirconia coating.*

CHAPTER 10 – CONCLUSION

Sol gel coated zirconia has unique properties such as nano scale crystallites and nano scale porosity, when a homogenous zirconia coating is formed through the sol gel process with the titanium metal it offers a solution to the inherent problems of the titanium oxide film, though offering excellent corrosion properties has poor wear characteristics and poor corrosion resistance in highly reducing acid media such as HCl and H_2SO_4 solutions.

Zirconia is a polymorph that occurs in three forms: monoclinic, cubic and tetragonal. Pure zirconia is monoclinic at room temperature. This phase is stable up to 1170°C. Above this temperature it transforms into tetragonal and then into the cubic phase at 2370°C. During cooling, a tetragonal to monoclinic transformation takes place in a temperature range of about 100°C below 1070°C. The phase transformation taking place while cooling is associated with a volume expansion of approximately 3 *to* 4%. Nanometre thick sol-gel zirconia films crystallise directly into the tetragonal/cubic phases without the need to add phase stabilisers into the zirconia film.

The crystallization of the tetragonal zirconia formed at the final sintering temperature of 550°C is due to the excess energy in the thin zirconia film as it anneals at this temperature, reducing the residual stresses inherent in the zirconia thin film coating. This residual stress reduction has resulted in the formation of a metastable tetragonal phase in this work. This tetragonal zirconia was formed on all substrates tested. In pure zirconia, the tetragonal crystal structure exists when grains are below a critical grain size whereas they are monoclinic above the critical grain size. Increasing the heat treatment temperature results in particle or grain growth and hence the tetragonal particles transform into the monoclinic form.

Elastic modulus and hardness are important parameters used by industry with the nano indentation techniques measuring a wide range of materials including thin films. The mechanical properties of the zirconia nano coatings resulting from the nano-indention show zirconia has a young's modulus of 138 GPa, with the hardness value of 4.2GPa for the zirconia sol gel coatings.

The micro adhesion testing yielded a significant number of calculations for the zirconia thin films which were firstly conducted on the cracked zirconia coatings derived from the original zirconia sol gel solution. These highly stressed films had yielded a film thickness of 200 nm and more importantly a cracked zirconia film. This cracking in the film was eliminated by using the modified zirconia solution that yielded 100 nm thick films due to reduced film viscosity and resulting in a less stressed oxide, which showed no cracking even over the edge of the coated titanium samples.

Comparisons of the cracked zirconia films with the modified crack free zirconia solutions showed significant improvement in the adhesion of this crack free film, the 25 and 50 volt anodised C.P. titanium and Ti6Al4V samples with the crack free zirconia show interface toughness values in excess of 1.5 MPa.m$^{1/2}$ indicating that these samples all possess good interface toughness values while the substrates with the cracked zirconia film have toughness values samples of up to 1.1 MPa.m$^{1/2}$ on the best performed samples down to 0.1 MPa.m$^{1/2}$ for the C.P titanium sample.

The testing for both the cracked and crack free zirconia thin films demonstrated that the crack free coatings yielded superior results on every test from the interface energy to the film toughness results. Of interest was the 25 volt and 50 volt results on the C.P. titanium substrate which yielded comparable results with the Ti6Al4V substrate, 25 volt Ti6Al4V substrate and the 50 volt Ti6Al4V substrate in both the interface energy calculations and the interface toughness calculations. Yet the shear stress, film toughness and film fracture energy calculations for the 25 volt and 50 volt result on the C.P. titanium substrate yielded far lower results indicating the improved adhesion properties evident on the Ti6Al4V substrates.

The Ti6Al4V and C.P titanium samples with the 75 volt anodised substrate yielded significantly lower values for all calculations indicating that the increased oxide thickness around 150 nm was inhibiting the performance of the coating due to the failure of the anodised oxide film under micro adhesion testing.

The surface roughness of the anodised layers formed demonstrated that the 50V samples having the greatest surface roughness measurements on both C.P. titanium and Ti6Al4V samples, this is in part due to the actual combined growth method used to anodise the samples with the 50 volt samples having the highest current applied and thus the roughest surfaces. Though the 75 volt surfaces whilst having a higher potential were slowly brought up to this voltage and the resulting current was reduced by the time it formed the same oxide thickness of the 50 volt samples and the increasing voltage slowly increased the anodic oxide formed due to the limited current carrying ability of the rectifier used.

The surface roughness also highlights the effect of the oxide thickness formed during anodisation, with the extra 50nm oxide thickness of the 75 volt anodised samples having a negative effect on the mechanical and adhesion properties of the sol gel coatings both zirconia and hydroxyapatite, despite the enhanced surface wettability of the 75V samples with their high surface energy and a contact angle less than 60°.

Anodising is an technique which forms the oxide film by metal ions moving through the surface oxide to react with the oxide ions in solution and form the metal oxide film and the dissolution of areas of the metal oxide film with the greatest exposure to the anodising solution. So what is occurring is a flattening out of the metal oxide film formed with the high spots removed, hence the improved contact angles and also lower surface roughness figures. This process though is a balancing act though as rapid film formation through high voltages (above 150V) and short anodising times will produce rough porous oxide films that result from the breakdown of the oxide layer as in spark anodising and controlled low voltages over a longer time period will result in a more homogeneous smoother surface oxide film formed.

The hydroxyapatite sol gel coatings although yielding lower mechanical properties than the zirconia coatings this is in part due to the nature of the hydroxyapatite coatings themselves having a more brittle nature, the hydroxyapatite coating demonstrated improved adhesion on the anodised 25 volt and 50 volt substrates of both C.P titanium and the Ti6Al4V. With the 75 volt anodised samples of C.P titanium and the Ti6Al4V showing reduced adhesion properties this demonstrates in part the brittle nature of the titanium oxide formed at 150nm it is substantially thicker than the 25 volt and 50 volt samples at 50 and 75 nm respectively so while the 75 volt sample demonstrated the lowest contact values this was not enough to improve the adhesion of the hydroxyapatite on this oxide as the anodised titanium oxide appeared to fail in the micro adhesion testing leading to large delamination areas of the hydroxyapatite coating.

There was no sign of calcium oxide or calcium titanate in the XRD samples on any of the original, anodised or C.P Titanium and Ti6Al4V substrates with the diffractograms consistent for all titanium samples showing the existence of the hydroxyapatite coating.

The surface roughness of the anodised titanium samples tested in the Saos and Mg63 cell tests was 0.026 µm to 0.028 µm and for the titanium samples 0.005 µm to 0.006 µm and when compared to other cellular adhesion tests who surface Ra ranged from 0.75 µm to 4.68 µm there is a significant difference in the surface roughness of the samples tested. The increased surface roughness has in previous work found to result in better cell attachment and thus adhesion. So the fact that cells adhered on all the surfaces examined in this study despite the very low surface roughness values indicate that it is the substrates themselves that allowed for osteoblast adhesion in both cell lines.

The number of dead cells present in the Saos and Mg63 PI tests was below the linearity of the standard curve, so the levels of cell death were too low to indicate cytotoxic effects. The adhered cells are also very similar for all of the surfaces tested. It must be noted that the significantly lower surface roughness values should result in extremely low adhesion of the cell lines, further work needs to be undertaken on this surface roughness factor with the anodised substrates to see how enhanced the cellular adhesion is with the increased surface roughness values.

These studies showed that the 25 volt current produces a mainly rutile oxide film, the 50 volt current a mixed rutile and anatase oxide film, and the 75 volt current again produces a mixed rutile and anatase oxide film where the anatase crystals formed were larger in size with increasing voltage. This composition of the oxide layer is not the critical factor regarding the adhesion of sol gel layers, of greater importance is the thickness of the anodised layer formed with the 50 to 100nm thick oxide films having a beneficial effect on the adhesion of the sol gel coatings but a further increase of 50nm as in the case of the 75 volt anodised samples significantly results in rapidly decreasing adhesion and mechanical properties of the sol gel coatings in micro adhesion testing.

The SIMS of both of the C.P. Titanium and Ti6Al4V and anodised samples demonstrated the possibility of a similar degree of diffusion in the zirconia sol gel coatings. whilst allowing similar diffusion of the elements of calcium and phosphorus in the case of the hydroxyapatite coating. This diffusion of the sol gel constituent elements would indicate an improved adhesion occurring in the sol gel film as the interlayer existing between the ceramic coatings and the titanium substrates has a degree of bonding between the layers. Further verification of the diffusion processes occurring between the zirconia and hydroxyapatite sol gel coatings and the anodised titanium substrates would be possible by using the FIB technique.

The 25V and 50V anodised titanium layers formed on both the C.P titanium and Ti6Al4V have resulted in the improved adhesion and mechanical properties of both the zirconia and hydroxyapatite sol gel nano coated films and offers a new technique for coating titanium with ceramic sol gel coatings.

BIBLIOGRAPHY

1. Kirk, P.B., et al., *Evaluating sol-gel ceramic thin films for metal implant applications: III. In vitro aging of sol-gel-derived zirconia films on Ti-6Al-4V.* Journal of Biomedical Materials Research (USA), 1999. **48**(4): p. 424-433.
2. Colling, E.W., *The Physical metallurgy of titanium alloys*, in *ASM Series in Metal Processing*, G. H.L., Editor. 1984, American Society for Metals: Cleveland, Metals Park, OH.
3. Denissen, H., et al., *Mechanical Properties of Biomaterials.*, ed. Hastings GW and W. DF. 1980, New York: Wiley.
4. Hench, L.L. *Bioactive Ceramics*. in *Bioceramics: Materials Characteristics Versus In Vivo Behavior.* 1988. Annals N.Y. Acad. Sci.
5. Hench, L.L. and J.K. West, *The Sol Gel Process.* Chem. Rev., 1990. **90**: p. 33-72.
6. Brunette, D.M., et al., *Titanium in Medicine - Material Science, Surface Science, Engineering, Biological Responses and Medical Applications.* 2001, Heidelburg: Springer. 1000 pp.
7. Polmear, J.J., *Titanium Alloys*. Light Alloys. 1981 London Edward Arnold Publications, (Chapter 6).
8. Branemark, P.I., et al., *Osseointegrated titanium fixtures in the treatment of Endentulosness.* Biomaterials, 1983. **4**(25).
9. Aladjem, A., *Anodic Oxidation of Titanium and its Alloys.* Journal of Materials Science, 1973. **8**: p. 688-704.
10. Arsov, L.D. *Growth of Anodic Oxide Films on Titanium Surfaces*. in *Contemporary inorganic Materials: Progress in Ceramics, Metals and Composites: 7th German-Yugoslav Meeting on Engineering Materials Science and Technology*. 1985. Bad Herranalb: Kernforschungsanlage Julich.
11. Andreeva, V. and N. Shishakov, *Z. Fiz. Khim.* 1958. **32**: p. 1671.
12. Andreeva, V. and V. Kazarin. *"Proc. III Internat. Conf. Met. Corrosion - 1966"*. 1969. Mir, Moscow.
13. Young, L., *Anodic Oxide Films.* Academic Press New York, 1961.

14. Franz, D. and H. Goehr, *Ber. Binsenges. Physik. Chem.* 1963. **67**(7): p. 680.
15. Vijh, A., Electrochimica Acta, 1969. **14**: p. 921.
16. Kossyi, G., V. Nivakoyskii, and Y.A. Kolotyrkin, *Zashchita Metallov.* 1969. **5**(2): p. 210.
17. Tomashov, N. and N. Strukov, *Dakl. Akad. Nauk SSSR.* 1963. **152**: p. 1177.
18. Guntherschnize, A. and H. Betz, *Z. Phys.* 1934. **92**: p. 367.
19. Nakata, N. and Y. IIda, *Denki Kagaku Oyobi Kogyo Bulsuri Kagaku.* 1969. **37**(5): p. 366.
20. Krasil'shchikov, A. *"Proc. III Inter. Conf. Met. Corrosion 1966"*. 1968. Mir, Moscow.
21. Hall, C. and N. Hackerman, J. Phys. Chem, 1953. **57**: p. 262.
22. Cover, F. and M. Musselin, Thin Solid Films, 1968. **2**(3): p. 211.
23. Tylecote, R. in *CNRS Symp. No. 122 (1963)*: Paris 1965.
24. Dornelas, W., *Thesis*. 21 December, 1967, University of Paris.
25. Novakovskii, V. and V. Ovcharenko, Zashchita Metallov, 1968. **4**(6): p. 656.
26. Cheseldine, D., J. Electrochem. Soc., 1965. **111**(8): p. 1005.
27. Bogoyavlenskii, A., *Tr. Kaz. Aviats. Inst.* 1966. **90**(3).
28. Tomashov, I. and T. Matveeva, Zashchita Metallov, 1971. **7**(5): p. 272.
29. Cotton, J.B. *"Proc. III Internat. Conf. Met. Corrosion - 1966"*. 1969. Mir, Moscow.
30. Sibert, M.E., J. Electrochem. Soc., 1963(110): p. 65.
31. Cotton, J.B. and A.C. Wood, Trans Inst Chem Engrs, 1963. **41**: p. 354.
32. Cotton, J.B., Chem. Eng. Progr., 1970. **66**: p. 57.
33. Darnault, G., Metallurgie, 1972. **12**: p. 146.
34. Aladjem, A., J. Mater. Sci., 1973. **8**: p. 688.
35. Peksheva, N.P., Zh Prikl Khum, 1979. **52**: p. 2640.
36. Delplancke, J.-L., et al., *Influence of the anodizing procedure on the structure and the properties of titanium oxide films and its effect on copper nucleation.* Electrochimica Acta, 1994. **39**(8-9): p. 1281-1289.
37. Delplancke, J.L. and R. Winand, Electrochimica Acta, 1988. **33**: p. 1539.
38. Marchenour, J.C., J. Gautron, and J.P. Loup, *Met Corros-Ind.* 1977. **52**: p. 83.
39. Marchenour, J.C., J.P. Loup, and J. Masson, *C.R. Hebd Seances Acad. Sci, Ser C.* 1979. **289**: p. 145.

40. Marchenour, J.C., J.P. Loup, and J. Masson, Thin Solid Films, 1980. **66**: p. 357.
41. Arsov, L.D., et al., J. Chim Phys Phys-chum Biol, 1975. **72**: p. 275.
42. Blondeau, G., et al., Thin Solid Films, 1977. **42**: p. 147.
43. Blondeau, G., et al., *Proc Int Vac Congr, 7th.* 1977. **2**: p. 1789.
44. Blondeau, G., et al., J Microsc Spectrosc Electron, 1977. **2**: p. 27.
45. Dalard, F., et al., Surf Technol, 1976. **4**: p. 367.
46. Aladjem, A., G. Brandon, and J. Zahavi, Electrochimica Acta, 1970. **15**: p. 663.
47. Jouve, G., et al., J. Less-Common Met, 1978. **56**: p. 175.
48. Jouve, G. and N.E. Derradji, J Less-Common Met, 1982. **86**: p. 161.
49. Jouve, G. and C. Severac, Titanium Sci technol, Proc Int Conf Titanium 5th, 1984. **4**: p. 2589.
50. Politi, A., G. Jouve, and P. Lacombe, J. Less-Common Met, 1977. **56**: p. 263.
51. Politi, A., et al., J. Microsc Spectrosc Electron, 1978. **3**: p. 513.
52. Yahalom, J. and J. Zahavi, Electrochimica Acta, 1970. **15**: p. 1429.
53. Marino, C.E.B., et al., *On the stability of thin-anodic-oxide films of titanium in acid phosphoric media.* Corrosion Science, 2001. **43**(8): p. 1465-1476.
54. Leitner, K., J.W. Shultze, and U. Stimming, J. Electrochem. Soc., 1986. **135**: p. 1561.
55. Torres, R.M., O.R. Camara, and C.P.D. Pauli, Electrochimica Acta, 1987. **32**: p. 1291.
56. Jung, C. *Surface Treatment of Titanium*. in *The Tribology of Precision*. 2007. Murten, Switzerland.
57. Ishii, M., M. Kaneko, and T. Oda, *Titanium and its Alloys as Key Materials for Corrosion Protection Engineering.* Nippon Steel Technical Report, 2003. **87**: p. 49-56.
58. Lausmaa, J., et al., *Multi-technique surface charaterization of oxide films on electropolished and anodically oxidized titanium.* Applied Surface Science, 1990. **45**(3): p. 189-200.
59. Piveteau, L.D., *Titanium in Medicine*, ed. D.M. Brunette, et al. 2001, Berlin: Springer. pp. 267-282.
60. Paterson, M.J. and B. Ben-Nissan, *Multilayer sol-gel zirconia coatings on 316 stainless steel.* Surface and Coatings Technology, 1996. **86-87**(Part 1): p. 153-158.

61. Uhlmann, D.R., G. Teowee, and J. Boulton, *The Future of Sol-Gel Science and Technology.* J. Sol-Gel Sci. Technol., 1997. **8**: p. 1083-1091.
62. Yen, S.-K., *Mechanism of electrolytic ZrO2 coating on commercial pure titanium.* Materials Chemistry and Physics, 2000. **63**(3): p. 256-262.
63. Lowenheim, F.A., ed. *Modern Electroplating*. 3rd ed. 1974, Wiley - Interscience. 801.
64. D. Velten, et al., *Preparation of TiO2 layers on cp-Ti and Ti6Al4V by thermal and anodic oxidation and by sol-gel coating techniques and their characterization.* Journal of Biomedical Materials Research, 2002. **59**: p. 18-28.
65. Arsov, L.D., *Anodic Oxidation of Ti in H_2SO_4 Solution- Nature, Thickness and Refractive Index of Thin Films Obtained.* Journal De Chime Physique ET DE Physico-Chimie Biologique, 1975. **72**(3): p. 275-279.
66. Arsov, L.D., *Dissolution electrochimique des films anodiques du titane dans l'acide sulfurique.* Electrochimica Acta, 1985. **30**(12): p. 1645-1657.
67. Blondeau, G., et al., *On the optical indices of oxide films as a function of their crystallization: Application to anodic TiO2 (anatase).* Thin Solid Films, 1977. **42**(2): p. 147-153.
68. Ask, M., et al., *Microstructure and Morphology of Surface Oxide Films on Ti-6Al-4V.* J. Mater. Res., 1990. **5**(8): p. 1662-1667.
69. Blackwood, D.J. and L.M. Peter, *The influence of growth rate on the properties of anodic oxide films on titanium.* Electrochimica Acta, 1989. **34**(11): p. 1505-1511.
70. Birch, J.R. and T.D. Burleigh, *Oxides formed on Titanium by Polishing, Etching, Anodizing, or Thermal Oxidizing.* Corrosion, 2000. **56**(12): p. 1233-1241.
71. Climent, F. and R. Capellades, *Anodic oxidation of titanium up to 100 V.* Electrochimica Acta, 1988. **33**(3): p. 433-434.
72. Devilliers, D., et al., *Structure and composition of passive titanium oxide films.* Materials Science and Engineering B, 1997. **47**(3): p. 235-243.
73. Goossens, A. and D.D. Macdonald, *Photostimulated Anodic Oxide Film Formation.* Journal of Applied Physics, 1996. **79**(1): p. 157-162.
74. Joseph, J. and A. Gagnaire, *Ellipsometric study of anodic oxide growth: Application to the titanium oxide systems.* Thin Solid Films, 1983. **103**(1-3): p. 257-265.

75. Ohtsuka, T. and N. Nomura, *The dependence of the optical property of Ti anodic oxide film on its growth rate by ellipsometry.* Corrosion Science, 1997. **39**(7): p. 1253-1263.
76. Ohtsuka, T. and T. Otsuki, *The aging of the anodic oxide of titanium during potentiostatic condition by ellipsometry.* Corrosion Science. **In Press, Corrected Proof**.
77. Rolander, U., et al., *Anodic oxide films on titanium.* Ultramicroscopy, 1986. **19**(4): p. 407.
78. Zwilling, V., M. Aucouturier, and E. Darque-Ceretti, *Anodic oxidation of titanium and TA6V alloy in chromic media. An electrochemical approach.* Electrochimica Acta, 1999. **45**(6): p. 921-929.
79. Roest, R. and B. Ben-Nissan. *Surface Modification of Anodized Titanium for Calcium Phosphate Coatings*. in *Proceedings of the Engineering Materials*. 2001. Melbourne 23-26 September 2001.
80. Roest, R., et al., *Tribology and adhesion of zirconia nano-coatings on surface treated titanium.* Transactions - 7th World Biomaterials Congress Transactions - 7th World Biomaterials Congress, 2004: p. 1783.-7th 2004.
81. Roest, R., et al., *Adhesion of Sol-Gel Derived Zirconia Nano-Coatings on Surface Treated Titanium.* Key Engineering Materials. **254-256**: p. 455-458 (2004).
82. Roest, R., A. Milev, and H. Zreiqat, *Sol-Gel Derived Hydroxyapatite Coatings on Anodized Titanium Substrates*, in *XII International Workshop on Sol Gel Science and Technology*. 2003: Sydney. p. 112 2003.
83. Chai, C.S., K.A. Gross, and B. Ben-Nissan, *Critical ageing of hydroxyapatite sol-gel solutions.* Biomaterials, 1998. **19**(24): p. 2291-2296.
84. Ebelman, M., *Untersuchungen Über die Verbindung der Borsaure und Kieselsaure mit Aether.* Ann. Chim. Phys. **1846**(57): p. 319-355.
85. Masuda, Y., K. Matubara, and S. Sakka, *Synthesis of Hydroxyapatite from Metal Alkoxides through Sol-gel Technique.* J Ceram Soc Jpn, 1990. **98**: p. 1255-1266.
86. Ben-Nissan, B., C. Chai, and K.A. Gross. *Effect of Solution Ageing on Sol Gel Hydroxyapatite Coatings.* in *Bioceramics, Vol 10*. 1997. Paris: Elsevier Science, pp 175-178.
87. P. Ducheyne, L.L.H., A. Kagan, M. Martens, A. Burssens and J.C. Miller *The effect of hydroxyapatite impregnation on skeletal bondings of porous

coated implants. Journal of Biomedical Materials Research, 1980. **14**: p. 225-237.

88. Partenfelder, U., A. Engel, and C. Russel, *A Pyrolytic Route for the Formation of Hydroxyapatite/Fluorapatite Solid Solutions.* Journal of Materials Science, 1993. **4**: p. 292-295.
89. Lacout, J.L., J. Assarane, and J.C. Trombe, *Some Reactions between Phospho-Calcium Hydroxyapatite and Titanium Oxide.* C.R. Acad. Sc Serie II, 1984. **298**: p. 173-175.
90. Chai, C. and B. Ben-Nissan, *Bioactive Nanocrystalline Sol-gel Hydroxyapatite Coatings.* J. Mater. Sci: Mater Med., 1999. **10**: p. 465-469.
91. Ali, A.F., P. Mustarelli, and A. Magistris, *Optimal Synthesis of Organo-Phosphate Precursors for Sol-gel preparations.* Journal Am Ceram Soc, 1998. **82**: p. 27-32.
92. Livage, J., et al., *Sol-gel Synthesis of Phosphates.* J Non-Cryst Solids, 1992. **147-148**: p. 18-23.
93. Weng, W. and J.L. Baptista, *Preparation and Characterization of Hydroxyapatite Coatings on Ti6Al4V alloy by a Sol-gel Method.* J Am Ceram Soc, 1999. **82**: p. 27-32.
94. Weng, W. and J.L. Baptista, *Alkoxide route for Preparing Hydroxyapatite and its Coatings.* Biomaterials, 1998. **19**: p. 125-131.
95. Weng, W. and J.L. Baptista, *A New Synthesis of Hydroxyapatite.* J Eur Ceram Soc, 1997. **17**: p. 1151-1156.
96. Liu, D., et al., *Sol-gel Hydroxyapatite Coatings on Stainless Steel Substrates.* Biomaterials, 2002. **23**(3): p. 691-698.
97. Liu, D., T. Troczynski, and W. Tseng, *Water-based Sol-gel Synthesis of Hydroxyapatite: Process Development.* Biomaterials, 2001. **21**(13): p. 1721-1730.
98. Gross, K., et al., *Thin Hydroxyapatite Coatings via Sol-gel Synthesis.* J. Mater. Sci: Mater Med., 1998. **9**: p. 839-843.
99. Ben-Nissan, B., et al., *'P NMR Studies of Diethyl Phosphite Derived Nanocrystalline Hydroxyapatite.* J. Sol-Gel Sci. Tech., 2001. **21**: p. 27-37.
100. Westheimer, F., S. Huang, and F. Covitz, J. Am. Chem. Soc., 1988. **110**: p. 181.
101. Milev, A., *Chemistry, Synthesis and Morphological Stability of Sol-gel Derived Carbonate Substituted Plate-Like Hydroxyapatite. PhD Thesis*, in *Dept of CMFS*. 2003, UTS: Sydney.

102. Xiao-Xiang Wang, et al., *A comparative study of in vitro apatite deposition on heat, H_2O_2 and NaOH-treated titanium surfaces.* Journal of Biomedical Materials Research, 2001. **54**(2): p. 172-178.

103. Jin-Ming Wu, et al., *Low-Temperature Preparation of Anatase and Rutile Layers on Titanium Substrates and Their Ability To Induce in Vitro Apatite Deposition.* Journal of the American Ceramic Society, 2004. **87**(9): p. 1635-1642.

104. Chai, C. and B. Ben-Nissan. *International Ceramic Monographs*. in *Proceedings of International Conference Austceram 94*. 1994.

105. Torpy, K., *Characterisation of sol-gel derived multi-layered coatings on mild steel for high temperature protection applications. PhD Thesis*, in *Dept of CMFS*. 2003, University of Technology: Sydney.

106. Milev, A., G.S.K. Kannangara, and B. Ben-Nissan. *Ligand substitution and complex formation in hydroxyapatite sol-gel system*. in *Bioceramics 14 Proceeding*. 2001. UTS, Sydney. Aust.

107. Mangonon, P.L., *The Principles of Materials Selection for Engineering Design*. 1999, New Jersey: Prentice-Hall, Inc. 824.

108. Lee, J.S., et al., J. Mater. Sci., 1997. **32**: p. 5249.

109. Ju, X.S., P. Huang, and N.P. Xu, J. Shi, Membr. Sci. Technol. (Chinese), 1999. **19**: p. 11.

110. Lee, I.-S., H.-E. Kim, and S.-Y. Kim, *Studies on calcium phosphate coatings.* Surface and Coatings Technology, 2000. **131**(1-3): p. 181-186.

111. *Science and Technology of Zirconia II*. in *International Conference on the Science and Technology of Zirconia*. 1985: The American Ceramic Society.

112. *Science and Technology of Zirconia III*. in *Proceedings of the International Conference Zirconia '88 Advances in Zirconia Science and Technology*. 1988: The American Ceramic Society.

113. Chen, Y. and W. Liu, *Preparation and tribological properties of sol-gel zirconia thin films stabilized with ceria.* Materials Letters, 2002. **55**(6): p. 407-413.

114. Sergo, V., et al., *Grain size influence on residual stresses in alumina/zirconia composites.* Acta Materialia, 1998. **46**(5): p. 1701-1710.

115. Guicciardi, S., et al., *Effects of residual stresses on the fracture properties of non-oxide laminated composites.* Journal of the European Ceramic Society, 2007. **27**(1): p. 351-356.

116. Innocenzi, P.C., et al., *Coatings of Metals by the Sol Gel Dip Coating Method.* J. Eur. Ceramic Soc., 1992. **10**: p. 431-436.

117. Atik, M., J. Zarzycki, and C. R'Kha, *Protection of Ferritic Stainless Steel against Oxidation by Zirconia Coatings.* J. Mater. Sci. Lett., 1994. **13**: p. 266-269.

118. Atik, M. and M.A. Aegerter, *Corrosion Resistant Sol Gel* ZrO_2 *Coatings on Stainless Steel.* J Non-Cryst Solids, 1992. **147-148**: p. 813-819.

119. Izumi, K., et al., *Zirconia Coatings on Stainless Steel Sheets from Organozirconium Compounds.* J Am Ceram Soc, 1989. **72**: p. 1465-1468.

120. Atik, M., et al., *Protection of 316L Stainless Steel by Zirconia Sol Gel Coatings in 15%* H_2SO_4 *Solutions.* J. Mater. Sci. Lett., 1995. **14**: p. 178-181.

121. Filiaggi, M.J., et al., *Evaluating Sol-Gel Ceramic Thin Films for Metal Implant Applications. I. Processing and Structure of Zirconia Films on Ti-6Al-4V.* Journal of Biomedical Materials Research, 1996. **33**(4): p. 225-238.

122. Filiaggi, M.J., R.M. Pilliar, and D. Abdullah, *Evaluating Sol-Gel Ceramic Thin Films for Metal Implant Applications. II. Adhesion and Fatigue Properties of Zirconia Films on Ti-6Al-4V.* Journal of Biomedical Materials Research, 1996. **33**(4): p. 239-256.

123. Jaffe, W.L. and D.F. Scott, *Total Hip Arthroplasty with Hydroxyapatite-Coated Protheses.* The Journal of Bone and Joint Surgery (American Volume), 1996. **78A**(12): p. 1918-1934.

124. Quinson, J.F., et al., *Deformation Capibility and Protective Role of Zirconia Coatings on Stainless Steel.* J. Mater. Sci., 1996. **31**: p. 5179-5184.

125. Anast, M., et al., *Preparation and Characterisation of Sol Gel Derived Zirconia Coatings.* Sci. Tech. Zirconia V, 1993. **33**: p. 259-266.

126. Paterson, M.J., P.J.K. Paterson, and B. Ben-Nissan, *The dependence of structural and mechanical properties on film thickness in sol-gel zirconia films.* J. Mater. Res., 1998. **13**(2): p. 388-395.

127. Paterson, M.J. and B. Ben-Nissan, Surf. & Coat. Technol., 1996. **86-87**: p. 156.

128. Anast, M., et al., J. Mater. Sci. Lett., 1992. **11**: p. 1483.

129. Mehner, A., et al., *Crystallization and residual stress formation of sol-gel-derived zirconia films.* Thin Solid Films, 1997. **308-309**: p. 363-368.

130. Scherer George, W., *Sintering of Sol-Gel Films.* Journal of Sol-Gel Science and Technology, 1997. **8**(1): p. 353-363.

131. Anselme, K., *Osteoblast adhesion on biomaterials.* Biomaterials, 2000. **21**(7): p. 667-681.

132. Anselme, K., et al., *Qualitative and quantitative study of human osteoblast adhesion on materials with various surface roughnesses.* Journal of Biomedical Materials Research, 2000. **49**(2): p. 155-166.

133. John Martin, T., N. Kong Wah, and G.C. Nicholson, *Cell biology of bone.* Bailliere's Clinical Endocrinology and Metabolism, 1988. **2**(1): p. 1-29.

134. Lewis, K., S.M. Valenzuela, and B. Ben-Nissan, *Changes in the Activity of Osteoblast Like Cells with Sol-Gel Derived Hydroxyapatite and Zirconia Nanocoatings.* Key Engineering Materials, 2008. **361-363**: p. 633-636.

135. Zreiqat, H., et al. *Human Bone Derived Cell (HBDC) Behaviour of Sol-Gel Derived Carbonate Hydroxyapatite Coatings on Titanium Alloy Substrates*. in *Key Engineering Materials, Vols. 284-286, Bioceramics 17*.

136. Zreiqat, H., et al., *The effect of surface chemistry modification of titanium alloy on signalling pathways in human osteoblasts.* Biomaterials, 2005. **26**(36): p. 7579-7586.

137. Siebers, M.C., et al., *Integrins as linker proteins between osteoblasts and bone replacing materials. A critical review.* Biomaterials, 2005. **26**(2): p. 137-146.

138. Das, K., S. Bose, and A. Bandyopadhyay, *Surface modifications and cell-materials interactions with anodized Ti.* Acta Biomaterialia, 2007. **3**(4): p. 573-585.

139. Eisenbarth, E., et al., *Interactions between cells and titanium surfaces.* Biomolecular Engineering, 2002. **19**(2-6): p. 243-249.

140. Kim, Y., et al., *Microarray-based expression analysis of human osteoblast-like cell response to anodized titanium surface.* Biotechnology Letters, 2004. **26**(5): p. 399-402.

141. Sul, Y.-T., *The significance of the surface properties of oxidized titanium to the bone response: special emphasis on potential biochemical bonding of oxidized titanium implant.* Biomaterials, 2003. **24**(22): p. 3893-3907.

142. Sul, Y.T., et al., *Oxidized implants and their influence on the bone response.* Journal of Materials Science: Materials in Medicine, 2001. **12**(10 - 12): p. 1025-1031.

143. Sul, Y.-T., et al., *The bone response of oxidized bioactive and non-bioactive titanium implants.* Biomaterials, 2005. **26**(33): p. 6720-6730.

144. Feldman, L.C. and J.W. Mayer, *Fundamentals of Surface and Thin Film Analysis*. 1986, North Holland, New York.

145. Roest, R., et al. *An Investigation Of Sol Gel Coated Zirconia Thin Films On Anodised Titanium Substrate by Secondary Ion Mass Spectometry and Scanning Electron Microscopy*. in *Materials Forum*. 2007: IMEA.

146. Gnaser, H., *Improved quantification in secondary-ion mass spectrometry detecting MCs $^+$ molecular ions.* Journal of Vacuum Science & Technology A: Vacuum, Surfaces, and Films, 1994. **12**(2): p. 452-456.

147. Vieira, M.T., S. Roque, and A.S. Ramos, *The Effect of a Titanium-based Interlayer on the Adhesion of Ceramic Coatings*, in *Adhesion Aspects of Thin Films*, K.L. Mittal, Editor. 2001. p. 171-180.

148. Shane, M. and M.L. Mecartney, *Sol-gel synthesis of zirconia barrier coatings.* Journal of Materials Science, 1990. **25**(3): p. 1537-1544.

149. Cheng, K., et al., *The adhesion strength and residual stress of colloidal-sol gel derived [beta]-Tricalcium-Phosphate/Fluoridated-Hydroxyapatite biphasic coatings.* Thin Solid Films, 2008. **516**(10): p. 3251-3255.

150. Gastaldi, D., P. Vena, and R. Contro, *Hybrid microstructural finite element modeling for intergranular fracture in ceramic composites and coated systems.* Computational Materials Science. **In Press, Corrected Proof**.

151. Kang, K.J., et al., *A method for in situ measurement of the residual stress in thin films by using the focused ion beam.* Thin Solid Films, 2003. **443**(1-2): p. 71-77.

152. Fujishima, A. and K. Honda, *Electrochemical Photolysis of Water at a Semiconductor Electrode.* Nature, 1972. **238**: p. 37.

153. Liang, B., et al. *Bone-bonding Ability of Anodic Oxidized Titanium*. in *Bioceramics 15 - Key Engineering Materials Vols. 240-242*. 2003. Sydney, Australia: Trans Tech Publications.

154. Ohtsuka, T., M. Masuda, and N. Sato, J. Electrochem. Soc., 1985. **132**(4): p. 787-792.

155. Cotton, J.B., *The Metallurgist and Material Technologies.* 1975(July): p. 350.

156. Ehrhart, G., et al., *Structural and optical properties of n-propoxide sol-gel derived ZrO2 thin films.* Thin Solid Films, 2006. **496**(2): p. 227-233.

157. Kendall, K., *Molecular Adhesion and Its Applications*. 2001, New York: Kluwer Academic / Plenum Publishers.

158. William D. Callister, J., *Materials Science and Engineering*. 3 ed. 1994, New York: John Wiley and Sons.

159. Lee, L.-H., *Fundamentals of Adhesion*. 1991, New York: Plenum Press.

160. Veronica Borsari, G.G., Milena Fini, Paola Torricelli, Matilde Tschon, Roberto Chiesa, Loris Chiusoli, Armando Salito, Andreas Volpert and Roberto Giardino, *Comparative in vitro study on a ultra-high roughness and dense titanium coating* Biomaterials, 2005. **Volume 26**(24): p. 4948-4955.

161. Poulingue, M., M. Ignat, and J. Dijon, *The effects of particle pollution on the mechanical behaviour of multilayered systems.* Thin Solid Films, 1999. **348**(1-2): p. 215-221.

162. Latella, B.A., et al., *Enhanced adhesion of atomic layer deposited titania on polycarbonate substrates.* Thin Solid Films, 2007. **515**(5): p. 3138-3145.

163. Sachse, W., K.Y. Kim, and H.D. Conway, *Determination of the Bond Strength of a Metal Coating on a Substrate.* Mater. Res. Soc. Symp. Proc., 1989. **153**: p. 249-259.

164. Valli, J., *A Review of Adhesion Test Methods for Thin Hard Coatings.* J. Vac. Sci. Technol., 1986. **A4**: p. 3007-3014.

165. Rickerby, D.S., *A Review of the Methods for the Measurement of Coating-Substrate Adhesion.* Surface and Coatings Technology, 1988. **36**: p. 541-557.

166. Mittal, K.L., *Adhesion Measurement of Thin Films.* Electro-component Sci. Technol., 1976. **3**: p. 21-42.

167. Wojciechowski, P.H. and M.S. Mendolia, *Fracture and Cracking Phenomena in Thin Films Adhering to High-Elongation Substrates*, in *Thin Films for Emerging Applications*, M.H. Francombe and J.L. Vossen, Editors. 1991, Academic Press: Boston. p. 271-340.

168. Scafidi, P. and M. Ignat, *Cracking and loss of adhesion of* Si_3N_4 *and* SiO_2*:P films deposited on Al substrates.* J. Adhesion Sci. Technol., 1998. **12**(11): p. 1219-1242.

169. Ignat, M., *Mechanical Response of Multilayers Submitted to In-Situ Experiments.* Key Engineering Materials, 1996. **116-117**: p. 279-290.

170. Hu, M.S. and A.G. Evans, *The Cracking and Decohesion of Thin Films on Ductile Substrates.* Acta Metallurgica, 1989. **37**(3): p. 917-925.

171. Thouless, M.D., et al., Acta metall., 1987. **35**: p. 1333.

172. Hu, M.S., M.D. Thouless, and A.G. Evans, Acta metall., 1988. **36**: p. 1301.

173. Ignat, M., et al., *An experimental approach to the analysis of the adhesion properties of SiC coatings deposited on steel substrates.* Thin Solid Films, 1992. **220**(1-2): p. 271-276.

174. Latella, B.A., B.K. Gan, and H. Li, *Fracture toughness and adhesion of thermally grown titanium oxide on medical grade pure titanium.* Surface and Coatings Technology, 2007. **201**(14): p. 6325-6331.

175. Ignat, M., et al., *Mechanical Behaviour of Submicron Multilayers Submitted to Microtensile Experiments.* Thin Solid Films, 1999. **353**: p. 201-207.

176. Beuth, J.L. and N.W. Klingbeil, *Cracking of Thin Films Bonded to Elastic-Plastic Substrates.* J. Mech.Phys. Solids, 1996. **44**(9): p. 1411-1428.

177. Hu, M.S., M.D. Thouless, and A.G. Evans, *The decohesion of thin films from brittle substrates.* Acta Metallurgica, 1988. **36**(5): p. 1301-1307.

178. Bordet, H., M. Ignat, and M. Dupeux, *Analysis of the Mechanical Response of Film on Substrate Systems Presenting Rough Interfaces.* Thin Solid Films, 1998. **315**: p. 207-213.

179. Field, J.S. and M.V. Swain, *A simple predictive model for sherical indentation.* J. Mater. Res., 1993. **8**(3): p. 297-306.

180. Field, J.S. and M.V. Swain, *Determining the mechanical properties of small volumes of materials from sub micrometer spherical indentations.* J. Mater. Res., 1995. **10**(1): p. 101-112.

181. Suchanek, W. and M. Yoshimura, *Processing and properties of hydroxyapatite-based biomaterials for use as hard tissue replacement implants.* Journal of Materials Research, 1998. **13**(1): p. 94-117.

182. Chen, S.H., L. Liu, and T.C. Wang, *Small scale, grain size and substrate effects in nano-indentation experiment of film-substrate systems.* International Journal of Solids and Structures, 2007. **44**(13): p. 4492-4504.

183. Bhushan, B., *Principles and Applications of Tribology*. 1999, New York: John Wiley & Sons. 1018.

184. Bhushan, B., *Introduction to Tribology*. 2002, New York: John Wiley & Sons. 732.

185. Radchik, V.S., B. Ben-Nissan, and W.H. MÜller, *Theoretical Modeling of Surface Asperity Depression Into an Elastic Foundation Under Static Loading.* Journal of Tribology, 2002. **124**(10): p. 852-855.

186. Radchik, V.S., B. Ben-Nissan, and W.H. MÜller, *Semi-Graphical Methods for the Calculation of Real Areas of Loaded Contact by Means of the Abbott-Firestone Bearing Curve.* Journal of Tribology, 2002. **124**(1): p. 223-226.

187. Critchlow, G.W. and D.M. Brewis, *Review of surface pretreatments for titanium alloys.* International Journal of Adhesion and Adhesives, 1995. **15**(3): p. 161-172.

188. Mason, R.D., D.A. Lind, and W.G. Marchal, *Statistics: an Introduction* 1998: Thomson Brooks/Cole.

APPENDIX

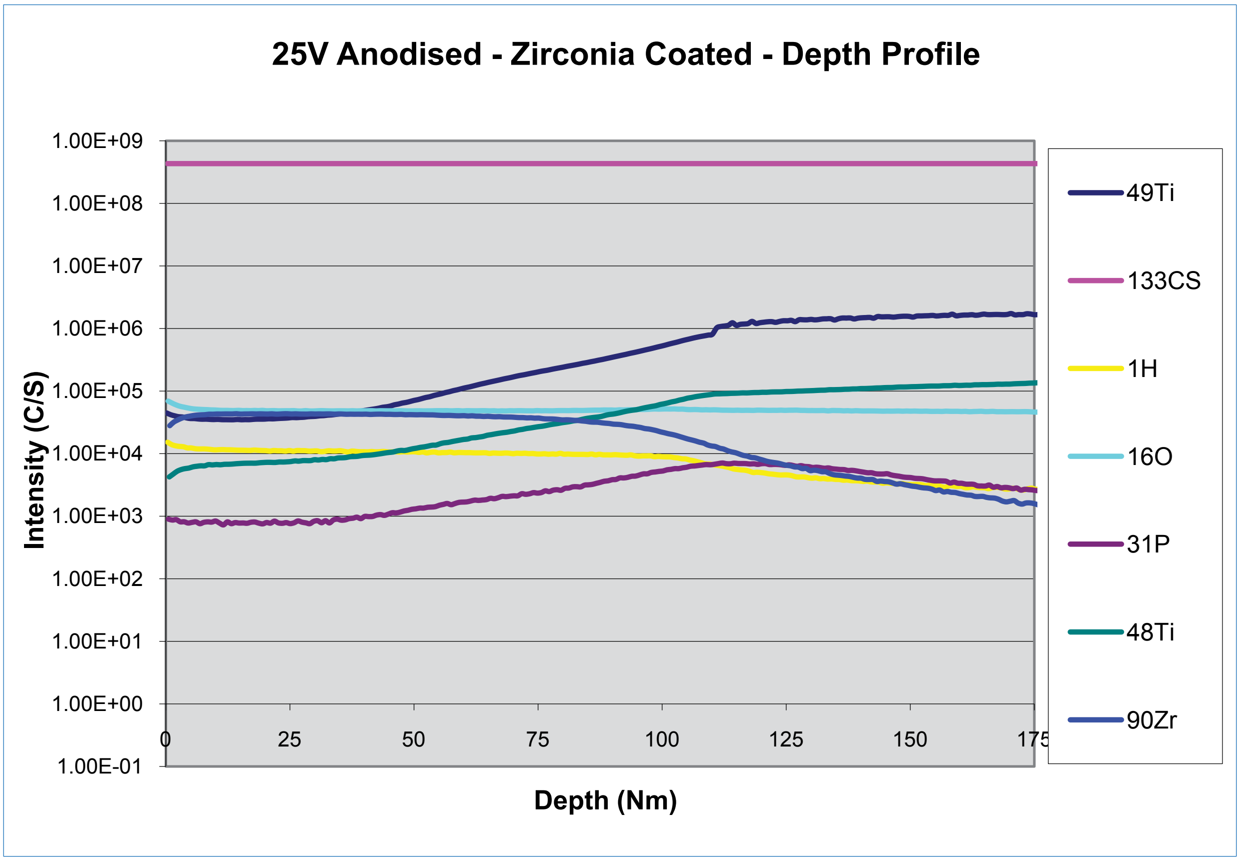

APPENDIX–1 *25 VOLT ANODISED C.P. TITANIUM ZIRCONIA COATED DEPTH PROFILE.*

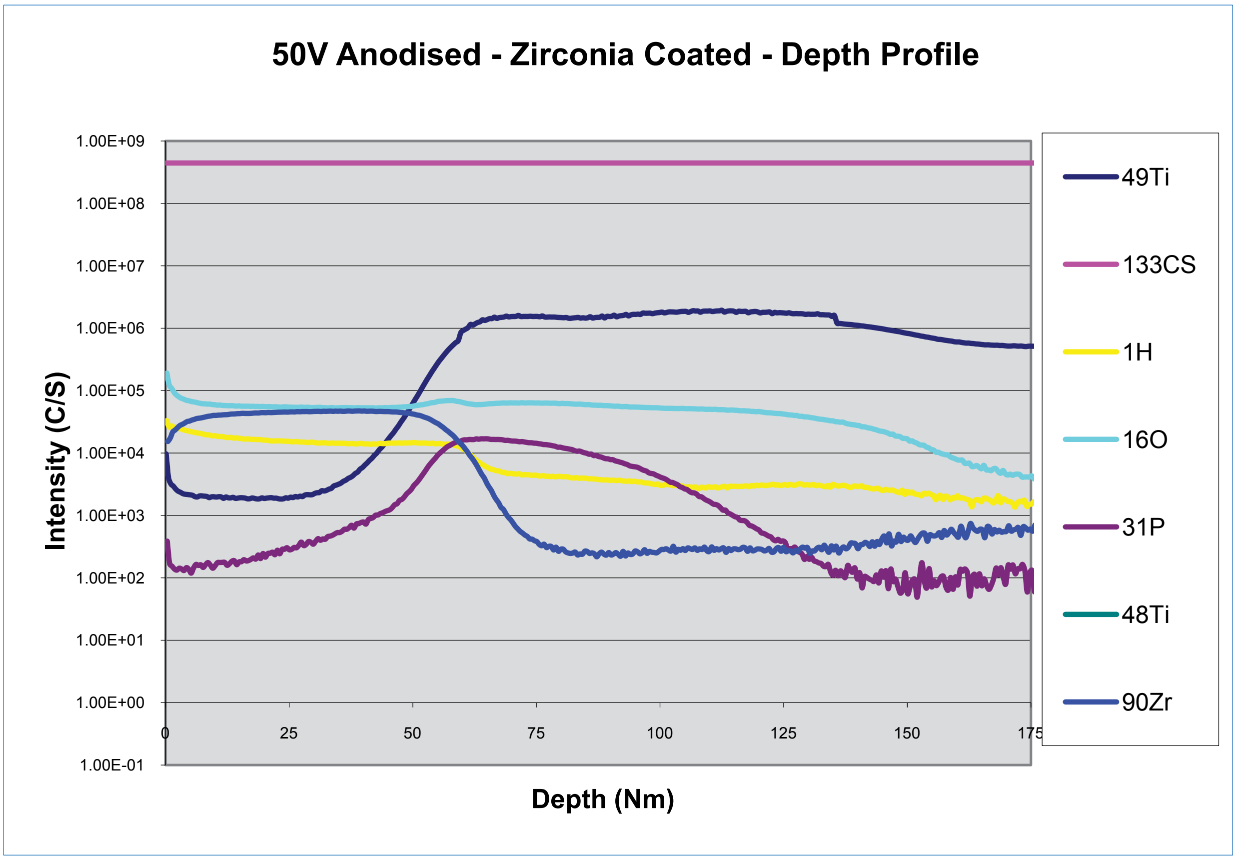

Appendix-2 *50 Volt anodised C.P. Titanium zirconia coated depth profile.*

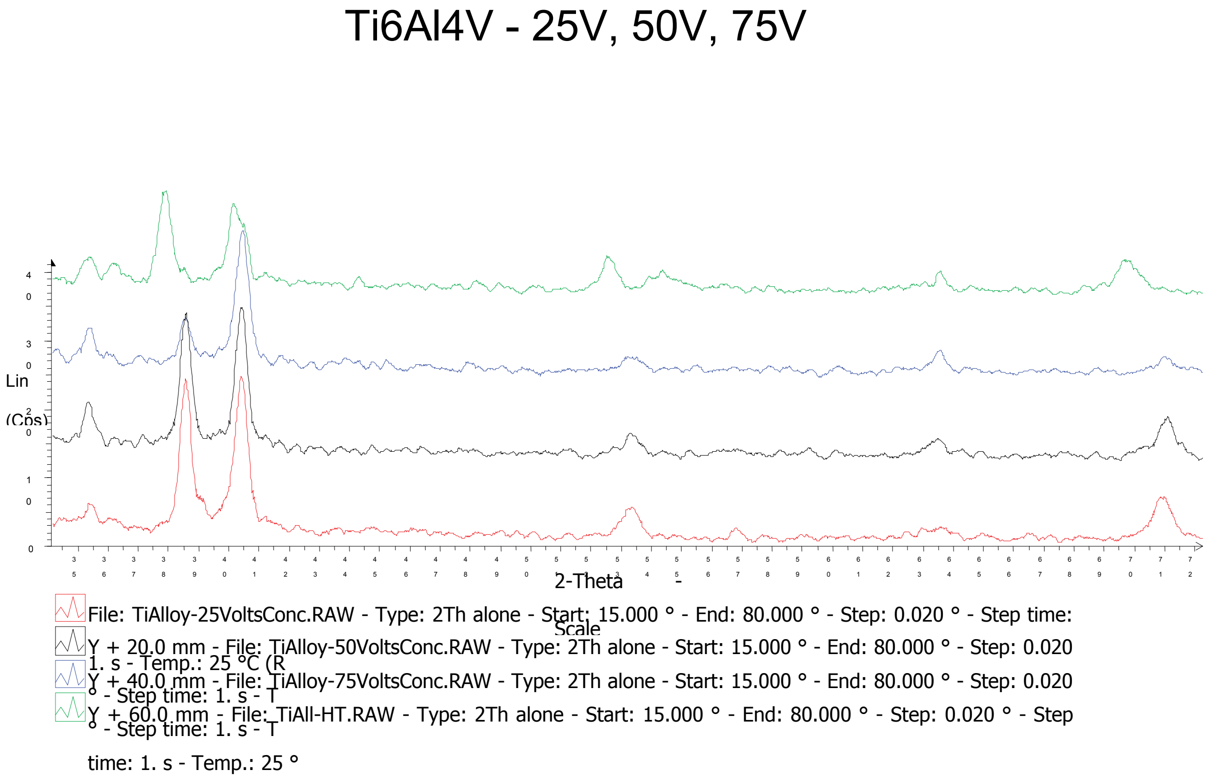

APPENDIX-3 TI6AL4V- XRD DIFFRACTOGRAM OF ANODISED SAMPLES INVOLVING 25, 50, 75 VOLT PLUS TI6AL4V SAMPLE.

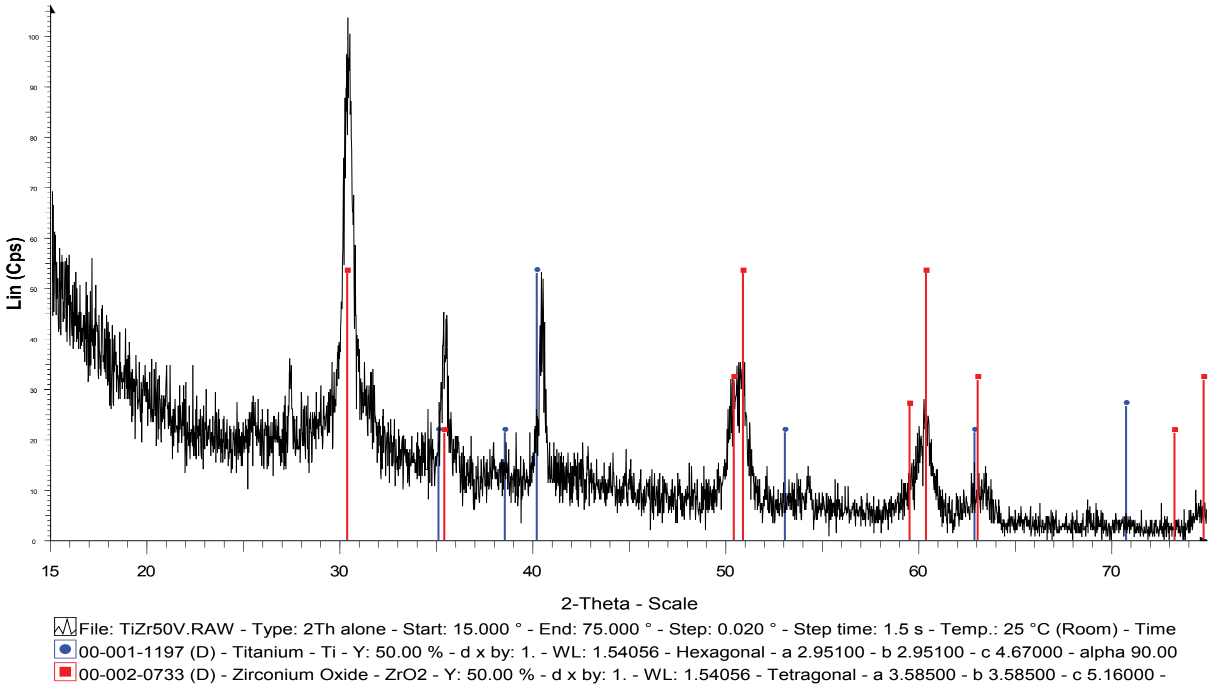

Appendix-4 *Ti6Al4V - XRD Diffractogram of 50V anodised sample with Zirconia Coating.*

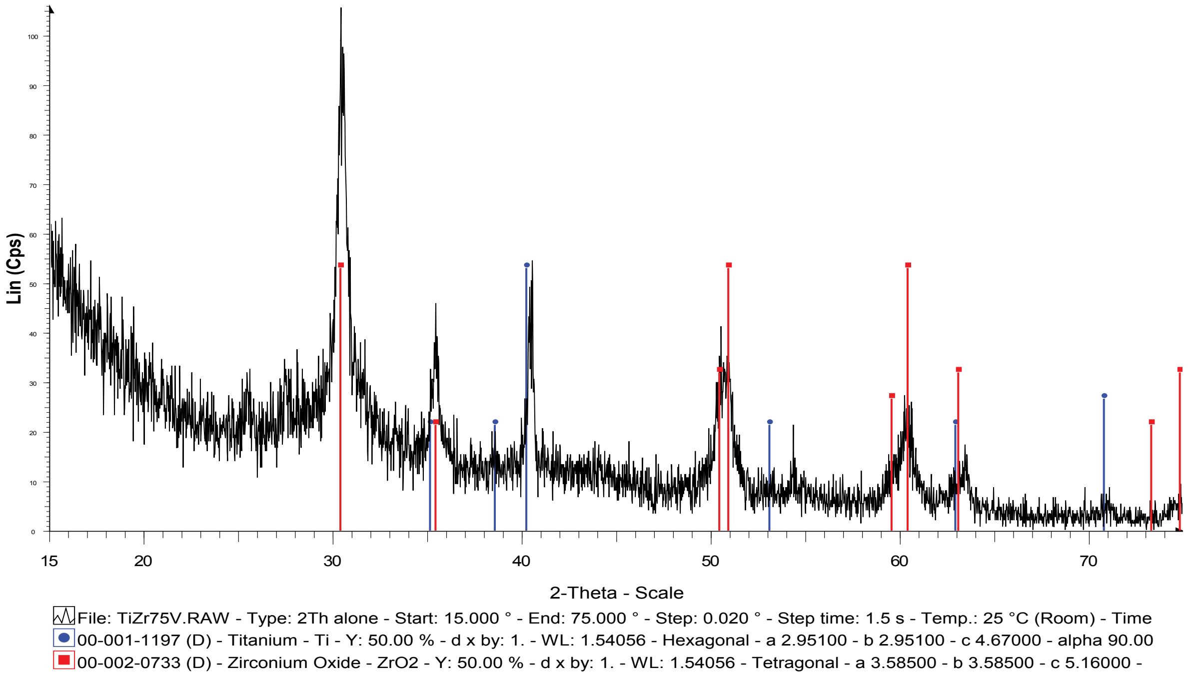

Appendix-5 *Ti6Al4V - XRD Diffractogram of 75V anodised sample with Zirconia Coating.*

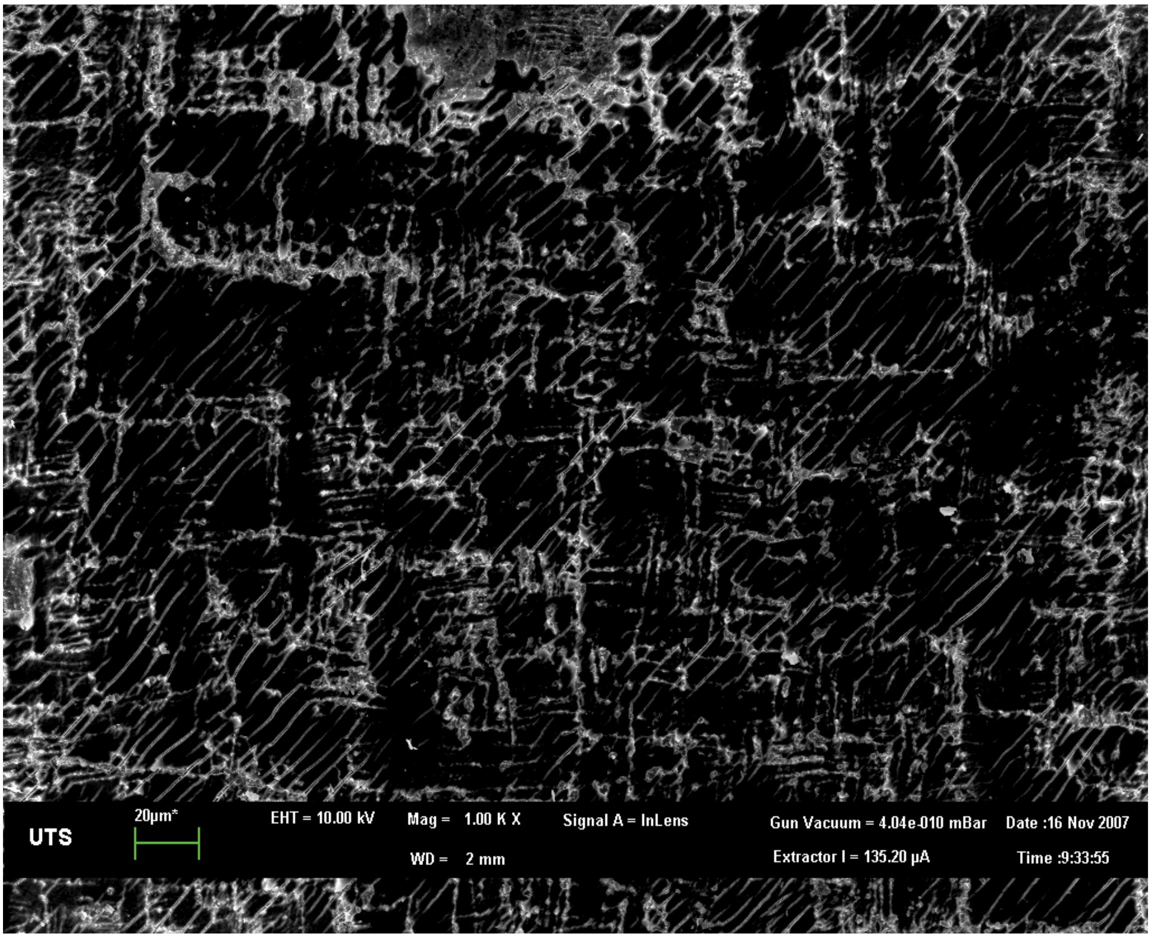

Appendix-6 *SEM of anodised 25 volt C.P. titanium sample after Micro-Adhesion Testing with Hydroxyapatite Sol Gel Coating 1K magnification.*

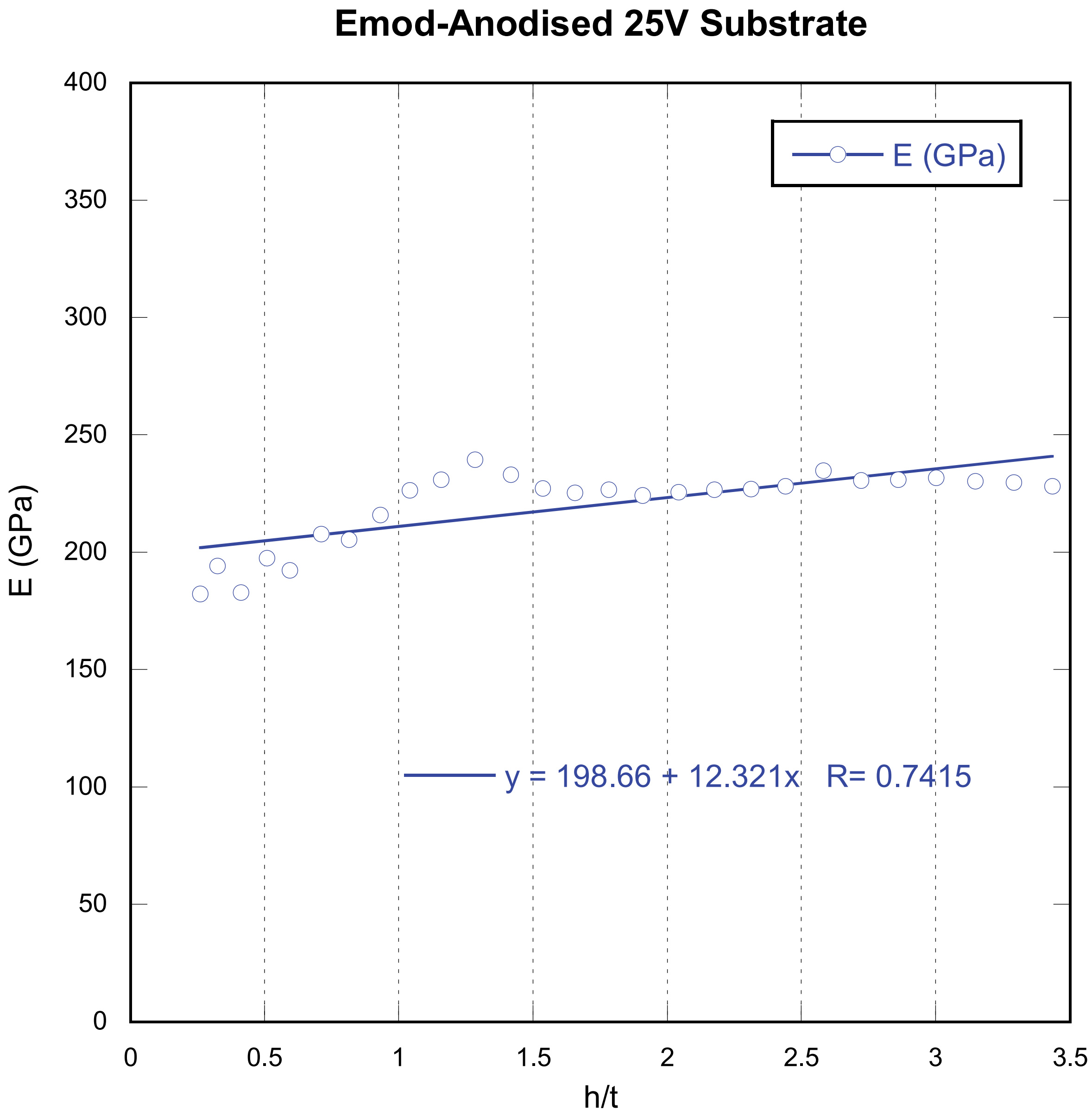

APPENDIX-7 *NANO-INDENTATION OF ANODISED 25 VOLT C.P. TITANIUM SAMPLE SHOWING THE E-MODULUS.*

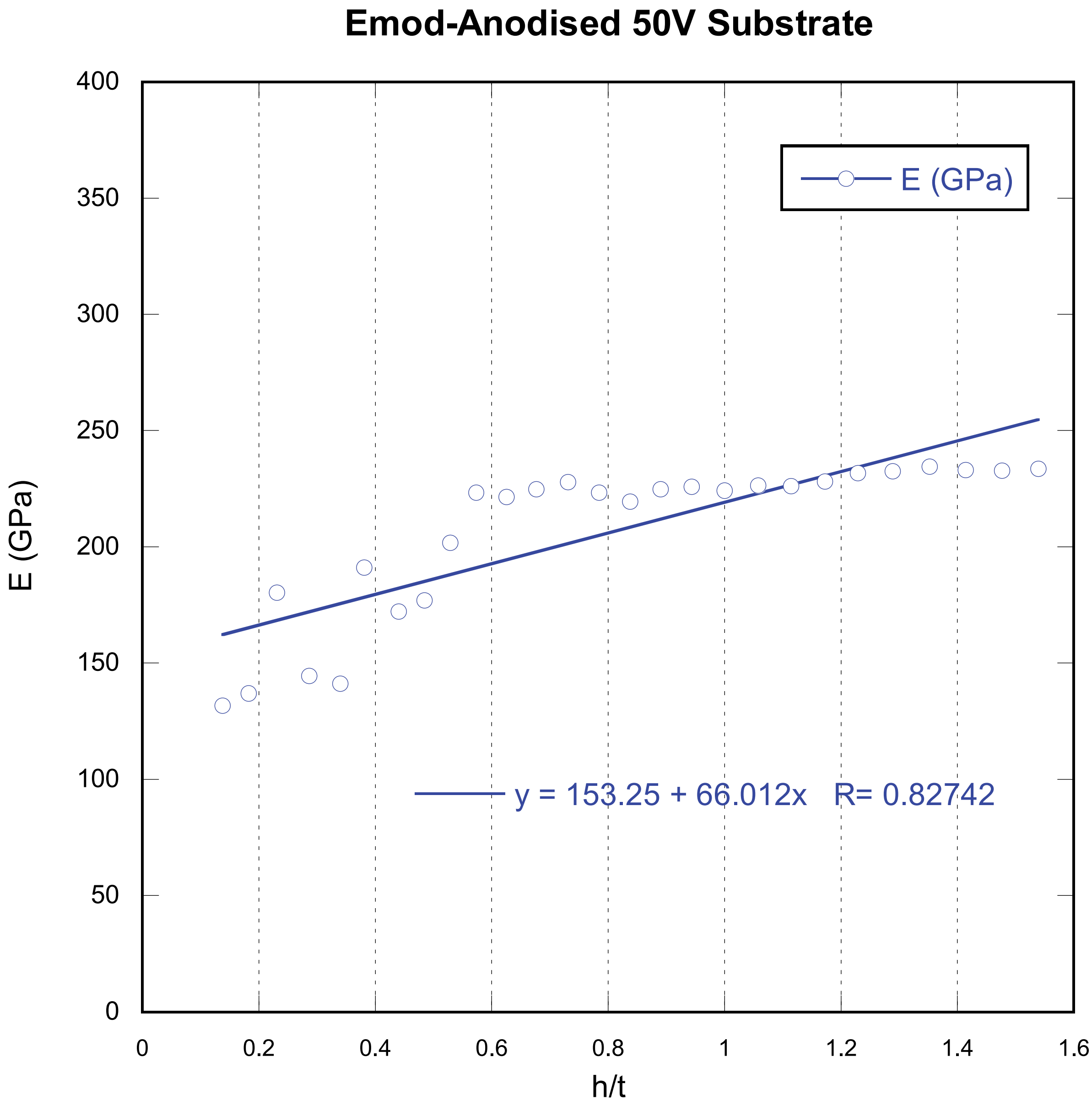

APPENDIX-8 *NANO-INDENTATION OF ANODISED 50 VOLT C.P. TITANIUM SAMPLE SHOWING THE E-MODULUS.*

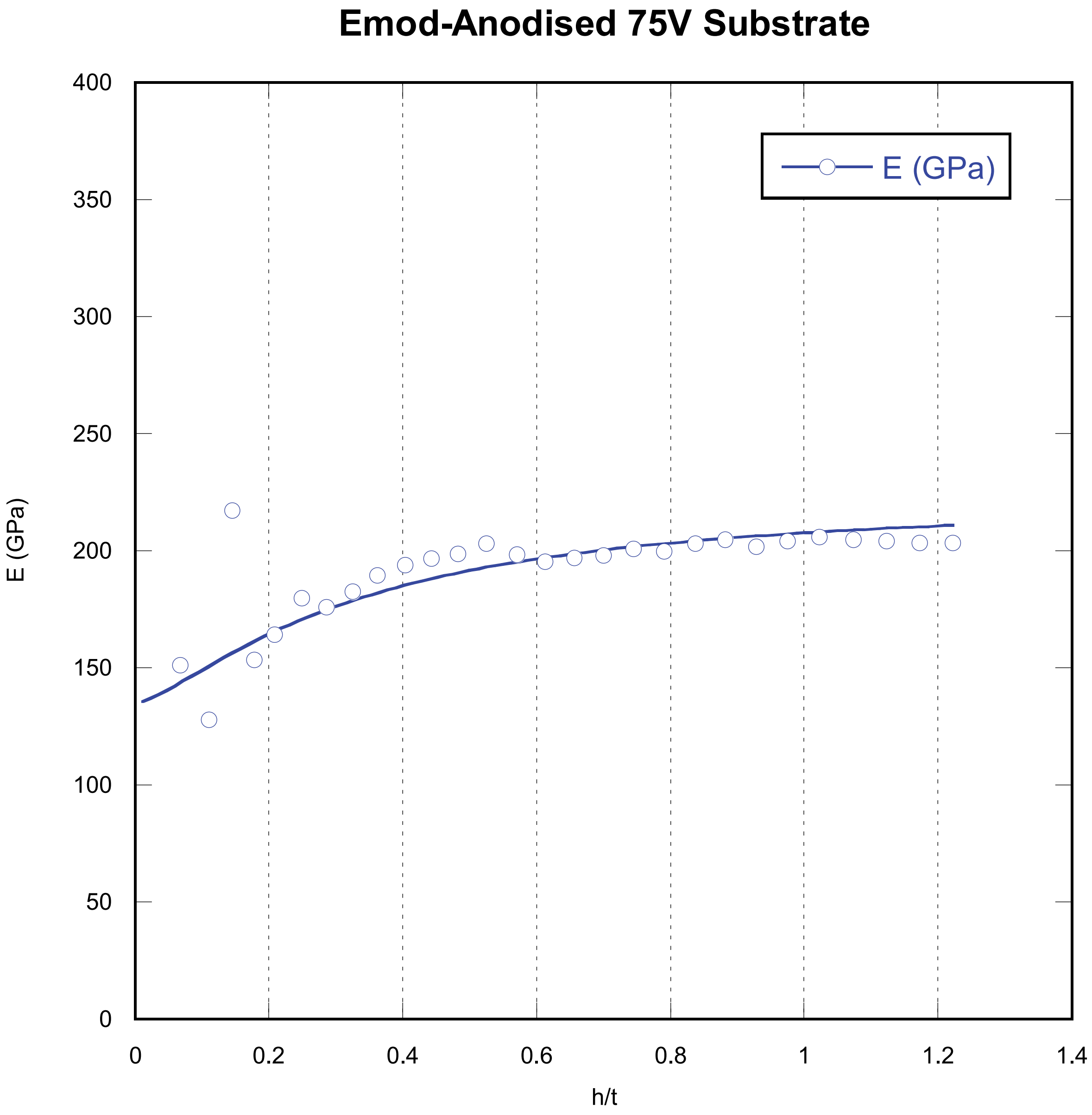

APPENDIX-9 *NANO-INDENTATION OF ANODISED 75 VOLT C.P. TITANIUM SAMPLE SHOWING THE E-MODULUS.*

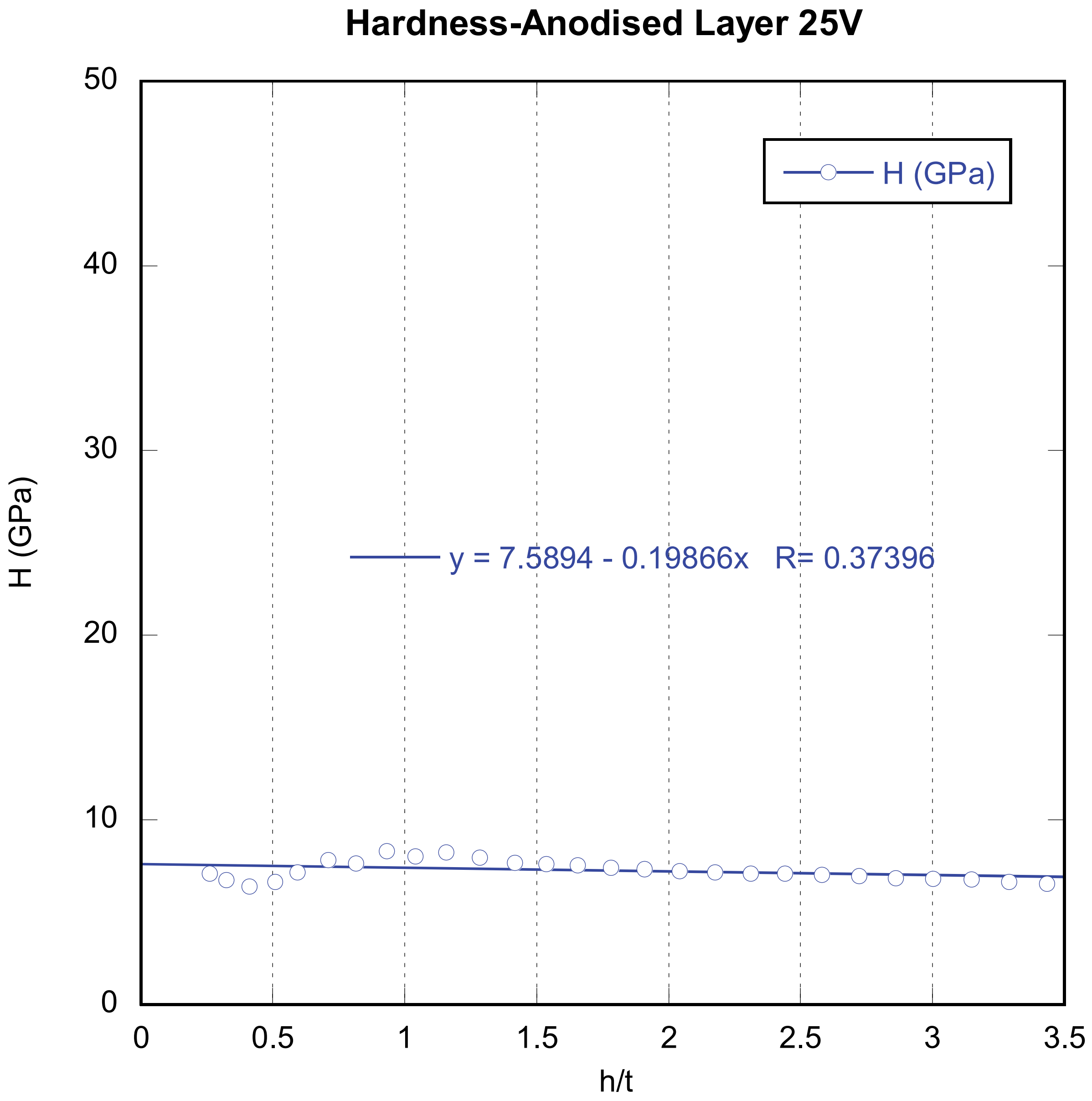

Appendix-10 *Nano-Indentation of anodised 25 volt C.P. titanium sample showing the Hardness Value.*

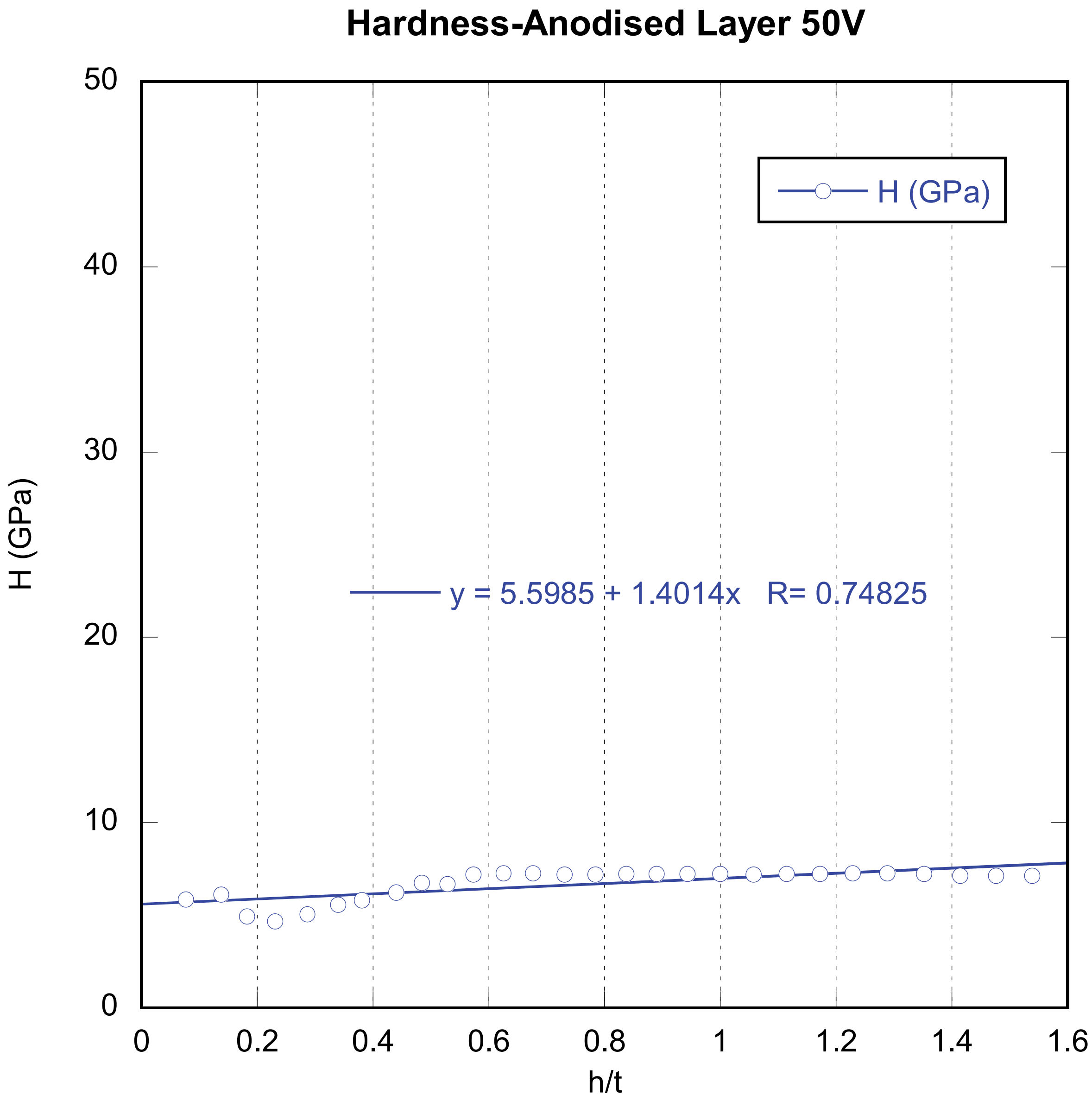

Appendix-11 *Nano-Indentation of anodised 50 volt C.P. titanium sample showing the Hardness Value.*

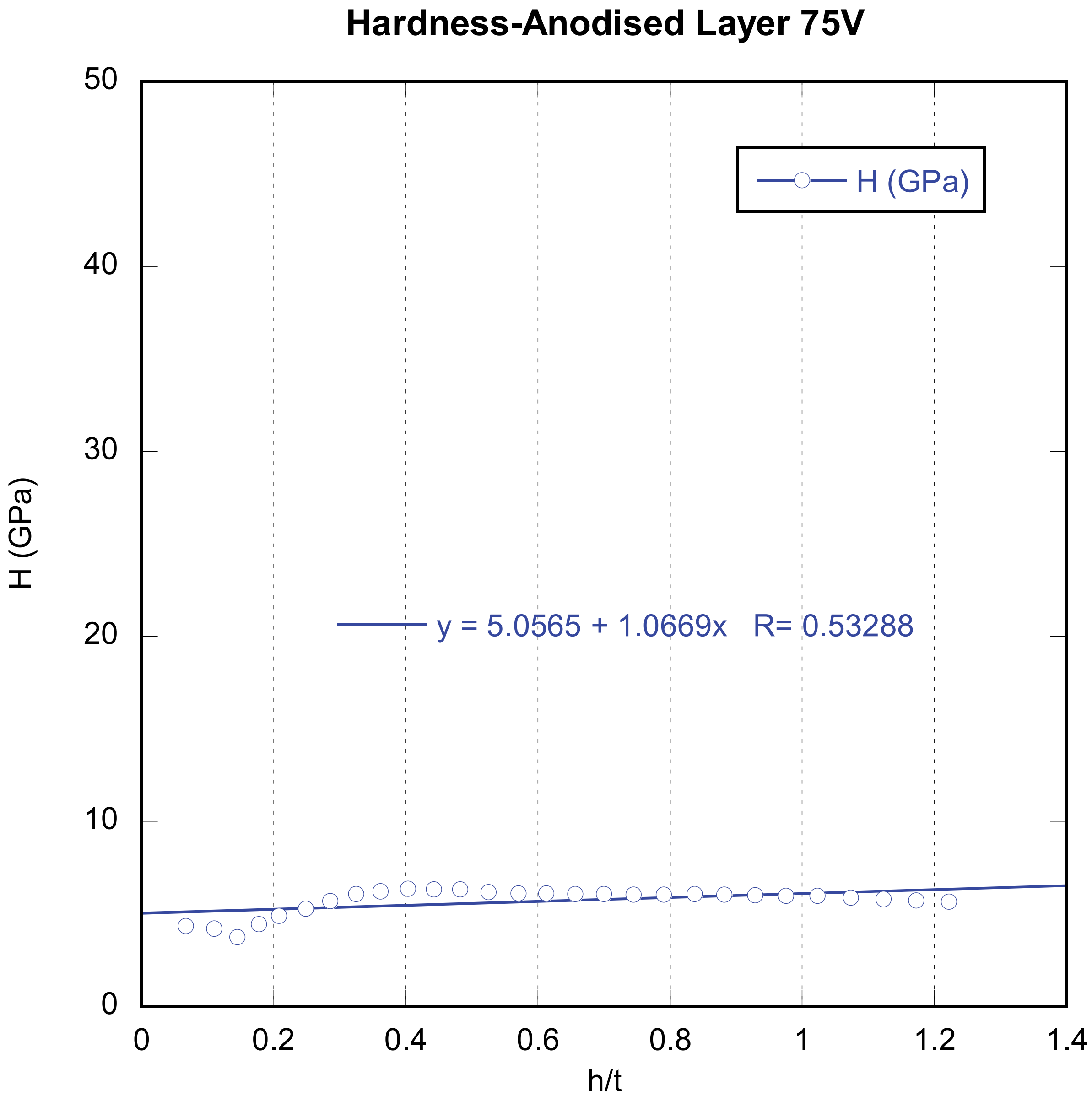

APPENDIX-12 *NANO-INDENTATION OF ANODISED 75 VOLT C.P. TITANIUM SAMPLE SHOWING THE HARDNESS VALUE.*

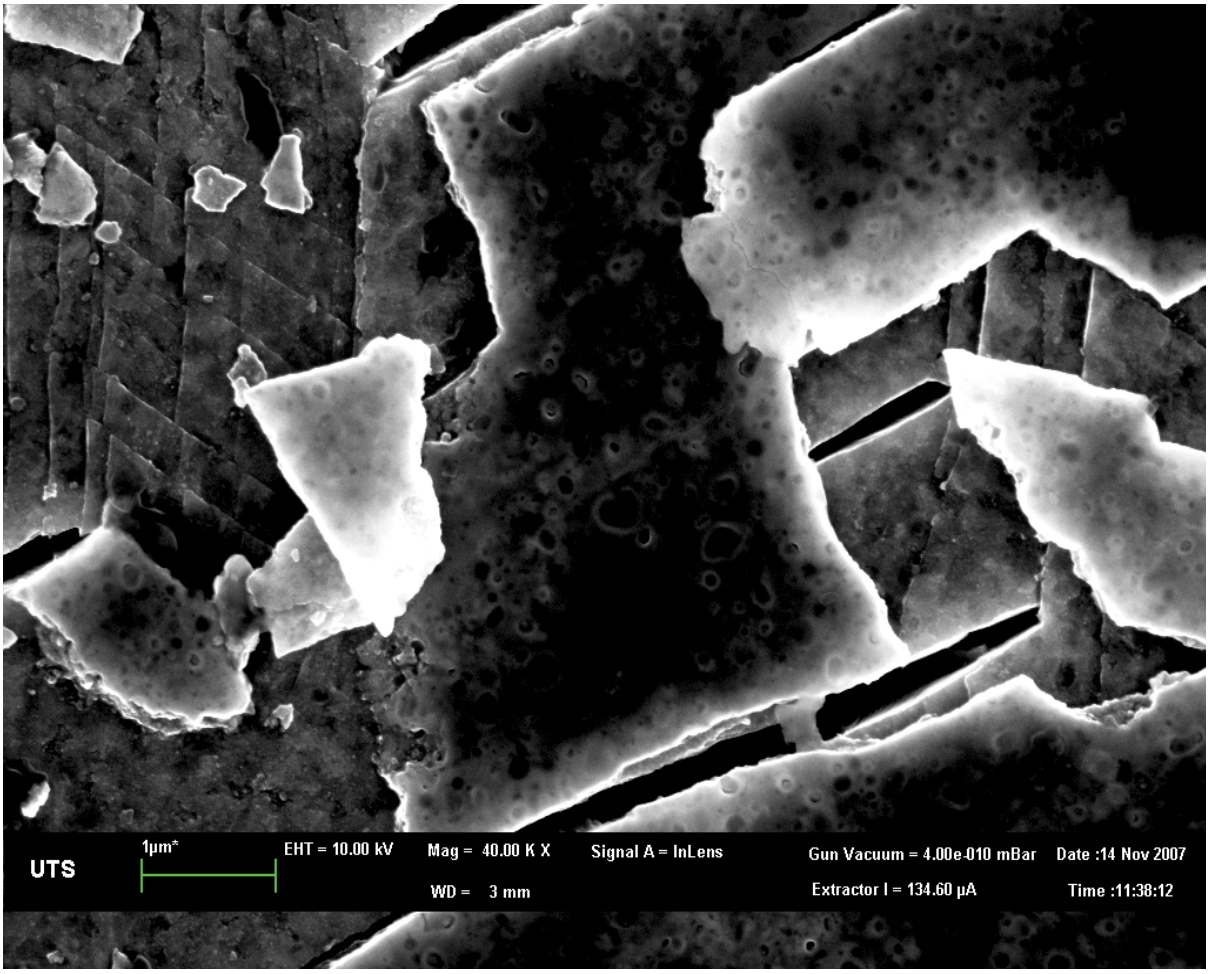

Appendix-13 *SEM of anodised 75 volt Ti6Al4V sample after Micro-Adhesion Testing with Hydroxyapatite Sol Gel Coating 40K magnification.*

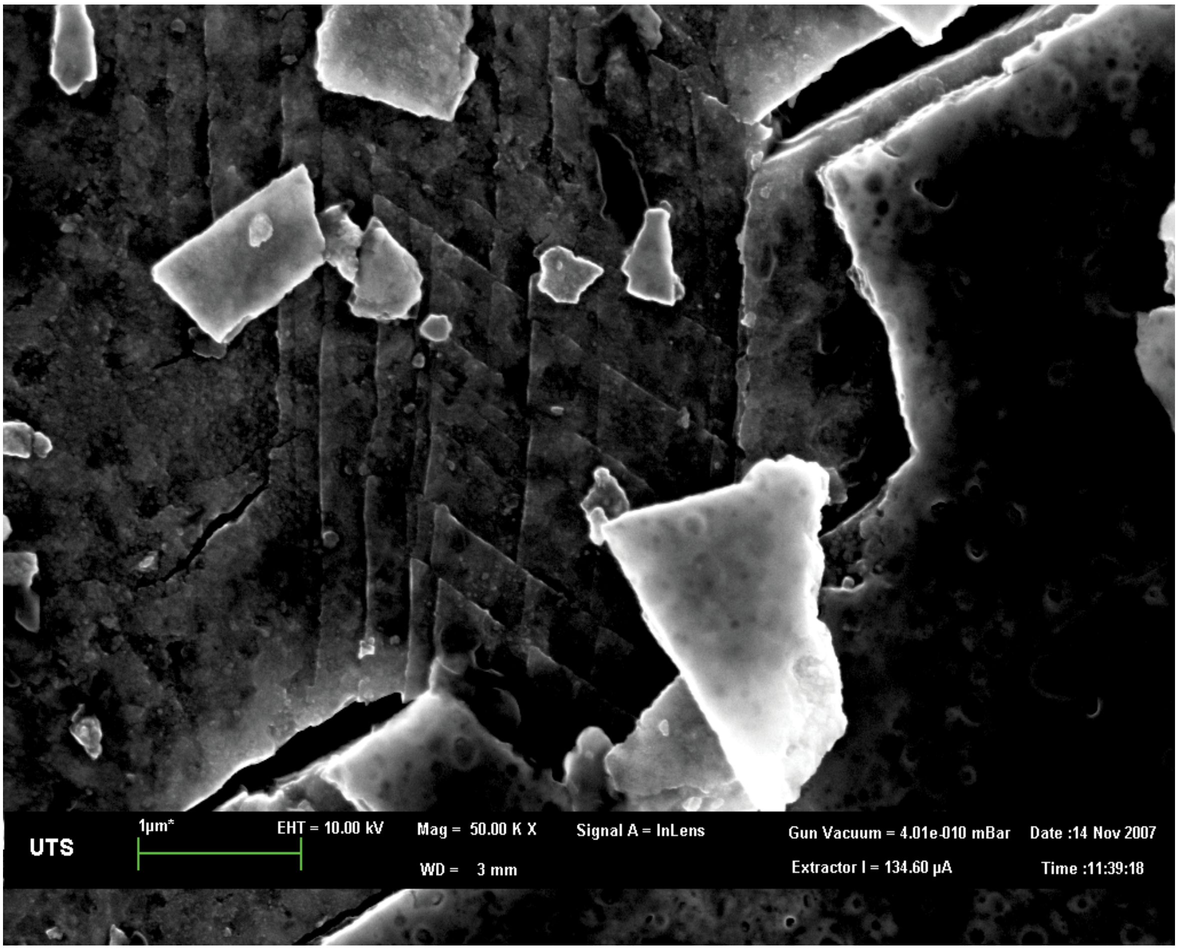

Appendix-14 *SEM of anodised 75 volt Ti6Al4V sample after Micro-Adhesion Testing with Hydroxyapatite Sol Gel Coating 50K magnification.*

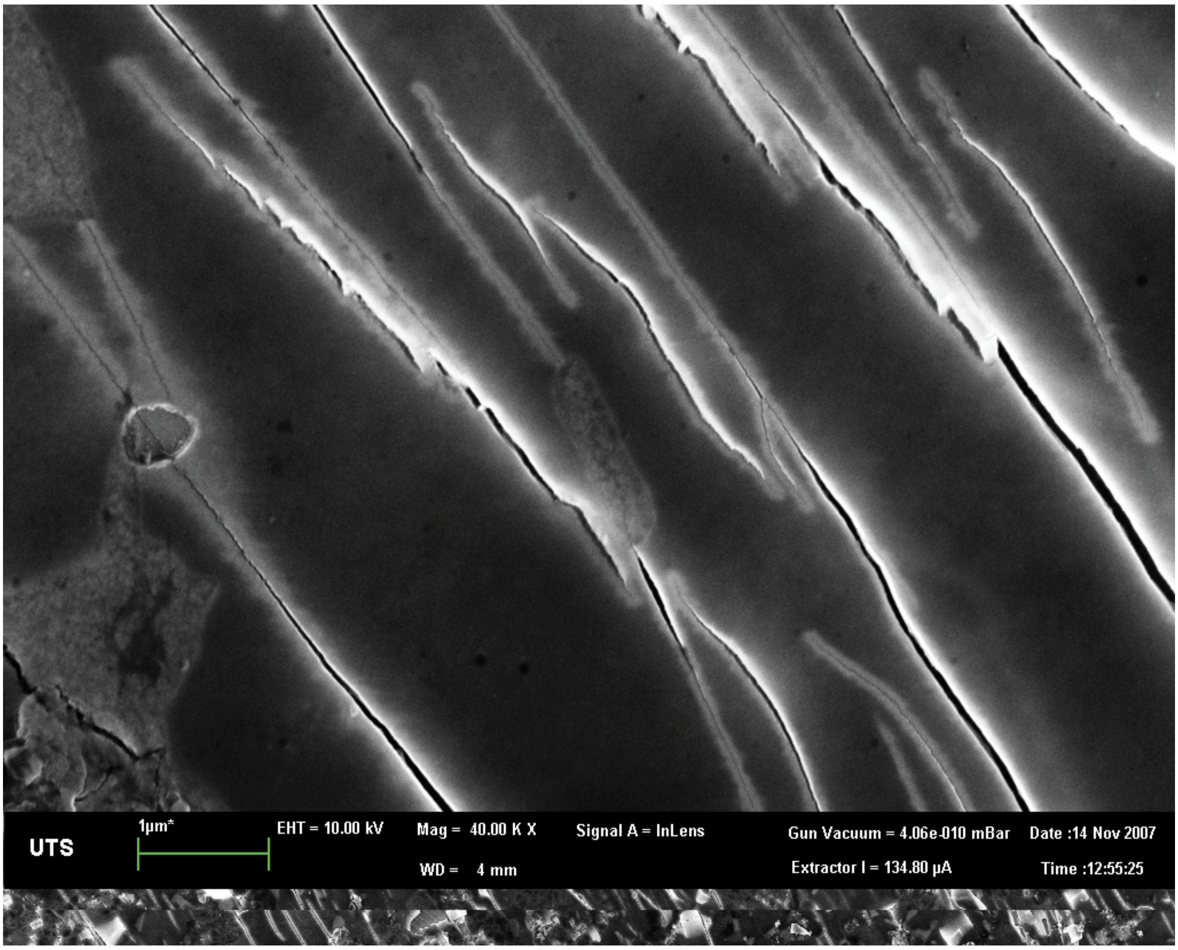

Appendix-15 *SEM of anodised 50 ti6Al4V sample after Micro-Adhesion Testing with Hydroxyapatite Sol Gel Coating 40K magnification.*

Sample Name	**Initial Cracking** (Sec)	**Debonding** (Sec)	**E (Gpa) - Film**	**Thickness** (nm)
ACPTiZr1	210	276	138.25	100
ACPTiZr2	208	270	138.25	100
ACPTi25VZr1	276	470	138.25	100
ACPTi25VZr2	274	460	138.25	100
ACPTi50VZr1	254	410	138.25	100
ACPTi50VZr2	246	406	138.25	100
ACPTi75VZr1	200	240	138.25	100
ACPTi75VZr2	202	240	138.25	100
ATiZr1	360	418	138.25	100
ATiZr2	368	424	138.25	100
ATi25VZr1	400	420	138.25	100
ATi25VZr2	400	418	138.25	100
ATi50VZr1	380	406	138.25	100
ATi50VZr2	372	398	138.25	100
ATi75VZr1	230	260	138.25	100
ATi75VZr2	242	280	138.25	100
CPTi25V1	316	476	135	100
CPTi25V2	314	488	135	100
CPTi25V3	322	480	135	100
CPTi50V1	314	402	135	100
CPTi50V2	316	412	135	100
CPTi50V3	308	396	135	100
CPTi75V1	270	388	135	100
CPTi75V2	274	386	135	100
CPTi75V3	278	394	135	100
Ti25V1	444	478	135	100
Ti25V2	458	490	135	100
Ti25V3	450	472	135	100
Ti50V1	392	460	135	100
Ti50V2	388	444	135	100
Ti50V3	390	456	135	100

APPENDIX-16 *MICRO ADHESION RESULTS FROM TESTING AND ENERGY CALCULATIONS*

Sample Name	**Initial Cracking** (Sec)	**Debonding** (Sec)	**E (Gpa) - Film**	**Thickness** (nm)
CPTiHAp1	192	272		
CPTiHAp2	208	346	24.93	100
CPTiHAp3	210	300	24.93	100
CPTi25VHAp1	212	300	24.93	100
CPTi25VHAp2	214	304	24.93	100
CPTi25VHAp3	192	238	24.93	100
CPTi50VHAp1	218	288	24.93	100
CPTi50VHAp2	206	246	24.93	100
CPTi50VHAp3	200	252	24.93	100
CPTi75VHAp1	188	212	24.93	100
CPTi75VHAp2	170	192	24.93	100
CPTi75VHAp3	172	206	24.93	100
TiHAp1	320	400	24.93	100
TiHAp2	310	372	24.93	100
TiHAp3	336	438	24.93	100
Ti25VHAp1	332	444	24.93	100
Ti25VHAp2	340	478	24.93	100
Ti25VHAp3	300	370	24.93	100
Ti50VHAp1	380	458	24.93	100
Ti50VHAp2	312	420	24.93	100
Ti50VHAp3	316	432	24.93	100
Ti75VHAp1	216	316	24.93	100
Ti75VHAp2	210	290	24.93	100
Ti75VHAp3	192	310	24.93	100

Sample Name	**Initial Cracking** (Sec)	**Debonding** (Sec)	**E (Gpa) - Film**	**Thickness** (nm)
CPTiZr1	330	410	138.25	100
CPTiZr2	290	372	138.25	100
CPTiZr3	300	370	138.25	100
CPTi25VZr1	262	340	138.25	100
CPTi25VZr2	240	310	138.25	100
CPTi25VZr3	260	350	138.25	100
CPTi50VZr1	202	258	138.25	100
CPTi50VZr2	240	300	138.25	100
CPTi50VZr3	250	282	138.25	100
CPTi75VZr1	200	240	138.25	100
CPTi75VZr2	210	252	138.25	100
CPTi75VZr3	210	250	138.25	100
TiZr1	376	440	138.25	100
TiZr2	390	410	138.25	100
TiZr3	376	410	138.25	100
Ti25VZr1	386	428	138.25	100
Ti25VZr2	378	438	138.25	100
Ti25VZr3	370	400	138.25	100
Ti50VZr1	280	302	138.25	100
Ti50VZr2	272	324	138.25	100
Ti50VZr3	276	340	138.25	100
Ti75VZr1	210	240	138.25	100
Ti75VZr2	200	242	138.25	100
Ti75VZr3	190	212	138.25	100

Sample Name	Stress Cracking (MPa)	Strain (Debonding)	Dundar's Parameter	g(aD) from Bleuth
ACPTiZr1	468.7819672	0.021784559	0.152884228	1.341
ACPTiZr2	495.8983607	0.025360255	0.152884228	1.341
ACPTi25VZr1	527.1114754	0.066229059	0.152884228	1.341
ACPTi25VZr2	526.5262295	0.065038559	0.152884228	1.341
ACPTi50VZr1	519.5032787	0.05795772	0.152884228	1.341
ACPTi50VZr2	520.4786885	0.057187018	0.152884228	1.341
ACPTi75VZr1	474.4393443	0.018668012	0.152884228	1.341
ACPTi75VZr2	510.3344262	0.016551123	0.152884228	1.341
ATiZr1	979.8234552	0.057747017	0.052651616	1.251
ATiZr2	981.3997478	0.059202017	0.052651616	1.251
ATi25VZr1	988.0201765	0.05814385	0.06913063	1.251
ATi25VZr2	988.0212765	0.057747017	0.06913063	1.251
ATi50VZr1	983.6065574	0.055101517	0.06913063	1.251
ATi50VZr2	982.3455233	0.053381933	0.06913063	1.251
ATi75VZr1	955.8638083	0.0212391	0.06913063	1.251
ATi75VZr2	956.1790668	0.02639785	0.06913063	1.251
CPTi25V1	567.2983607	0.018063542	0.125	1.295
CPTi25V2	565.9327869	0.018585785	0.125	1.295
CPTi25V3	570.4196721	0.018217153	0.125	1.295
CPTi50V1	561.8360656	0.013867834	0.125	1.295
CPTi50V2	562.4213115	0.014382577	0.125	1.295
CPTi50V3	558.1295082	0.013565043	0.125	1.295
CPTi75V1	539.9868852	0.014897714	0.125	1.295
CPTi75V2	542.7180328	0.014833074	0.125	1.295
CPTi75V3	547.7901639	0.015253185	0.125	1.295
Ti25V1	988.0201765	0.0606571	0.040783286	1.25
Ti25V2	990.5422446	0.062905767	0.040783286	1.25
Ti25V3	988.6506936	0.0594666	0.040783286	1.25
Ti50V1	977.3013871	0.056424267	0.040783286	1.25
Ti50V2	976.9861286	0.053117433	0.040783286	1.25
Ti50V3	976.6708701	0.05549835	0.040783286	1.25

Sample Name	Stress Cracking (MPa)	Strain (Debonding)	Dundar's Parameter	g(aD) from Bleuth
Ti75V1	974.779319	0.0474296	0.040783286	1.25
Ti75V2	975.7250946	0.048090933	0.040783286	1.25
Ti75V3	973.8335435	0.043196767	0.040783286	1.25
CPTiZr1	562.2262295	0.013210478	0.152884228	1.341
CPTiZr2	555.5934426	0.010145115	0.152884228	1.341
CPTiZr3	569.6393443	0.012271313	0.152884228	1.341
CPTi25VZr1	552.4721311	0.012391041	0.152884228	1.341
CPTi25VZr2	503.7016393	0.008270405	0.152884228	1.341
CPTi25VZr3	520.0885246	0.008382862	0.152884228	1.341
CPTi50VZr1	495.5081967	0.010855998	0.152884228	1.341
CPTi50VZr2	535.5	0.006026217	0.152884228	1.341
CPTi50VZr3	518.9180328	0.006133743	0.152884228	1.341
CPTi75VZr1	522.2344262	0.005439358	0.152884228	1.341
CPTi75VZr2	494.5327869	0.007056479	0.152884228	1.341
CPTi75VZr3	534.5245902	0.007009535	0.152884228	1.341
TiZr1	974.779319	0.0527206	0.06913063	1.251
TiZr2	977.6166456	0.04610685	0.06913063	1.251
TiZr3	974.779319	0.045974517	0.06913063	1.251
Ti25VZr1	976.6708701	0.050604183	0.06913063	1.251
Ti25VZr2	975.4098361	0.053117433	0.06913063	1.251
Ti25VZr3	973.8335435	0.04372585	0.06913063	1.251
Ti50VZr1	957.1248424	0.02375235	0.06913063	1.251
Ti50VZr2	956.1790668	0.028381933	0.06913063	1.251
Ti50VZr3	957.1248424	0.031159767	0.06913063	1.251
Ti75VZr1	795.0819672	0.008408433	0.06913063	1.251
Ti75VZr2	721.3114754	0.008672933	0.06913063	1.251
Ti75VZr3	664.2496847	0.00620293	0.06913063	1.251
CPTiHAp1				
CPTiHAp2	507.6032787	0.025100258	-0.616254906	0.7672
CPTiHAp3	454.1508197	0.009624469	-0.616254906	0.7672
CPTi25VHAp1	529.647541	0.008700561	-0.616254906	0.7672
CPTi25VHAp2	493.1672131	0.014501266	-0.616254906	0.7672
CPTi25VHAp3	498.2393443	0.012227935	-0.616254906	0.7672

Sample Name	**Stress Cracking (MPa)**	**Strain (Debonding)**	**Dundar's Para**	**g(aD) from Bleuth**
CPTi50VHAp1	544.2786885	0.018575172	-0.616254906	0.7672
CPTi50VHAp2	529.0622951	0.013741492	-0.616254906	0.7672
CPTi50VHAp3	549.3508197	0.016816014	-0.616254906	0.7672
CPTi75VHAp1	523.0147541	0.010892927	-0.616254906	0.7672
CPTi75VHAp2	532.1836066	0.009188818	-0.616254906	0.7672
CPTi75VHAp3	333.5901639	0.005348497	-0.616254906	0.7672
TiHAp1	962.7994956	0.042667683	-0.666153331	0.7461
TiHAp2	961.5384615	0.036715267	-0.666153331	0.7461
TiHAp3	965.9520807	0.051794683	-0.666153331	0.7461
Ti25VHAp1	965.6368222	0.053117433	-0.666153331	0.7461
Ti25VHAp2	967.8436318	0.059863433	-0.666153331	0.7461
Ti25VHAp3	959.6469105	0.036186183	-0.666153331	0.7461
Ti50VHAp1	975.4098361	0.056159767	-0.666153331	0.7461
Ti50VHAp2	962.4842371	0.048355517	-0.666153331	0.7461
Ti50VHAp3	963.1147541	0.051794683	-0.666153331	0.7461
Ti75VHAp1	832.2824716	0.026794683	-0.666153331	0.7461
Ti75VHAp2	810.2143758	0.021768183	-0.666153331	0.7461
Ti75VHAp3	678.7515763	0.026265517	-0.666153331	0.7461

Sample Name	Interface Energy (J/m^2)	Interface Energy Average	STD Dev
ACPTiZr1	3.39078123	3.99301738	0.851690532
ACPTiZr2	4.595253531		
ACPTi25VZr1	31.3400294	30.78174018	0.789540184
ACPTi25VZr2	30.2235		
ACPTi50VZr1	24.00075036	23.6837187	0.448350472
ACPTi50VZr2	23.36668704		
ACPTi75VZr1	2.489994515	2.223646717	0.376672668
ACPTi75VZr2	1.957298919		
ATiZr1	23.82655964	24.43445925	0.859699878
ATiZr2	25.04235886		
ATi25VZr1	24.15515361	23.99085662	0.232351024
ATi25VZr2	23.82655964		
ATi50VZr1	21.69348566	21.02704888	0.942483923
ATi50VZr2	20.36061211		
ATi75VZr1	3.22310499	4.101036561	1.241582735
ATi75VZr2	4.978968133		
CPTi25V1	2.202467898	2.258072084	0.066448368
CPTi25V2	2.331661909		
CPTi25V3	2.240086446		
CPTi50V1	1.298138588	1.312167934	0.078063678
CPTi50V2	1.396294998		
CPTi50V3	1.242070216		
CPTi75V1	1.49810774	1.517898624	0.045972906
CPTi75V2	1.485135553		
CPTi75V3	1.570452579		
Ti25V1	24.83516552	25.1385655	1.444497142
Ti25V2	26.71066449		
Ti25V3	23.86986648		
Ti50V1	21.48996061	20.4417595	1.259289718
Ti50V2	19.04486664		
Ti50V3	20.79045126		

Sample Name	**Interface Energy (J/m2)**	**Interface Energy Average**	**STD Dev**
Ti75V1	15.18457695	14.46359732	1.632035553
Ti75V2	15.61098061		
Ti75V3	12.59523439		
CPTiZr1	1.246921958	1.019413368	0.260408446
CPTiZr2	0.735387407		
CPTiZr3	1.075930737		
CPTi25VZr1	1.097028338	0.695946529	0.347411465
CPTi25VZr2	0.488715163		
CPTi25VZr3	0.502096085		
CPTi50VZr1	0.842057522	0.456781734	0.333691315
CPTi50VZr2	0.259472741		
CPTi50VZr3	0.268814938		
CPTi75VZr1	0.211396361	0.306077709	0.082030378
CPTi75VZr2	0.355777374		
CPTi75VZr3	0.351059391		
TiZr1	19.85925359	16.71682179	2.721773925
TiZr2	15.18913835		
TiZr3	15.10207343		
Ti25VZr1	18.29679718	17.37234122	3.346410735
Ti25VZr2	20.15934402		
Ti25VZr3	13.66088245		
Ti50VZr1	4.031024163	5.574622669	1.4615615
Ti50VZr2	5.755541428		
Ti50VZr3	6.937302415		
Ti75VZr1	0.505164012	0.439174249	0.143166774
Ti75VZr2	0.537445275		
Ti75VZr3	0.274913459		
CPTiHAp1			
CPTiHAp2	0.785323584	0.450393688	0.473662401
CPTiHAp3	0.115463792		
CPTi25VHAp1	0.094359751	0.180953933	0.084012825
CPTi25VHAp2	0.262122391		
CPTi25VHAp3	0.186379659		

Sample Name	**Interface Energy (J/m2)**	**Interface Energy Average**	**STD Dev**
CPTi50VHAp1	0.430088628	0.339315558	0.098022468
CPTi50VHAp2	0.235374847		
CPTi50VHAp3	0.352483198		
CPTi75VHAp1	0.147904539	0.096269962	0.05665927
CPTi75VHAp2	0.105247441		
CPTi75VHAp3	0.035657907		
TiHAp1	2.269292142	2.431186576	0.843571189
TiHAp2	1.68029547		
TiHAp3	3.343972115		
Ti25VHAp1	3.516952039	3.205388145	1.442843296
Ti25VHAp2	4.466995606		
Ti25VHAp3	1.632216791		
Ti50VHAp1	3.931360522	3.396656244	0.510405578
Ti50VHAp2	2.914636094		
Ti50VHAp3	3.343972115		
Ti75VHAp1	0.894930976	0.781840627	0.166490561
Ti75VHAp2	0.590658769		
Ti75VHAp3	0.859932136		

Sample Name	Evans Interface Toughness (MPa.m$^{1/2}$)	Evans Interface Toughness Average	STD Dev
ACPTiZr1	0.696090969	0.753218821	0.080790982
ACPTiZr2	0.810346672		
ACPTi25VZr1	2.116244362	2.097224094	0.026898721
ACPTi25VZr2	2.0782		
ACPTi50VZr1	1.851946875	1.839633601	0.017413599
ACPTi50VZr2	1.827320327		
ACPTi75VZr1	0.596506677	0.562685757	0.047830004
ACPTi75VZr2	0.528864837		
ATiZr1	1.845214181	1.868460287	0.032874959
ATiZr2	1.891706394		
ATi25VZr1	1.857894359	1.85155427	0.00896624
ATi25VZr2	1.845214181		
ATi50VZr1	1.760681431	1.733208154	0.038853081
ATi50VZr2	1.705734877		
ATi75VZr1	0.6786617	0.761081531	0.116559242
ATi75VZr2	0.843501361		
CPTi25V1	0.545282648	0.552083299	0.008102096
CPTi25V2	0.561047554		
CPTi25V3	0.549919694		
CPTi50V1	0.418627172	0.420759895	0.012476874
CPTi50V2	0.434165665		
CPTi50V3	0.409486849		
CPTi75V1	0.449716071	0.452642494	0.006828636
CPTi75V2	0.447764782		
CPTi75V3	0.460446629		
Ti25V1	1.831050885	1.841698482	0.052721575
Ti25V2	1.898931201		
Ti25V3	1.79511336		
Ti50V1	1.703274694	1.660683469	0.051496842
Ti50V2	1.603451588		
Ti50V3	1.675324124		

Sample Name	**Evans Interface Toughness (MPa.m$^{1/2}$)**	**Evans Interface Toughness Average**	**STD Dev**
Ti75V1	1.431753432	1.395815906	0.080158542
Ti75V2	1.451717046		
Ti75V3	1.30397724		
CPTiZr1	0.422119826	0.37946706	0.050183467
CPTiZr2	0.324171036		
CPTiZr3	0.392110319		
CPTi25VZr1	0.395936042	0.309354911	0.075002982
CPTi25VZr2	0.264267661		
CPTi25VZr3	0.267861028		
CPTi50VZr1	0.346886177	0.245146126	0.088126214
CPTi50VZr2	0.192558185		
CPTi50VZr3	0.195994017		
CPTi75VZr1	0.173806041	0.207754385	0.029409693
CPTi75VZr2	0.225478573		
CPTi75VZr3	0.223978541		
TiZr1	1.684603021	1.542305604	0.123251313
TiZr2	1.473271146		
TiZr3	1.469042645		
Ti25VZr1	1.616976289	1.570483187	0.155355004
Ti25VZr2	1.6972832		
Ti25VZr3	1.397190074		
Ti50VZr1	0.758968611	0.887176349	0.119572396
Ti50VZr2	0.906899592		
Ti50VZr3	0.995660843		
Ti75VZr1	0.26867813	0.248004238	0.043334137
Ti75VZr2	0.277129807		
Ti75VZr3	0.198204776		
CPTiHAp1			
CPTiHAp2	0.139921824	0.096786797	0.061002141
CPTiHAp3	0.053651769		
CPTi25VHAp1	0.048501429	0.065834608	0.016293521
CPTi25VHAp2	0.080837561		
CPTi25VHAp3	0.068164836		

Sample Name	Evans Interface Toughness (MPa.m$^{1/2}$)	Evans Interface Toughness Average	STD Dev
CPTi50VHAp1	0.103547619	0.09129699	0.013637983
CPTi50VHAp2	0.076602186		
CPTi50VHAp3	0.093741166		
CPTi75VHAp1	0.060722814	0.047253777	0.015831491
CPTi75VHAp2	0.051223224		
CPTi75VHAp3	0.029815292		
TiHAp1	0.237851746	0.243750669	0.042339564
TiHAp2	0.204669895		
TiHAp3	0.288730367		
Ti25VHAp1	0.29610406	0.277178109	0.067999514
Ti25VHAp2	0.333709755		
Ti25VHAp3	0.201720511		
Ti50VHAp1	0.3130636	0.29045088	0.021803436
Ti50VHAp2	0.269558672		
Ti50VHAp3	0.288730367		
Ti75VHAp1	0.14936743	0.139044043	0.015396794
Ti75VHAp2	0.121347118		
Ti75VHAp3	0.146417581		

Sample Name	**Film Toughness ($MPa.m^{1/2}$)**	**Film Toughness Average**	**STD Dev**
ACPTiZr1	0.327207132	0.337346503	0.014339236
ACPTiZr2	0.347485874		
ACPTi25VZr1	0.37100443	0.3708	0.000313036
ACPTi25VZr2	0.3706		
ACPTi50VZr1	0.36525447	0.365622746	0.000520821
ACPTi50VZr2	0.365991022		
ACPTi75VZr1	0.331426162	0.344883004	0.019030847
ACPTi75VZr2	0.358339845		
ATiZr1	0.659404869	0.659970404	0.000799787
ATiZr2	0.66053594		
ATi25VZr1	0.665288817	0.665288817	0
ATi25VZr2	0.665288817		
ATi50VZr1	0.662119804	0.661667245	0.000640015
ATi50VZr2	0.661214686		
ATi75VZr1	0.642239489	0.642352255	0.000159476
ATi75VZr2	0.642465022		
CPTi25V1	0.393523218	0.393960908	0.001719133
CPTi25V2	0.39250293		
CPTi25V3	0.395856578		
CPTi50V1	0.389194997	0.388419849	0.001734208
CPTi50V2	0.389631287		
CPTi50V3	0.386433264		
CPTi75V1	0.373292567	0.375902606	0.002943825
CPTi75V2	0.375321658		
CPTi75V3	0.379093594		
Ti25V1	0.665058293	0.665812893	0.000942526
Ti25V2	0.666869375		
Ti25V3	0.665511011		
Ti50V1	0.657367423	0.657141376	0.000226045
Ti50V2	0.657141373		
Ti50V3	0.656915333		

Sample Name	**Film Toughness ($MPa.m^{1/2}$)**	**Film Toughness Average**	**STD Dev**
Ti75V1	0.655559273	0.655559299	0.000677951
Ti75V2	0.656237264		
Ti75V3	0.654881361		
CPTiZr1	0.395578416	0.393870558	0.005544033
CPTiZr2	0.387673529		
CPTiZr3	0.398359728		
CPTi25VZr1	0.385236834	0.367265257	0.016635746
CPTi25VZr2	0.352404534		
CPTi25VZr3	0.364154404		
CPTi50VZr1	0.345622557	0.360300784	0.013553099
CPTi50VZr2	0.372340825		
CPTi50VZr3	0.36293897		
CPTi75VZr1	0.362846406	0.359681175	0.013523613
CPTi75VZr2	0.344855671		
CPTi75VZr3	0.371341447		
TiZr1	0.655786911	0.656465187	0.001174808
TiZr2	0.657821738		
TiZr3	0.655786911		
Ti25VZr1	0.657143384	0.656163737	0.001019383
Ti25VZr2	0.656239034		
Ti25VZr3	0.655108793		
Ti50VZr1	0.643141671	0.642916121	0.000390664
Ti50VZr2	0.642465022		
Ti50VZr3	0.643141671		
Ti75VZr2	0.476887056		
Ti75VZr3	0.437405574		
CPTiHAp1			
CPTiHAp2	0.280123308	0.264777264	0.021702583
CPTiHAp3	0.249431221		
CPTi25VHAp1	0.291513507	0.280729667	0.009479416
CPTi25VHAp2	0.273712651		
CPTi25VHAp3	0.276962844		

Sample Name	Film Toughness (MPa.m$^{1/2}$)	Film Toughness Average	STD Dev
CPTi50VHAp1	0.300311949	0.298430638	0.006147019
CPTi50VHAp2	0.291562813		
CPTi50VHAp3	0.303417153		
CPTi75VHAp1	0.287334318	0.252179732	0.06547899
CPTi75VHAp2	0.292573246		
CPTi75VHAp3	0.176631633		
TiHAp1	0.52137789	0.521753798	0.001354872
TiHAp2	0.520626572		
TiHAp3	0.523256931		
Ti25VHAp1	0.523068979	0.52231792	0.002527599
Ti25VHAp2	0.524384867		
Ti25VHAp3	0.519499915		
Ti50VHAp1	0.528900443	0.523885411	0.004347205
Ti50VHAp2	0.521190044		
Ti50VHAp3	0.521565746		
Ti75VHAp1	0.444526801	0.410918181	0.047550557
Ti75VHAp2	0.431715745		
Ti75VHAp3	0.356511997		

Sample Name	Shear stress (MPa) Debonded	Shear stress Average	STD Dev
ACPTiZr1	6.564109575	6.753957938	0.268486129
ACPTiZr2	6.943806301		
ACPTi25VZr1	7.38086728	7.376769833	0.005794665
ACPTi25VZr2	7.372672386		
ACPTi50VZr1	7.274333666	7.281162744	0.009657774
ACPTi50VZr2	7.287991822		
ACPTi75VZr1	6.643326878	6.894636941	0.355406099
ACPTi75VZr2	7.145947003		
ATiZr1	13.7199572	13.7309932	0.015607263
ATiZr2	13.7420292		
ATi25VZr1	13.83473161	13.83973161	0.007071068
ATi25VZr2	13.84473161		
ATi50VZr1	13.77293	13.7641012	0.012485811
ATi50VZr2	13.7552724		
ATi75VZr1	13.38446275	13.38666995	0.003121453
ATi75VZr2	13.38887715		
CPTi25V1	7.94358329	7.951778183	0.032205456
CPTi25V2	7.924461872		
CPTi25V3	7.987289388		
CPTi50V1	7.867097619	7.852528919	0.032589325
CPTi50V2	7.875292512		
CPTi50V3	7.815196627		
CPTi75V1	7.561154933	7.610324293	0.055446056
CPTi75V2	7.599397769		
CPTi75V3	7.670420178		
Ti25V1	13.83473161	13.84944628	0.018378615
Ti25V2	13.87004682		
Ti25V3	13.84356041		
Ti50V1	13.68464199	13.68022759	0.004414401
Ti50V2	13.68022759		
Ti50V3	13.67581319		

Sample Name	Shear stress (MPa) Debonded	Shear stress Average	STD Dev
Ti75V1	13.64932679	13.64932679	0.013243202
Ti75V2	13.66256999		
Ti75V3	13.63608358		
CPTiZr1	7.872560881	7.876203056	0.098389293
CPTiZr2	7.779685423		
CPTiZr3	7.976362863		
CPTi25VZr1	7.735979325	7.357193143	0.347522458
CPTi25VZr2	7.053071545		
CPTi25VZr3	7.282528559		
CPTi50VZr1	6.938343039	7.234269743	0.281349165
CPTi50VZr2	7.498327418		
CPTi50VZr3	7.266138773		
CPTi75VZr1	7.312576502	7.240643549	0.286838611
CPTi75VZr2	6.924684883		
CPTi75VZr3	7.484669262		
TiZr1	13.64932679	13.66256999	0.022937899
TiZr2	13.68905639		
TiZr3	13.64932679		
Ti25VZr1	13.67581319	13.65668412	0.019905635
Ti25VZr2	13.65815559		
Ti25VZr3	13.63608358		
Ti50VZr1	13.40212035	13.39770595	0.007645966
Ti50VZr2	13.38887715		
Ti50VZr3	13.40212035		
Ti75VZr1	11.13311842	10.17813641	0.918474728
Ti75VZr2	10.10014867		
Ti75VZr3	9.301142154		
CPTiHAp1			
CPTiHAp2	7.107704168	6.733470705	0.529246039
CPTiHAp3	6.359237242		
CPTi25VHAp1	7.416378484	7.099509274	0.276704929
CPTi25VHAp2	6.905563465		
CPTi25VHAp3	6.976585874		

Sample Name	Shear stress (MPa) Debonded	Shear stress Average	STD Dev
CPTi50VHAp1	7.621250818	7.573902545	0.147844934
CPTi50VHAp2	7.408183591		
CPTi50VHAp3	7.692273227		
CPTi75VHAp1	7.323503026	6.482160642	1.56974698
CPTi75VHAp2	7.451889689		
CPTi75VHAp3	4.671089211		
TiHAp1	13.48157956	13.49040836	0.031832696
TiHAp2	13.46392196		
TiHAp3	13.52572357		
Ti25VHAp1	13.52130917	13.50365157	0.059389687
Ti25VHAp2	13.55220997		
Ti25VHAp3	13.43743556		
Ti50VHAp1	13.65815559	13.54043824	0.102041746
Ti50VHAp2	13.47716516		
Ti50VHAp3	13.48599396		
Ti75VHAp1	11.6540177	10.83441064	1.162307023
Ti75VHAp2	11.34500965		
Ti75VHAp3	9.504204583		

Sample Name	**Film Fracture Energy** G **(J/m2)**	**Film Fracture Energy Average**	**STD Dev**
ACPTiZr1	0.749226784	0.797099161	0.067701766
ACPTiZr2	0.844971539		
ACPTi25VZr1	0.963221043	0.9621	0.001624472
ACPTi25VZr2	0.9609		
ACPTi50VZr1	0.933595716	0.935480252	0.002665135
ACPTi50VZr2	0.937364787		
ACPTi75VZr1	0.768672507	0.833627521	0.091860263
ACPTi75VZr2	0.898582536		
ATiZr1	3.042790635	3.048014378	0.007387488
ATiZr2	3.053238121		
ATi25VZr1	3.097335267	3.097335267	0
ATi25VZr2	3.097335267		
ATi50VZr1	3.067898078	3.063707127	0.0059269
ATi50VZr2	3.059516176		
ATi75VZr1	2.886434999	2.887448794	0.001433722
ATi75VZr2	2.888462588		
CPTi25V1	1.147114986	1.149682724	0.010041472
CPTi25V2	1.141174442		
CPTi25V3	1.160758742		
CPTi50V1	1.122020338	1.117570253	0.009967321
CPTi50V2	1.12453733		
CPTi50V3	1.106153092		
CPTi75V1	1.032202522	1.046729976	0.016412241
CPTi75V2	1.04345442		
CPTi75V3	1.064532985		
Ti25V1	3.276315055	3.283758522	0.009299811
Ti25V2	3.294183433		
Ti25V3	3.280777078		
Ti50V1	3.200977247	3.198776462	0.002200644
Ti50V2	3.198776182		
Ti50V3	3.196575959		

Sample Name	Film Fracture Energy G (J/m2)	Film Fracture Energy Average	STD Dev
Ti75V1	3.1833923	3.183394824	0.006584256
Ti75V2	3.189980342		
Ti75V3	3.17681183		
CPTiZr1	1.095047469	1.085755823	0.030471833
CPTiZr2	1.051719839		
CPTiZr3	1.110500162		
CPTi25VZr1	1.038540364	0.945194317	0.086040485
CPTi25VZr2	0.869061972		
CPTi25VZr3	0.927980615		
CPTi50VZr1	0.835933881	0.909300996	0.067986177
CPTi50VZr2	0.970172776		
CPTi50VZr3	0.92179633		
CPTi75VZr1	0.921326204	0.906175458	0.067656218
CPTi75VZr2	0.832228367		
CPTi75VZr3	0.964971803		
TiZr1	3.009492463	3.015727512	0.010799422
TiZr2	3.02819761		
TiZr3	3.009492463		
Ti25VZr1	3.021955399	3.012956908	0.009360743
Ti25VZr2	3.013643593		
Ti25VZr3	3.003271733		
Ti50VZr1	2.8945501	2.89252093	0.003514627
Ti50VZr2	2.888462588		
Ti50VZr3	2.8945501		
Ti75VZr1	1.953594242	1.627976482	0.308986805
Ti75VZr2	1.59147141		
Ti75VZr3	1.338863795		
CPTiHAp1			
CPTiHAp2	3.147575911	2.821600507	0.460998838
CPTiHAp3	2.495625102		
CPTi25VHAp1	3.40874948	3.16362023	0.215301703
CPTi25VHAp2	3.005159068		
CPTi25VHAp3	3.076952142		

Sample Name	**Film Fracture Energy** G (J/m2)	**Film Fracture Energy Average**	**STD Dev**
CPTi50VHAp1	3.617619994	3.573447108	0.146539382
CPTi50VHAp2	3.409902693		
CPTi50VHAp3	3.692818636		
CPTi75VHAp1	3.311713219	2.665581608	1.226185819
CPTi75VHAp2	3.433578183		
CPTi75VHAp3	1.251453421		
TiHAp1	10.90392716	10.91970514	0.056739841
TiHAp2	10.87252416		
TiHAp3	10.98266409		
Ti25VHAp1	10.97477564	10.99583449	0.105809294
Ti25VHAp2	11.03006372		
Ti25VHAp3	10.8255179		
Ti50VHAp1	11.2208455	11.0095677	0.18314057
Ti50VHAp2	10.8960715		
Ti50VHAp3	10.9117861		
Ti75VHAp1	7.92635687	6.833578896	1.519560572
Ti75VHAp2	7.476072393		
Ti75VHAp3	5.098307427		